

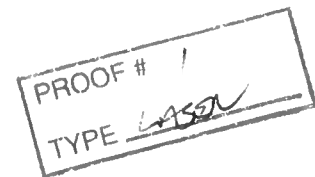
CWP-560
December 2006



Anisotropic Geometrical-Spreading Correction and Its Application in Azimuthal AVO Analysis

Xiaoxia (Ellen) Xu

— Doctoral Thesis —
Geophysics



Defended on November 10, 2006

Advisor:	Prof. Ilya Tsvankin
Committee members:	Prof. Ken Larner
	Prof. Max Peeters
	Prof. William Navidi
	Prof. Eileen Poeter

Center for Wave Phenomena
Colorado School of Mines
Golden, Colorado 80401
(1) 303 273-3557

Abstract

Velocity variations with angle in anisotropic media influence not only reflection coefficients but also geometrical spreading. Anisotropy-induced distortions in geometrical spreading can be comparable to those in reflection coefficients. Since AVO (amplitude-variation-with-offset) analysis operates with reflection coefficients, an important element of AVO processing, particularly for azimuthal AVO, is to correct amplitude responses for anisotropic geometrical spreading.

Using paraxial ray theory, I obtain a concise expression for geometrical spreading as a function of reflection traveltimes recorded over laterally homogeneous, arbitrarily anisotropic media. By extending the Alkhalifah-Tsvankin (1995) nonhyperbolic moveout equation to orthorhombic media, I further express azimuthally-varying geometrical spreading in terms of normal-moveout velocities and anellipticity parameters. Weak-anisotropy approximation reveals that the azimuthal variation of geometrical spreading is primarily controlled by the difference between the anellipticity parameters in the two vertical symmetry planes of orthorhombic media.

Using the analytic results, I develop a moveout-based anisotropic spreading correction (MASC) that computes geometrical spreading from estimated normal-moveout velocities and anellipticity parameters. The implementation of MASC involves almost no extra cost; the spreading correction can be incorporated easily into the processing sequence that estimates azimuthal moveout and AVO attributes. MASC proves to be insensitive to the trade-offs between moveout velocities and anellipticity parameters as long as they approximate the traveltime surface with adequate accuracy. Sensitivity studies show that the robustness of MASC is lower than that of normal-moveout inversion, but higher than that of estimation for anellipticity parameters.

The underlying assumption of the MASC methodology is that the medium is laterally homogeneous. I perform numerical modeling to show that MASC remains sufficiently accurate for media with mild reflector dip and moderate lateral velocity variation. Because of the high sensitivity of shear waves to the presence of anisotropy, it is imperative to correct for geometrical spreading in AVO analysis of converted PS-waves. I, therefore, extend the MASC algorithm to PS-waves. The formalism developed for P-waves can be used to correct for the geometrical spreading for PS-waves, albeit with slightly lower accuracy.

To evaluate the accuracy of MASC and its significance for azimuthal AVO analysis, I apply anisotropic spreading correction to wide-azimuth full-wavefield synthetic data and field data. Synthetic studies on models with strong azimuthal anisotropy verify the accuracy of MASC. In addition, I show that application of MASC is critically important for accurate quantitative AVO inversion. For qualitative AVO analysis, application of MASC becomes essential when the magnitude of the azimuthal variation of geometrical spreading reaches about one-third of that of the corresponding reflection coefficient. Also, I demonstrate

that the influence of transmission loss on azimuthal AVO analysis of P-waves is negligible. Application of MASC to wide-azimuth data from the Rulison field, Colorado, confirms that MASC is essential for reliable estimation of azimuthal AVO attributes. In addition, the field study proves the stability of azimuthal AVO attributes and helps to improve understanding of the fracture distribution in the reservoir.

Table of Contents

Abstract	i
Acknowledgments	vii
Chapter 1 Introduction	1
Chapter 2 Geometrical spreading of P-waves	7
2.1 Summary	7
2.2 Introduction	7
2.3 Relative geometrical spreading as a function of reflection traveltime	9
2.3.1 Nonhyperbolic moveout equation for an orthorhombic layer	11
2.3.2 Geometrical spreading as a function of moveout coefficients	14
2.3.3 Analysis of the weak-anisotropy approximation	15
2.3.4 Numerical example	17
2.4 Comparison with dynamic ray tracing	21
2.5 Discussion and conclusions	21
2.6 References	26
Chapter 3 Correction for wide-azimuth P-wave reflections	29
3.1 Summary	29
3.2 Introduction	29
3.3 Moveout equations for orthorhombic media	31
3.3.1 Layered models with uniform symmetry-plane orientation	34
3.3.2 Models with misaligned symmetry planes	35
3.4 Azimuth-dependent geometrical-spreading correction	38
3.4.1 Synthetic example	39
3.4.2 Error analysis	42
3.4.3 Field-data application	46
3.5 Discussion and conclusions	46
3.6 References	48
Chapter 4 Full-waveform synthetic data estimation	51
4.1 Introduction	51
4.2 Synthetic modeling	52
4.3 Estimation of the reflection coefficient from the AVO response	53

4.3.1	Model 1	55
4.3.2	Model 2	58
4.3.3	Model 3	60
4.4	Influence of the transmission loss	62
4.5	Discussion	64
Chapter 5 Case studies of azimuthal AVO analysis		67
5.1	Introduction	67
5.2	Geologic background	68
5.3	Data acquisition and processing	68
5.4	Results of azimuthal seismic analysis	74
5.4.1	Mesaverde top	74
5.4.2	Top of the reservoir (UMV Shale)	76
5.4.3	Bottom of the reservoir (Cameo Coal)	76
5.5	Comparison with the fault system and EMI log	80
5.5.1	Fault system	80
5.5.2	EMI and production logs	80
5.6	Discussion	83
5.6.1	Acquisition footprint	83
5.6.2	Error analysis	84
5.6.3	Correlation between the NMO and AVO ellipses	84
5.6.4	Group angle versus phase angle	84
5.7	Conclusions	85
5.8	References	85
Chapter 6 Correction in the presence of lateral heterogeneity		89
6.1	Introduction	89
6.2	Numerical tests	89
6.2.1	Layered isotropic model	89
6.2.2	Dipping orthorhombic layer	90
6.2.3	Isotropic layer with quadratic lateral velocity variation	91
6.3	Conclusions	91
6.4	References	93
Chapter 7 MASC for Converted PS-Waves		95
7.1	Introduction	95
7.2	Moveout-based expression for geometrical spreading of PS-waves	96
7.3	Algorithm for moveout-based anisotropic spreading correction	98
7.4	Application to AVO analysis of synthetic data	101
7.5	Conclusions	105
7.6	References	105

Chapter 8	Conclusions	107
Appendix A	Relative geometrical spreading as a function of reflection traveltime	111
Appendix B	Traveltime derivatives from the nonhyperbolic moveout equation	115
Appendix C	Traveltime derivatives for the geometrical-spreading correction	117

Acknowledgments

I am deeply grateful to many people without whom the completion of this thesis would not have been possible. My advisor, Ilya Tsvankin, provided me with solid guidance throughout my Ph.D. study. I admire his sharp scientific insights and clear and elegant writing style. As my advisor, he is always available to discuss my research and extremely efficient in revising my manuscripts. His firm support was indispensable for my success at CSM. My other committee members, Ken Lerner, Max Peeters, Eileen Poeter, and Williams Navidi each supported me in a unique way. Ken taught me how to produce “Ken Lerner” clear presentations, whether oral or written. Max constantly reminded me of the broader context of my research. My minor representative Dr. Poeter helped me with geological aspects of my Ph.D. study and Dr. Navidi saw to it that I understand uncertainty.

My gratitude also goes to the alumni, faculty and staff at the CSM Geophysics Department. Zhaobo Meng first introduced me to CWP. Mike Batzle took me on for a fun ride with my second comprehensive project. Dave Hale enlightened me on computational aspect of geophysics. I will never forget the warm encouragement from Roel Snieder and Terry Young. Paul Sava, though newly arrived, has taught me how to document reproducible research. Tom Davis and his consortium (RCP) provided me with resources necessary for the field application of my research. Seismic Unix guru John Stockwell brought me up to speed in programming in SU and taught me how to interact with colleagues in a men-dominated field.

I am also indebted to Barbara McLenon, Michelle Szobody, the late Lela Webber, Sara Summers, Barbara Middlebrook, and Susan Venable for making CWP and the Department in general a warm place to work in. Michelle is always on top of everything, which took so much logistical burden off my shoulders. Barbara, especially, provides me with professional help and warm friendship. I will never forget the lunch Barbara and Lela invited me to when I just arrived in Golden and the idioms they taught me such as “it is raining cats and dogs.”

Without many friends at the Department, study at a demanding graduate school would be too difficult to bear. Debashish Sarkar and his wife, Roshni, always had their home open for me and entertained me with delicious Indian cuisine and culture. At the beginning of my Ph.D. journey, when I was still in doubt about my capabilities, Andres Pech’s encouragement was so precious. Yaping Zhu and his wife, Hanqiu, helped us purchase our first car and get familiar with the Denver area. Lunch with Jyoti Behura was a special time everyday. His good sense of humor eased much strain from work. The favorite adage of Rodrigo Fuck, “don’t worry, be happy”, helped me much during tough times. I will also cherish the many fond memories with and appreciate help from CWP fellow students Ivan Vasconcelos, Carlos Pacheco, Kurang Mehta, Matt Reynolds, Steve Smith, Dongjie Cheng, Alison Malcom, Jia Yan, Jianmin Lin, Jun Li, Xiaoxiang Wang, and Yuanzhong Fan. The collaboration with

RCP and the Center for Rock Abuse provided me an opportunity to develop friendship with Ronny Hoffmann and Mila Adams. I am also grateful to RCP students and alumni, Eldar Guliyev, Gerardo Franco, Michael Rumon, Matthew Casey, K.J. Jansen, Lauri Burke, and Shannon Higgins for providing resources for my field study.

It is said that one does not know how to work without knowing how to relax. Playing sports is an essential element of my daily life. I thank Yris for the companionship to hike almost all the trails at the foothills. The volleyball matches with the Chinese mafia on campus is forever imprinted in my memory. My unfailing stamina is gained through playing badminton with Bin, Jiaqiu, Huang and his wife.

The caring and love kindly shown to me by Nadine and Catherine is beyond words to thank for. I am looking forward to watch “The Lion, the Witch and the Wardrobe” with them to celebrate my defense. The love and guidance by sisters, Duan Ling and Wenzhi, made me a better person.

Finally, I thank my parents for their forever love and patience. My Mom is always ready to laugh with my laughter and cry with my crying. My aunts, Huanfan and Jin, are always proud of my least achievements. Last but no way the least, I am grateful to my husband, Qiufeng (David) Wang, whom this thesis is dedicated to. He is willing to give up anything for our marriage and showed me what true love is.

Chapter 1

Introduction

Geometrical spreading is one of the most fundamental subjects in wave propagation. With the expansion of wavefronts away from a source, the amplitudes of elastic waves decay as a function of traveltimes and medium properties. Although geometrical spreading is a dynamic quantity describing amplitude decay, it is governed by kinematic properties of wavefronts. While geometrical spreading in isotropic homogeneous media is simple (i.e., it depends solely on the source-receiver distance), it is complicated in anisotropic and heterogeneous media. For instance, explicit expression for geometrical spreading in homogeneous transversely isotropic media with vertical symmetry axis (VTI media) involves evaluation of residues of a complicated integrand associated with the Christoffel matrix (Tsvankin, 2005). Anisotropy acts like a lens that focuses and defocuses energy along a wavefront. As illustrated in Figures 1.1 and 1.2, the distribution of rays strongly varies with angle when rays are traced in a homogeneous, moderately anisotropic VTI medium using a constant phase-angle increment. These distortions of geometrical spreading become even more complicated in azimuthally anisotropic media.

The most straightforward way to compute geometrical spreading is by dynamic ray tracing. Since geometrical spreading is proportional to the cross-section area of a ray tube, it can be computed by tracing a bundle of rays. For simple homogeneous models, it is also possible to express geometrical spreading analytically. Modeling methods, however, require accurate knowledge of the anisotropic, heterogeneous velocity field, which is seldom available in practice.

An alternative approach, most suitable for processing, is based on relating geometrical spreading to reflection traveltimes recorded on the earth's surface. One of the most practical and important results of paraxial ray theory is an expression for geometrical spreading in terms of the traveltimes functions at the source and receiver locations (Červený, 2001). Direct implementation of this equation involves cumbersome sorting of data and suffers from instability (Tygel et al., 1992). Ursin and Hokstad (2003) simplify this equation for stratified VTI media. By employing the Tsvankin-Thomsen (1994) nonhyperbolic moveout equation, those authors further express geometrical spreading as a function of moveout parameters. Since orthorhombic model is typical for realistic fractured reservoirs, in Chapter 2 I obtain a concise equation for geometrical spreading as a function of traveltimes recorded over stratified azimuthally anisotropic media.

One important application of the obtained equation is to correct azimuthal AVO responses for anisotropic geometrical spreading. Azimuthal AVO analysis represents one of the most effective seismic tools for characterizing fractured reservoirs. The presence of

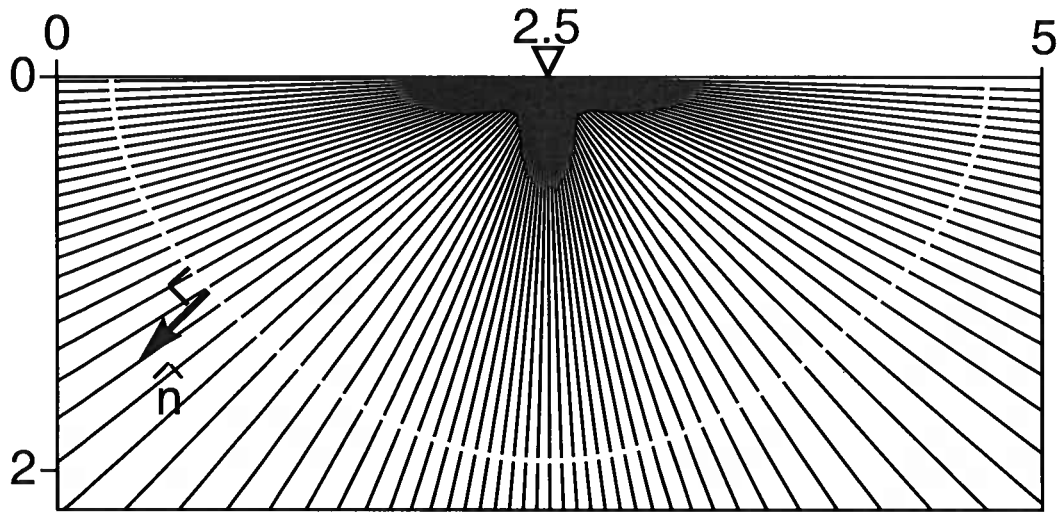


Figure 1.1. P-wave propagation from a point source (triangle) in a vertical plane of a homogeneous VTI medium with $\epsilon = 0.15$ and $\delta = -0.1$. The rays (in black) are computed with a constant increment in phase angle; the wavefront is shown in white. Notice that the density of rays strongly varies with angle (after Tsvankin, 2005).

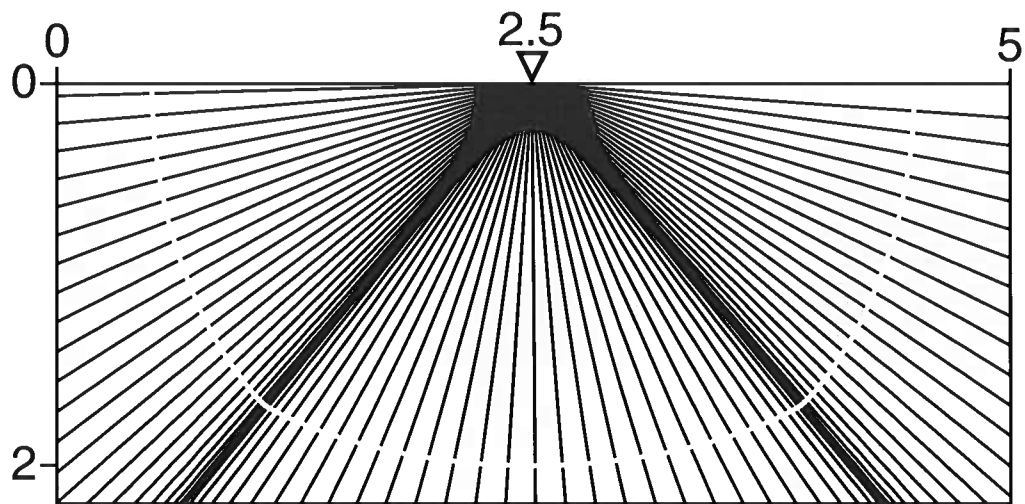


Figure 1.2. SV-wave propagation from a point source (triangle) in a vertical plane of a homogeneous VTI medium with $\epsilon = 0.15$ and $\delta = -0.1$ ($\sigma = 0.42$). The rays (in black) are computed with a constant increment in phase angle; the wavefront is shown in white. Notice the concentration of rays near the velocity maximum at an angle of 45° (after Tsvankin, 2005).

preferentially oriented fractures or horizontal stresses yields an azimuthally-varying AVO response that can be used to infer fracture orientation and intensity. Compared to traveltimes inversion, the advantages of amplitude methods are their strong sensitivity to the presence of anisotropy and high vertical resolution that makes AVO analysis applicable to thin reservoirs. Based on the theoretical work of Rüger and Tsvankin (1997), azimuthal AVO analysis is becoming a routine tool for fracture characterization. Current processing for azimuthal AVO attributes, however, involves a simplified assumption that AVO responses recorded on the earth's surface represent reflection coefficients at the target horizon. In fact, the amplitude signature observed on the earth's surface is controlled by the radiation pattern of the source, geometrical spreading, attenuation, the reflection/transmission coefficients along the raypath, and the conversion coefficients at the receiver. Since AVO analysis aims at estimating the reflection coefficient at the target horizon, an essential element of AVO processing is removal of all the other factors from the measured amplitudes. If the medium is not strongly attenuative, geometrical spreading typically makes the most significant contribution to the measured amplitude, in particular when azimuthal anisotropy is present in the overburden. An exact geometrical-spreading correction allows accurate reconstruction of the reflection coefficients, which not only ensures reliable qualitative AVO analysis, but also makes possible quantitative AVO inversion for medium parameters (Jilek, 2002). Furthermore, fracture density and fluid infill can be estimated from these parameters using effective medium theory (Bakulin et al, 2001).

The goal of this thesis is to develop a practical methodology to correct for geometrical spreading for both PP- and PS-waves in horizontally-layered azimuthally anisotropic media. I carry out azimuthal AVO analysis of synthetic and field data to evaluate the performance of the correction algorithm.

Chapter 2 is devoted to the theoretical aspects. I derive a concise equation for geometrical spreading as a function of traveltimes measured on the earth's surface. The geometrical spreading is further related to moveout parameters that describe long-offset, wide-azimuth traveltimes. By applying the weak-anisotropy approximation, I also identify the key parameters controlling variations of geometrical spreading with offset and azimuth. Finally, I perform numerical tests to verify the analytic results.

In Chapter 3, I develop a practical algorithm for anisotropic geometrical-spreading correction (MASC). The algorithm is designed in such a way that it readily fits into the processing sequence for azimuthal moveout and AVO attributes. In addition, I test the robustness of the algorithm by introducing realistic noise and then apply the algorithm to the Weyburn field data to evaluate the azimuthal variation of geometrical spreading.

Using the full-wavefield synthetic study in Chapter 4, I answer a few questions of practical importance regarding MASC:

- 1) Can MASC, despite its reliance on ray theory, accurately reconstruct reflection coefficients in the presence of strong azimuthal anisotropy?
- 2) Can we replace MASC with simple gain corrections commonly used in practice?
- 3) Is it possible to ignore the contribution of transmission loss along the raypath, which is not accounted for by MASC?

The underlying assumption of Chapters 2 to 4 is that the medium is laterally homo-

geneous. Since the subsurface structure often violates this assumption, it is important to test the applicability of MASC to models with mild lateral heterogeneity. By performing a series of numerical tests in Chapter 5, I show that the error of MASC is acceptable for media with mild reflector dip and moderate lateral velocity variation.

Guided by insights from the synthetic study, in Chapter 6 I apply MASC to azimuthal AVO analysis of a wide-azimuth data acquired at the Rulison field, Colorado. A number of processing steps are used to obtain azimuthal seismic attributes including NMO ellipses, 3D nonhyperbolic moveout parameters, and azimuthal AVO gradients. I show that application of MASC is important for reliable estimation of the azimuthal AVO gradient for reflections from the bottom of the reservoir.

The high sensitivity of shear-wave amplitudes to the presence of anisotropy makes it imperative to correct PS-wave amplitudes for geometrical spreading prior to AVO inversion. Chapter 7 extends the methodology of MASC to converted PS-waves. Since an incident P-wave excites two split shear waves, which compounds AVO analysis, the emphasis of this chapter is on PSV modes in vertical symmetry planes of horizontally layered anisotropic media. In addition, I conduct full-wavefield synthetic study to compare the performance of MASC and a conventional gain correction.

Chapter 8 summarizes the results of the thesis and discusses additional challenges that lie ahead for quantitative AVO inversion. To perform azimuthal AVO analysis, I developed two SU codes SUAZAVO and SUCONV. After 3D nonhyperbolic moveout inversion, SUAZAVO computes AVO ellipses for P-waves with application of MASC. The code SUCONV reconstructs the PSV conversion coefficient with anisotropic spreading correction. Along with the codes SUAZVELAN for extraction of NMO ellipses and SUAZNHP for 3D nonhyperbolic moveout inversion, SU now contains a comprehensive toolkit to perform azimuthal moveout and AVO analysis.

This thesis is a compendium of papers with chapters bounded by overall introduction and conclusions. Chapters 2 and 3 were published in *Geophysics* in 2005 and 2006, respectively. Likewise, chapter 4 was published in *The Leading Edge*, 2006. In the near future, I will submit chapters 5 and 7 for publication.

1.0 References

- Bakulin, A., V. Grechka, and I. Tsvankin, 2000, Estimation of fracture parameters from reflection seismic data – Part II: Fractured models with orthorhombic symmetry: *Geophysics*, **65**, 1803–1817.
- Červený V., 2001, *Seismic ray theory*: Cambridge University Press.
- Jílek, P., 2002, Modeling and inversion of converted-wave reflection coefficients in anisotropic media: A tool for quantitative AVO analysis: Ph.D. thesis, Colorado School of Mines.
- Rüger, A., and Tsvankin, I., 1997, Using AVO for fracture detection: Analytic basis and practical solutions: *The Leading Edge*, **16**, 1429–1434.

Tsvankin, I., 2005, *Seismic signatures and analysis of reflection data in anisotropic media*: Elsevier Science Publ. Co., Inc. (second edition).

Tygel, M., J. Schleicher, and P. Hubral, 1992, Geometrical spreading corrections of offset reflections in a laterally inhomogeneous earth: *Geophysics*, **57**, 1054–1063.

Ursin, B., and Hokstad, K., 2003, Geometrical spreading in a layered transversely isotropic medium with vertical symmetry axis: *Geophysics*, **68**, 2082–2091.

Chapter 2

Geometrical spreading of P-waves in horizontally layered, azimuthally anisotropic media

2.1 Summary

For purposes of processing and inversion of reflection data, it is convenient to represent geometrical spreading through the reflection traveltime measured at the earth's surface. Such expressions are particularly important for azimuthally anisotropic models in which variations of geometrical spreading with both offset and azimuth can significantly distort the results of wide-azimuth AVO (amplitude variation with offset) analysis.

Here, we present an equation for the relative geometrical spreading in laterally homogeneous, arbitrarily anisotropic media as a simple function of the spatial derivatives of reflection traveltimes. By employing the Tsvankin-Thomsen nonhyperbolic moveout equation, the spreading is represented by using the moveout coefficients, which can be estimated from surface seismic data. This formulation is then applied to P-wave reflections in an orthorhombic layer to evaluate the distortions of the geometrical spreading caused by both polar and azimuthal anisotropy.

The relative geometrical spreading of P-waves in homogeneous orthorhombic media is controlled by five parameters that are also responsible for time processing. The weak-anisotropy approximation, verified by numerical tests, shows that azimuthal velocity variations make a significant contribution to the geometrical spreading, so the existing equations for VTI (transversely isotropic with a vertical symmetry axis) media cannot be accurately used even in the vertical symmetry planes. The shape of the azimuthally varying spreading factor is close to an elliptical curve for offsets smaller than the reflector depth but becomes more complicated for larger offset-to-depth ratios. The overall magnitude of the azimuthal variation of the geometrical spreading for the moderately anisotropic model used in the tests exceeds 25% for a wide range of offsets.

While the methodology developed here is helpful in modeling and analyzing the anisotropic geometrical spreading, its main practical application is in correcting the wide-azimuth AVO signature for the influence of the anisotropic overburden.

2.2 Introduction

Inversion of prestack amplitude variation with offset and azimuth (azimuthal AVO analysis) is one of the most effective tools for characterization of naturally fractured reser-

voirs. The presence of preferentially oriented fractures or horizontal stresses makes the reservoir formation azimuthally anisotropic, and wide-azimuth reflection amplitudes can be used to estimate the fracture orientation and, in some cases, map the lateral variation of the fracture density (Mallick *et al.*, 1998; Lynn *et al.*, 1999; Bakulin *et al.*, 2000; Rüger, 2001). The main advantage of amplitude methods compared to traveltimes inversion is their high vertical resolution that makes AVO analysis applicable to relatively thin reservoir layers.

The amplitude signature of reflected waves is controlled by the radiation pattern of the source, geometrical spreading, attenuation, the reflection/transmission coefficients along the raypath, and the conversion coefficients at the receiver (Martinez, 1993; Maultzsch *et al.*, 2003). Since AVO analysis operates with the reflection coefficient at the target horizon, an essential element of AVO processing is the removal of the influence of all other factors from the measured amplitude. If the medium is not strongly attenuative, geometrical spreading typically makes the most significant contribution to the amplitude distortion above the target horizon (Martinez, 1993; Ursin and Hokstad, 2003). In particular, if the overburden is anisotropic (e.g., shales in a sand-shale sequence), it acts like a 3D focusing lens that can significantly change the amplitude distribution along the wavefront of the reflected wave (Tsvankin, 1995, 2001). Therefore, estimation of the reflection coefficient for targets beneath anisotropic layers can be strongly distorted without an accurate geometrical-spreading correction.

The most straightforward way to compute anisotropic geometrical spreading is by performing dynamic ray tracing (Gajewski and Pšenčík, 1990). For simple homogeneous models it is possible to use analytic approximations of the Green's function, such as those presented by Tsvankin (1995, 2001) for P- and SV-waves in a transversely isotropic layer. Modeling methods, however, require accurate information about the anisotropic velocity field for the whole overburden, which is seldom available in practice.

An alternative approach, more suitable for purposes of AVO processing, is based on relating geometrical spreading to the traveltimes of reflection events recorded at the surface. For example, Vanelle and Gajewski (2003) presented an algorithm to determine geometrical spreading from coarsely-gridded traveltimes tables. Ursin and Hokstad (2003) expressed the geometrical spreading in stratified transversely isotropic media with a vertical symmetry axis (VTI) in terms of the reflection traveltimes and the group angle in the subsurface layer. For horizontally layered VTI models, P-wave traveltimes can be accurately described by a nonhyperbolic moveout equation parameterized by just two moveout coefficients – the effective NMO velocity V_{nmo} and the effective anellipticity parameter η (Alkhalifah and Tsvankin, 1995). The best-fit parameters V_{nmo} and η can be estimated, for example, by a 2D semblance scan (Grechka and Tsvankin, 1998), which makes it possible to compute geometrical spreading using solely surface reflection data (Ursin and Hokstad, 2003). This approach can be also used to find analytic expressions for geometrical spreading in VTI media in terms of the parameters V_{nmo} and η .

The distortions caused by geometrical spreading in reflection amplitudes are particularly pronounced for azimuthally anisotropic media (Rüger and Tsvankin, 1997; Maultzsch *et al.*, 2003). Here we use ray theory to obtain a simple traveltimes-based equation for the geometrical spreading of pure (non-converted) reflected waves recorded over horizontally

layered arbitrarily anisotropic media. By combining this result with the Tsvankin-Thomsen moveout equation for an orthorhombic layer with a horizontal symmetry plane, we express the spreading as a function of the azimuthally varying moveout coefficients. Application of the weak-anisotropy approximation helps to explain the dependence of the relative geometrical spreading on the anisotropic parameters of orthorhombic media both within and outside the vertical symmetry planes. Numerical tests verify the accuracy of the analytic results and illustrate the character of the amplitude distortions caused by the azimuthally-varying geometrical spreading.

2.3 Relative geometrical spreading as a function of reflection travelttime

Geometrical spreading describes the amplitude decay of an elastic wave caused by the expansion of its wavefront away from the source. The relative geometrical spreading $L(R, S)$ between the source S and the receiver R is an essential part of the ray-theory Green's function G_{in} (Červený, 2001, eq. 5.4.24):

$$G_{in}(R, t; S, t_0) = \frac{g_n(S)g_i(R) \exp[iT^G(R, S)]}{4\pi[\rho(S)\rho(R)V(S)V(R)]^{1/2} L(R, S)} \times R^C \delta(t - t_0 - T(R, S)), \quad (2.1)$$

where t and t_0 are the recording and excitation times (respectively), $\rho(S)$ and $V(S)$ are density and phase velocity at the source, $\rho(R)$ and $V(R)$ are the same quantities at the receiver, $g_n(S)$ and $g_i(R)$ are the polarization vectors at the source and receiver, $T^G(R, S)$ is the complete phase shift, R^C is the product of the reflection/transmission coefficients normalized with respect to the vertical energy flux at all interfaces crossed by the ray, $\delta(t)$ is the delta function, and $T(R, S)$ is the travelttime.

Throughout the paper, we treat the relative geometrical spreading $L(R, S)$ defined by equation (eq. 4.10.11) in Červený (2001). The factor $L(R, S)$ can be expressed through the spatial derivatives of the travelttime T around a raypath (Červený, 2001, eq. 4.10.50; Goldin, 1986):

$$L(R, S) = \sqrt{\frac{\cos \phi^s \cos \phi^r}{|\det M^{\text{mix}}(R, S)|}} \quad , \quad (2.2)$$

where ϕ^s is the angle between the ray and the normal to the surface at the source, ϕ^r is the ray angle at the receiver, and the matrix M^{mix} is given by (Červený, 2001, eq. 4.10.46)

$$M^{\text{mix}} = \begin{bmatrix} \frac{\partial^2 T(x^r, x^s)}{\partial x_1^s \partial x_1^r} & \frac{\partial^2 T(x^r, x^s)}{\partial x_1^s \partial x_2^r} \\ \frac{\partial^2 T(x^r, x^s)}{\partial x_2^s \partial x_1^r} & \frac{\partial^2 T(x^r, x^s)}{\partial x_2^s \partial x_2^r} \end{bmatrix} ; \quad (2.3)$$

(x_1^s, x_2^s) and (x_1^r, x_2^r) are the local Cartesian coordinates of the source and receiver.

For a reflected wave recorded at a horizontal surface, equation (2.2) can be reduced to

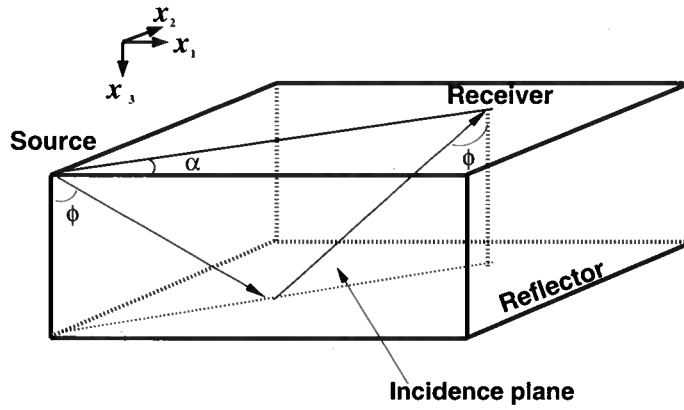


Figure 2.1. Reflected ray in a homogeneous horizontal orthorhombic layer with a horizontal symmetry plane. The ray lies in the incidence plane, although the corresponding phase-velocity vector may point out of plane.

the following function of the traveltime T (see Appendix A):

$$L(R, S) = L(x, \alpha) = (\cos \phi^s \cos \phi^r)^{1/2} \left[\frac{\partial^2 T}{\partial x^2} \frac{\partial T}{\partial x} \frac{1}{x} + \frac{\partial^2 T}{\partial x^2} \frac{\partial^2 T}{\partial \alpha^2} \frac{1}{x^2} - \left(\frac{\partial T}{\partial \alpha} \right)^2 \frac{1}{x^4} \right]^{-1/2} \quad (2.4)$$

where x is the source-receiver offset, and α is the azimuth of the source-receiver line. Equation (7.2) is valid for pure (non-converted) modes in laterally homogeneous (but possible vertically heterogeneous) media, regardless of the anisotropic symmetry.

In addition to providing a concise representation of the spreading $L(R, S)$ in terms of the reflection traveltime $T(x, \alpha)$, equation (7.2) helps to gain insight into the influence of both polar and azimuthal velocity variations on geometrical spreading. The first term in the brackets coincides with the geometrical-spreading factor for horizontally layered VTI media (Ursin and Hokstad, 2003), where the traveltime T is independent of the azimuth α . Note, however, that even this term is distorted by azimuthal anisotropy because the traveltime derivatives with respect to offset vary with α . The second and third term appear only in azimuthally anisotropic media.

Geometrical spreading in homogeneous orthorhombic media

Effective orthorhombic models, appropriate for one or two fracture sets, are considered typical for naturally fractured reservoirs (Schoenberg and Helbig, 1997; Bakulin et al., 2000). Here, we apply the general expression (7.2) to reflections from the bottom of a single horizontal orthorhombic layer with a horizontal symmetry plane (Figure 1). The incidence and reflection group angles for this model are equal to each other (i.e., $\phi^s = \phi^r = \phi$), and

equation (7.2) becomes

$$L(x, \alpha) = \cos \phi \left[\frac{\partial^2 T}{\partial x^2} \frac{\partial T}{\partial x} \frac{1}{x} + \frac{\partial^2 T}{\partial x^2} \frac{\partial^2 T}{\partial \alpha^2} \frac{1}{x^2} - \left(\frac{\partial T}{\partial \alpha} \right)^2 \frac{1}{x^4} \right]^{-1/2}. \quad (2.5)$$

Orthorhombic media with a horizontal symmetry plane have two mutually orthogonal vertical symmetry planes, in which the first derivative $\partial T/\partial \alpha$ goes to zero so equation (2.5) further simplifies to

$$L(x) = \cos \phi \left[\frac{\partial^2 T}{\partial x^2} \frac{\partial T}{\partial x} \frac{1}{x} + \frac{\partial^2 T}{\partial x^2} \frac{\partial^2 T}{\partial \alpha^2} \frac{1}{x^2} \right]^{-1/2}. \quad (2.6)$$

Equation (2.6) confirms the conclusion of Tsvankin (1997, 2001) that the kinematic equivalence between the symmetry planes of orthorhombic and VTI media cannot be extended to geometrical spreading. The second derivative $\partial^2 T/\partial \alpha^2$, which generally does not vanish in the symmetry planes, reflects the influence of azimuthal velocity variations on symmetry-plane amplitudes. This 3D character of geometrical spreading in the symmetry planes is explained by the dependence of the wavefront curvature on both in-plane and out-of-plane (azimuthal) velocity variations. The spreading $L(x, \alpha)$ for source-receiver lines outside the symmetry planes [equation (2.5)] also depends on the first derivative $\partial T/\partial \alpha$.

2.3.1 Nonhyperbolic moveout equation for an orthorhombic layer

Reflection moveout, as well as other signatures of reflected waves in orthorhombic media, is conveniently described using the notation suggested by Tsvankin (1997, 2001). Tsvankin's parameter definitions are based on the analogous form of the Christoffel equation in the symmetry planes of orthorhombic (Figure 2.2) and VTI media. The anisotropic parameters $\epsilon^{(1)}$, $\delta^{(1)}$, and $\gamma^{(1)}$ play the roles of Thomsen's (1986) VTI coefficients ϵ , δ , and γ in the vertical symmetry plane $[x_2, x_3]$ (the superscript denotes the orthogonal axis x_1). The similar set of the anisotropic coefficients in the $[x_1, x_3]$ -plane includes $\epsilon^{(2)}$, $\delta^{(2)}$, and $\gamma^{(2)}$. One more anisotropic coefficient, $\delta^{(3)}$, is defined in the horizontal plane $[x_1, x_2]$. The parameter V_{P0} denotes the vertical P-wave velocity, and V_{S0} is the velocity of the vertically propagating S-wave polarized in the x_1 -direction.

Although orthorhombic symmetry is described by a total of nine independent parameters (for a fixed orientation of the symmetry planes), kinematic signatures of P-waves depend only on five parameter combinations. As shown by Grechka and Tsvankin (1999), P-wave reflection traveltime and the operators for dip-moveout (DMO) correction and time migration in homogeneous orthorhombic media are controlled by the NMO velocities from horizontal reflectors in the vertical symmetry planes, $V_{\text{nmo}}^{(1)}$ and $V_{\text{nmo}}^{(2)}$, and three anellipticity coefficients defined as follows:

$$\eta^{(1)} \equiv \frac{\epsilon^{(1)} - \delta^{(1)}}{1 + 2\delta^{(1)}} \approx \epsilon^{(1)} - \delta^{(1)}, \quad (2.7)$$

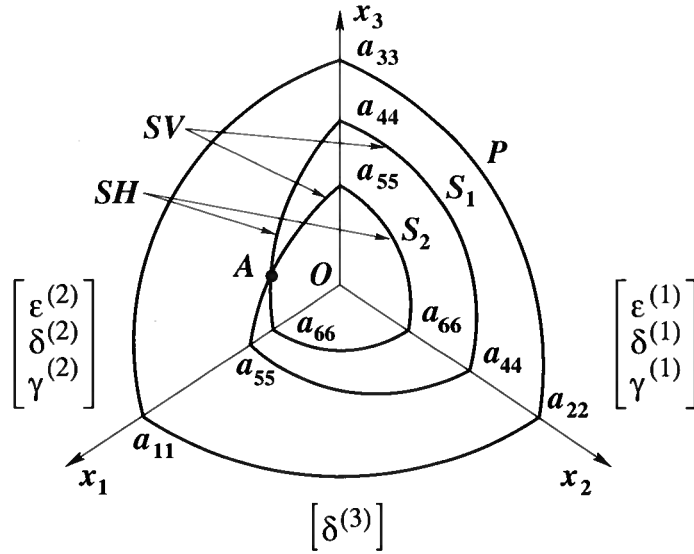


Figure 2.2. Sketch of body-wave phase-velocity surfaces in orthorhombic media (after Grechka et al., 1999). Tsvankin's (1997) parameters are defined in the mutually orthogonal symmetry planes which coincide with the coordinate planes. A marks a point (conical) singularity where the phase velocities of the two S-waves are equal to each other.

$$\eta^{(2)} \equiv \frac{\epsilon^{(2)} - \delta^{(2)}}{1 + 2\delta^{(2)}} \approx \epsilon^{(2)} - \delta^{(2)}, \quad (2.8)$$

$$\eta^{(3)} \equiv \frac{\epsilon^{(1)} - \epsilon^{(2)} - \delta^{(3)}(1 + 2\epsilon^{(2)})}{(1 + 2\epsilon^{(2)})(1 + 2\delta^{(3)})} \approx \epsilon^{(1)} - \epsilon^{(2)} - \delta^{(3)}. \quad (2.9)$$

The long-spread reflection travelttime for orthorhombic media can be described by the general Tsvankin-Thomsen (1994) nonhyperbolic moveout equation with azimuthally varying coefficients:

$$T^2(x, \alpha) = A_0 + A_2(\alpha)x^2 + \frac{A_4(\alpha)x^4}{1 + A(\alpha)x^2}, \quad (2.10)$$

where

$$A_0 \equiv T_0^2, \quad A_2 \equiv \left. \frac{d(T^2)}{d(x^2)} \right|_{x=0} \quad \text{and} \quad A_4 \equiv \frac{1}{2} \frac{d}{d(x^2)} \left[\left. \frac{d(T^2)}{d(x^2)} \right] \right|_{x=0}.$$

Here T_0 is the zero-offset travelttime, A_2 is related to the normal-moveout velocity as $A_2 = V_{\text{nmo}}^{-2}$, and A_4 is the quartic coefficient responsible for nonhyperbolic moveout. The parameter A in the denominator depends on the horizontal group velocity V_{hor} and is designed

to make $T(x)$ convergent at large offsets $x \rightarrow \infty$ (Tsvankin and Thomsen, 1994):

$$A = \frac{A_4}{V_{\text{hor}}^{-2} - V_{\text{nmo}}^{-2}}. \quad (2.11)$$

The hyperbolic coefficient A_2 in equation (2.10) can be obtained from the results of Grechka and Tsvankin (1999), who proved that the azimuthal variation of NMO velocity typically has a simple elliptical form even in arbitrarily anisotropic, heterogeneous media. For a horizontal orthorhombic layer in which the vertical symmetry planes coincide with the coordinate planes $[x_1, x_3]$ and $[x_2, x_3]$, the axes of the NMO ellipse are aligned with the x_1 and x_2 directions, which yields (for P-waves):

$$A_2(\alpha) = A_2^{(1)} \sin^2 \alpha + A_2^{(2)} \cos^2 \alpha, \quad (2.12)$$

$$A_2^{(1)} = \frac{1}{\left(V_{\text{nmo}}^{(1)}\right)^2} = \frac{1}{V_{P0}^2 (1 + 2\delta^{(1)})}, \quad (2.13)$$

$$A_2^{(2)} = \frac{1}{\left(V_{\text{nmo}}^{(2)}\right)^2} = \frac{1}{V_{P0}^2 (1 + 2\delta^{(2)})}; \quad (2.14)$$

the azimuth α is computed with respect to the x_1 -axis.

The azimuthally dependent P-wave quartic moveout coefficient A_4 in a horizontal orthorhombic layer has the form (Al-Dajani *et al.*, 1998)

$$A_4(\alpha) = A_4^{(1)} \sin^4 \alpha + A_4^{(2)} \cos^4 \alpha + A_4^{(x)} \sin^2 \alpha \cos^2 \alpha, \quad (2.15)$$

$$A_4^{(1)} = \frac{-2\eta^{(1)}}{T_0^2 \left(V_{\text{nmo}}^{(1)}\right)^4}, \quad (2.16)$$

$$A_4^{(2)} = \frac{-2\eta^{(2)}}{T_0^2 \left(V_{\text{nmo}}^{(2)}\right)^4}, \quad (2.17)$$

$$A_4^{(x)} = \frac{2}{T_0^2 \left(V_{\text{nmo}}^{(1)}\right)^2 \left(V_{\text{nmo}}^{(2)}\right)^2} \left[1 - \sqrt{\frac{(1 + 2\eta^{(1)}) (1 + 2\eta^{(2)})}{1 + 2\eta^{(3)}}} \right]. \quad (2.18)$$

Here $A_4^{(1)}$ and $A_4^{(2)}$ are the symmetry-plane coefficients and $A_4^{(x)}$ is a cross-term that contributes in off-symmetry directions. Al-Dajani *et al.* (1998) approximated V_{hor} in equation (2.11) by the horizontal phase velocity, and demonstrated that equation (2.10) with the moveout coefficients given by equations (2.11), (2.12), and (2.15) is sufficiently accurate for P-wave moveout in models with substantial azimuthal anisotropy. The algorithm of Al-Dajani *et al.* (1998), based on equation (2.10), is used below in the numerical modeling of the geometrical spreading in an orthorhombic layer.

A simplified version of equation (2.10) can be obtained by exploring the approximate kinematic equivalence between the vertical planes of orthorhombic and VTI media. In the limit of weak anisotropy, out-of-plane phenomena in a horizontal orthorhombic layer have no influence on kinematic signatures including reflection traveltimes (Tsvankin, 2001, p. 164). Also, the P-wave phase velocity in any vertical plane of weakly anisotropic orthorhombic media can be described by Thomsen's (1986) VTI equation with azimuthally-dependent coefficients ϵ and δ [Tsvankin, 2001, equation (1.107)]. Therefore, P-wave reflection moveout in a horizontal orthorhombic layer can be approximated by the VTI equation of Alkhalifah and Tsvankin (1995) with the appropriate parameters V_{nmo} and η for each azimuth:

$$T^2(x, \alpha) = T_0^2 + \frac{x^2}{V_{\text{nmo}}^2(\alpha)} - \frac{2\eta(\alpha)x^4}{V_{\text{nmo}}^2(\alpha)[T_0^2 V_{\text{nmo}}^2(\alpha) + (1 + 2\eta(\alpha))x^2]}. \quad (2.19)$$

$V_{\text{nmo}}(\alpha)$ in equation (2.19) is determined from equations (2.12)–(2.14),

$$V_{\text{nmo}}^2(\alpha) = A_2^{-1} = \frac{\left(V_{\text{nmo}}^{(1)}\right)^2 \left(V_{\text{nmo}}^{(2)}\right)^2}{\left(V_{\text{nmo}}^{(1)}\right)^2 \cos^2 \alpha + \left(V_{\text{nmo}}^{(2)}\right)^2 \sin^2 \alpha}, \quad (2.20)$$

and the linearized azimuthally dependent parameter η is given by (Pech and Tsvankin, 2004)

$$\eta(\alpha) = \eta^{(1)} \sin^2 \alpha - \eta^{(3)} \sin^2 \alpha \cos^2 \alpha + \eta^{(2)} \cos^2 \alpha. \quad (2.21)$$

The nonhyperbolic term in equation (2.19) can be derived from equation (2.10) by using the VTI relationships

$$A_4(\alpha) = -\frac{2\eta(\alpha)}{T_0^2 V_{\text{nmo}}^4(\alpha)}, \quad A(\alpha) = \frac{1 + 2\eta(\alpha)}{T_0^2 V_{\text{nmo}}^2(\alpha)}. \quad (2.22)$$

Although the linearization in the anisotropic parameters implied by the weak-anisotropy approximation formally requires dropping the coefficient $\eta(\alpha)$ from the denominator of equation (2.19), the complete denominator of the original VTI equation can be retained to increase the accuracy at large source-receiver offsets. Here, equation (2.19) is used only to obtain analytic expressions for the geometrical spreading in the weak-anisotropy approximation.

2.3.2 Geometrical spreading as a function of moveout coefficients

The derivatives of the traveltimes with respect to offset and azimuth needed to obtain the geometrical spreading $L(x, \alpha)$ from equation (2.5) can be found using the non-hyperbolic moveout equation (2.10). Explicit expressions for the traveltimes derivatives in terms of the azimuthally dependent parameters $A_2(\alpha)$, $A_4(\alpha)$, and $A(\alpha)$ are given in Appendix B. Substitution of equations (2.11), (2.12), and (2.15) yields $L(x, \alpha)$ as a function of the medium parameters and the group angle. The group angle ϕ for a single orthorhombic layer can be found in a straightforward way from the reflector depth ($T_0 V_{P0}/2$) and offset

$$x: \cos \phi = \frac{T_0 V_{P0}}{\sqrt{x^2 + T_0^2 V_{P0}^2}}.$$

While the derived equation is well-suited for numerical modeling, it does not provide insight into the dependence of the geometrical spreading on the anisotropic parameters. Therefore, next we apply the weak-anisotropy approximation based on the generalized VTI equation (2.19). The traveltime derivatives in equation (2.5) are obtained from equation (2.19) and then linearized in the anellipticity parameters $\eta^{(1,2,3)}$. Further linearization of equation (2.5) yields the weak-anisotropy approximation for the geometrical spreading discussed below.

2.3.3 Analysis of the weak-anisotropy approximation

Geometrical spreading in the symmetry planes. While the full linearized expression for geometrical spreading is still rather long, it takes a much more concise form in the vertical symmetry planes. For the symmetry plane $[x_1, x_3]$, we find the inverse relative spreading as

$$L^{-1}(x) = \cos^{-1} \phi \frac{A + Bx^2 + Cx^4}{V_{\text{nmo}}^{(1)} V_{\text{nmo}}^{(2)} \left[T_0^2 \left(V_{\text{nmo}}^{(2)} \right)^2 + x^2 \right]^{\frac{3}{2}}}, \quad (2.23)$$

where

$$\cos \phi = \frac{T_0 V_{P0}}{\sqrt{x^2 + T_0^2 V_{P0}^2}}, \quad (2.24)$$

$$A = T_0^5 \left(V_{\text{nmo}}^{(2)} \right)^6, \quad (2.25)$$

$$B = T_0^3 \left(V_{\text{nmo}}^{(2)} \right)^2 \left[2 \left(1 - 4\eta^{(2)} \right) \left(V_{\text{nmo}}^{(2)} \right)^2 + \left(\eta^{(2)} + \eta^{(3)} - \eta^{(1)} \right) \left(V_{\text{nmo}}^{(1)} \right)^2 \right], \quad (2.26)$$

$$C = T_0 \left[\left(1 + \eta^{(2)} \right) \left(V_{\text{nmo}}^{(2)} \right)^2 + \left(\eta^{(2)} + \eta^{(3)} - \eta^{(1)} \right) \left(V_{\text{nmo}}^{(1)} \right)^2 \right]. \quad (2.27)$$

At zero offset, the factor L^{-1} becomes $1/(T_0 V_{\text{nmo}}^{(1)} V_{\text{nmo}}^{(2)})$, which is an exact expression that can be obtained directly from the wavefront curvatures for any strength of anisotropy. As follows from equations (2.13) and (2.14) for the NMO velocities, the geometrical spreading at vertical incidence is governed by two anisotropic coefficients, $\delta^{(1)}$ and $\delta^{(2)}$. For VTI media, $V_{\text{nmo}}^{(1)} = V_{\text{nmo}}^{(2)}$, and L^{-1} at zero offset reduces to $1/(T_0 V_{\text{nmo}}^2)$; this result was previously obtained by Tsvankin (1995) and Ursin and Hokstad (2003). If the medium is isotropic, L^{-1} further simplifies to the familiar expression $1/(T_0 V_{P0}^2)$ (Newman, 1973).

The factors B and C in equation (2.23) can be called the “near-offset” and “far-offset” spreading coefficients, respectively. It should be emphasized that B and C include terms dependent on both in-plane and out-of-plane traveltime (and, therefore, velocity) variations. P-wave reflection traveltime in the incidence plane is controlled just by the NMO velocity $V_{\text{nmo}}^{(2)}$ and the anisotropic parameter $\eta^{(2)}$ (Grechka and Tsvankin, 1999; Tsvankin, 2001). Hence, the term $(1 - 4\eta^{(2)}) (V_{\text{nmo}}^{(2)})^2$ in the coefficient B represents the in-plane contribution,

which coincides with the corresponding (near-offset) spreading factor for VTI media. The other term in the expression for B , $[(\eta^{(2)} - \eta^{(1)} + \eta^{(3)}) (V_{\text{nmo}}^{(1)})^2]$, is entirely due to azimuthal anisotropy (i.e., to a nonzero value of the second traveltine derivative with respect to α). This term vanishes in VTI media where $\eta^{(3)} = 0$ and $\eta^{(1)} = \eta^{(2)}$. Similarly, the far-offset coefficient C contains the in-plane term $[(1 + \eta^{(2)}) (V_{\text{nmo}}^{(2)})^2]$ and exactly the same out-of-plane term as that in the expression for B .

The inverse spreading L^{-1} in the symmetry plane $[x_2, x_3]$ can be obtained from equations (2.23)–(2.27) by simply switching the superscripts (1) and (2) in the NMO velocities and the coefficients η . A more detailed comparison of the geometrical spreading in the symmetry planes of orthorhombic media with that in VTI media can be found in the numerical examples below.

Azimuthal variation of geometrical spreading. Since azimuthal AVO analysis often operates with prestack amplitudes measured at a fixed offset, here we analyze the azimuthally-varying spreading factor $L^{-1}(\alpha, x)$ for $x = \text{const}$. Using equations (2.13) and (2.14) for the symmetry-plane NMO velocities and linearizing both the x^2 - and x^4 -terms in equation (2.19) in the anisotropic parameters yields

$$\begin{aligned} T^2(x, \alpha) &= T_0^2 + x^2 \frac{1 - \delta^{(1)} - \delta^{(2)} + (\delta^{(2)} - \delta^{(1)}) \cos 2\alpha}{V_{P0}^2} \\ &- 2x^4 \frac{\eta^{(2)} \cos^2 \alpha + \eta^{(1)} \sin^2 \alpha - \eta^{(3)} \cos^2 \alpha \sin^2 \alpha}{T_0^2 V_{P0}^4 \left(1 + \frac{x^2}{T_0^2 V_{P0}^2}\right)}. \end{aligned} \quad (2.28)$$

Substituting moveout equation (2.28) into equation (2.5) and carrying out further linearization in the anisotropic parameters, we obtain the inverse geometrical spreading as

$$L^{-1}(x, \alpha) = D(x) + E(\alpha) \left[\frac{x}{T_0 V_{P0}} \right]^2 + F(\alpha) \left[\frac{x}{T_0 V_{P0}} \right]^4 + \dots \quad (2.29)$$

Here, $D(x)$ is an azimuthally-independent term that would coincide with L^{-1} in VTI media (the model becomes VTI if the anisotropic coefficients in the vertical symmetry planes are identical, and $\eta^{(3)} = 0$). The azimuthally-varying terms in equation (2.29) are expanded in x^2 , and powers of x higher than four are neglected. The coefficients E and F are given by

$$E(\alpha) = \frac{V_{P0}^3 T_0^4}{(V_{P0}^2 T_0^2 + x^2)^{\frac{5}{2}}} \left[3 \left(\eta^{(1)} - \eta^{(2)} \right) - \left(\delta^{(1)} - \delta^{(2)} \right) \right] \cos 2\alpha; \quad (2.30)$$

$$\begin{aligned} F(\alpha) &= \frac{V_{P0}^3 T_0^4}{(V_{P0}^2 T_0^2 + x^2)^{\frac{5}{2}}} \\ &\left\{ \left[\frac{3}{2} \left(\delta^{(1)} - \delta^{(2)} \right) + 9 \left(\eta^{(1)} - \eta^{(2)} \right) \right] \cos 2\alpha + \frac{9}{8} \eta^{(3)} \cos 4\alpha \right\}. \end{aligned} \quad (2.31)$$

The coefficient $E(\alpha)$ is responsible for the azimuthal dependence of the geometrical spreading at near offsets. Since $E(\alpha)$ is proportional to $\cos 2\alpha$, for small x the function $L^{-1}(\alpha)$ traces out a curve close to an ellipse. In contrast, the far-offset coefficient $F(\alpha)$ contains both $\cos 2\alpha$ and $\cos 4\alpha$, and the form of $L^{-1}(\alpha)$ may substantially deviate from elliptical; this is illustrated by the numerical examples in the next section.

The magnitude of the azimuthal variation of geometrical spreading is controlled by the differences $(\delta^{(1)} - \delta^{(2)})$, $(\eta^{(1)} - \eta^{(2)})$ and, at far offsets, by the coefficient $\eta^{(3)}$. If $\delta^{(1)} = \delta^{(2)}$, $\eta^{(1)} = \eta^{(2)}$, and $\eta^{(3)} = 0$, P-wave velocity becomes azimuthally independent, and for purposes of computing P-wave geometrical spreading the orthorhombic medium becomes equivalent to VTI.

2.3.4 Numerical example

The numerical example presented here is designed to illustrate the following properties of the inverse spreading L^{-1} in an orthorhombic layer:

- The influence of azimuthal anisotropy on L^{-1} in the vertical symmetry planes.
- The azimuthal variation of L^{-1} at a fixed source-receiver offset.
- The spatial variation of L^{-1} expressed as a function of offset and azimuth.
- The accuracy of the weak-anisotropy approximation for L^{-1} .

We use an orthorhombic model formed by parallel vertical penny-shaped cracks embedded in a VTI background. The stiffness coefficients for this model are given in Schoenberg and Helbig (1997), and the corresponding anisotropic parameters, listed in the caption of Figure 2.3, are taken from Tsvankin (1997). Although this model has a substantial azimuthal velocity variation, it is dominated by the VTI component, with both ϵ coefficients close to 0.3.

As before, we assume that the coordinate planes coincide with the symmetry planes of the orthorhombic layer. The inverse spreading L^{-1} is found using the formulation based on equations (2.5) and (2.10) without making any further approximations in computing the traveltime derivatives and the spreading factor itself. For comparison, we also calculate the weak-anisotropy approximation for L^{-1} by employing the moveout equation (2.19) and linearizing the spreading in the anisotropic coefficients (see the previous section).

Figure 2.3 displays the inverse spreading L^{-1} (normalized by L^{-1} in the corresponding isotropic model) in the vertical symmetry planes of the layer. Clearly, the influence of anisotropy leads to significant distortions of geometrical spreading in a wide range of offsets for both symmetry planes. As shown by Tsvankin (1995, 2001) for VTI media, the influence of anisotropy causes the amplitude (e.g., the inverse spreading) to decrease with increasing offset if the difference $\epsilon - \delta$ is positive (i.e., $\eta > 0$). Figure 2.3 confirms that this conclusion remains valid for the symmetry planes of orthorhombic media with moderate azimuthal anisotropy. Indeed, the η coefficients in both vertical symmetry planes ($\eta^{(1)}$ and $\eta^{(2)}$) are positive, and the normalized factor L^{-1} decreases with offset at near-vertical incidence.

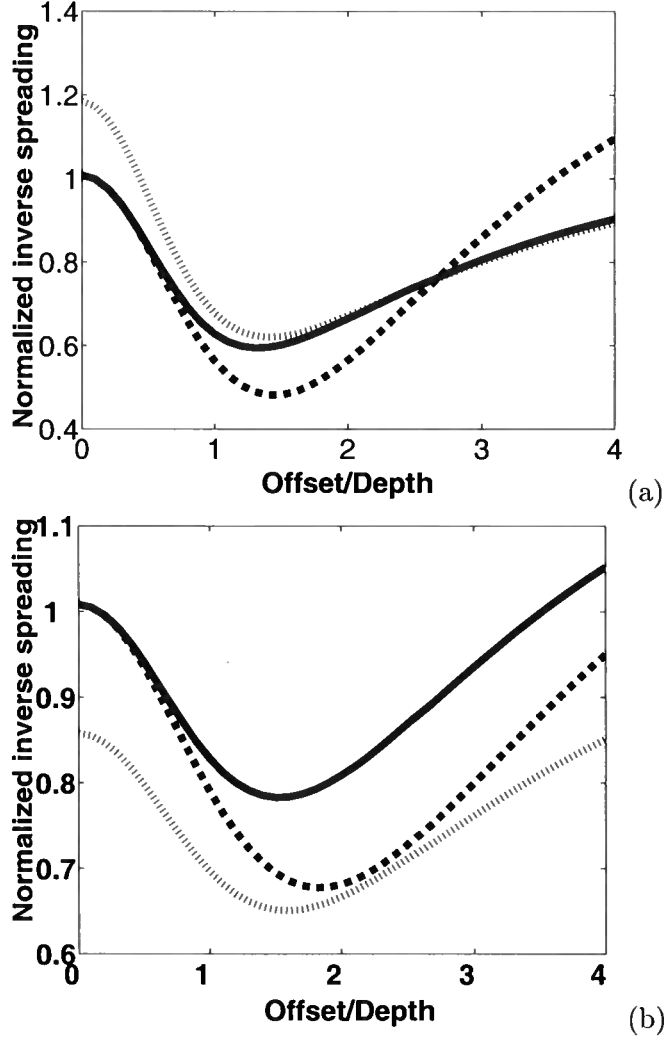


Figure 2.3. Normalized inverse spreading L^{-1} as a function of the offset-to-depth ratio in the symmetry planes $[x_1, x_3]$ (a) and $[x_2, x_3]$ (b) of a horizontal orthorhombic layer. The solid line is computed using equations (2.5) and (2.10), the dashed line is the weak-anisotropy approximation, and the dotted line is L^{-1} in the reference VTI model. The model parameters are $V_{P0} = 2.437$ km/s, $\epsilon^{(1)} = 0.329$, $\epsilon^{(2)} = 0.258$, $\delta^{(1)} = 0.083$, $\delta^{(2)} = -0.078$, and $\delta^{(3)} = -0.106$. The corresponding P-wave moveout parameters are $V_{\text{nmo}}^{(1)} = 2.632$ km/s, $V_{\text{nmo}}^{(2)} = 2.239$ km/s, $\eta^{(1)} = 0.211$, $\eta^{(2)} = 0.398$, and $\eta^{(3)} = 0.193$. The inverse spreading L^{-1} is normalized by its value in the corresponding isotropic layer with the velocity $V_{P0} = 2.437$ km/s.

Comparison with the spreading in the reference VTI medium (dotted line) helps to quantify the influence of azimuthal anisotropy in both symmetry planes. It is interesting that azimuthal anisotropy changes the spreading factor even at vertical incidence, where for orthorhombic media $L^{-1} = 1/(T_0 V_{\text{nmo}}^{(1)} V_{\text{nmo}}^{(2)})$, while for VTI media $L^{-1} = 1/(T_0 V_{\text{nmo}}^2)$. For example, if we substitute the NMO velocity in the $[x_1, x_3]$ symmetry plane into the VTI expression, we get a value that is 18% larger than the actual L^{-1} (Figure 2.3a).

As follows from the weak-anisotropy approximation discussed in the previous section, the influence of azimuthal velocity variations on the offset-dependent part of the factor L^{-1} in the $[x_1, x_3]$ symmetry plane is controlled by the combination $(\eta^{(2)} - \eta^{(1)} + \eta^{(3)})$ of the anellipticity coefficients. Since for our model this combination is positive and relatively large (0.38), L^{-1} in the $[x_1, x_3]$ -plane initially decreases with offset slower than that in the corresponding VTI medium (Figure 2.3a). For offset-to-depth ratios exceeding two, however, the factor L^{-1} almost coincides with the VTI value, which contradicts the weak-anisotropy result. Overall, the influence of azimuthal anisotropy is so significant that it is not acceptable to apply 2D amplitude analysis even in the symmetry planes of azimuthally anisotropic media.

Similarly, the factor L^{-1} in the $[x_2, x_3]$ symmetry plane contains the “out-of-plane” term proportional to $(\eta^{(1)} - \eta^{(2)} + \eta^{(3)})$. For the model at hand, however, this term is close to zero (0.006), and the offset dependence of the geometrical spreading in the $[x_2, x_3]$ -plane is close to that in the reference VTI medium (Figure 2.3b).

Figure 2.3 also helps to evaluate the accuracy of the weak-anisotropy approximation for a model that can be characterized as moderately-to-strongly anisotropic in terms of the magnitude of P-wave velocity variations. While the weak-anisotropy solution is exact at $x = 0$ (because we did not linearize the NMO velocities in the denominator of L^{-1}), it rapidly deviates from the exact factor L^{-1} with increasing offset. Still, the approximation correctly predicts the general character of the function $L^{-1}(x)$ and remains accurate for offset-to-depth ratios of up to about one.

The azimuthal variation of the normalized spreading L^{-1} at two different offsets is plotted in Figure 2.4. Since the geometrical spreading in our model is symmetric with respect to both vertical coordinate planes, the signature of L^{-1} is repeated in each quadrant. For the offset equal to the reflector depth, the azimuthal variation of L^{-1} is close to elliptical, as predicted by the weak-anisotropy approximation (Figure 2.4a). The fractional difference between the values of L^{-1} in the symmetry planes, which determines the overall magnitude of the azimuthal variation of the inverse geometrical spreading, is about 30%. Hence, for this model the eccentricity of the “geometrical-spreading ellipse” exceeds that of the NMO ellipse (18%). For larger offset-to-depth ratios, the shape of the curve $L^{-1}(\alpha)$ becomes more complicated and, in agreement with the weak-anisotropy approximation (2.31) for the x^4 -term, deviates from an ellipse (Figure 2.4b).

A complete picture of the spatial variations of the spreading factor in our model is given in Figure 2.5a, where the factor L^{-1} is computed as a function of both offset and azimuth. The combined influence of polar and azimuthal anisotropy creates a rather complicated pattern of the normalized factor L^{-1} , with substantial azimuthal variations and pronounced deviations from the corresponding isotropic values. The largest anisotropy-induced distur-

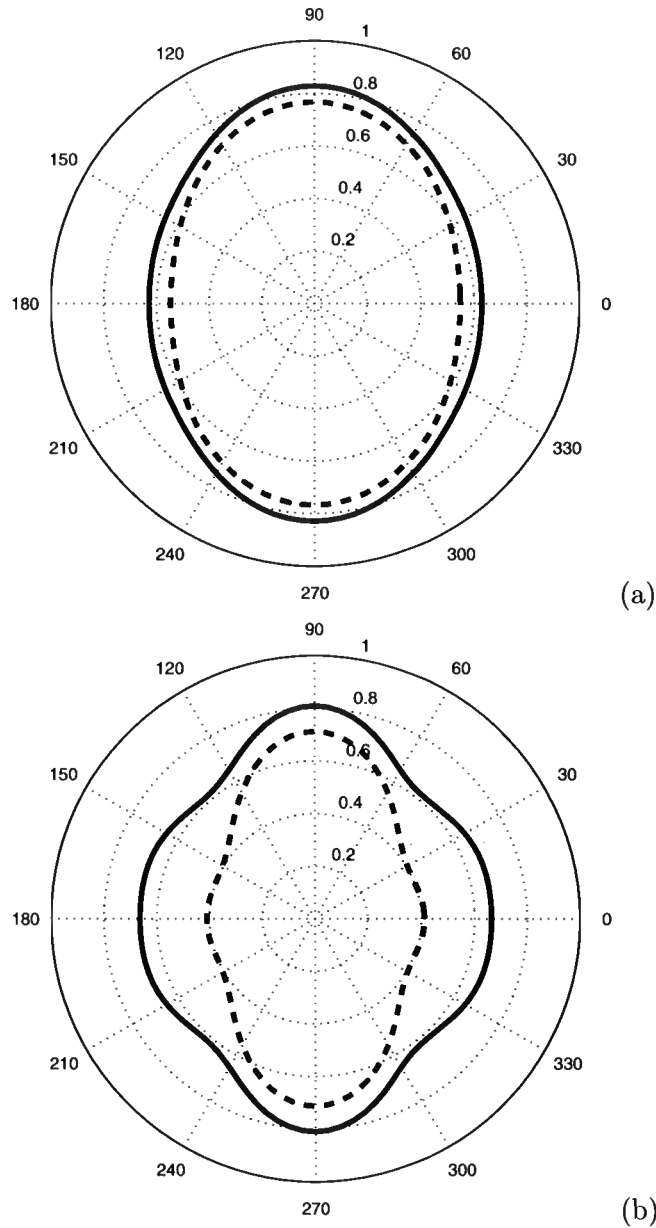


Figure 2.4. Azimuthal variation of the normalized spreading L^{-1} for the model from Figure 2.3; the offset-to-depth ratio is equal to one (a) and two (b). The azimuth α (numbers on the perimeter) is measured with respect to the x_1 -axis. The solid line is computed using equations (2.5) and (2.10), the dashed line is the weak-anisotropy approximation.

tions of the geometrical spreading, reaching 40%, are observed near the $[x_1, x_3]$ -plane for offset-to-depth ratios of about 1.5.

The significant azimuthal variation of L^{-1} at near offsets is partly caused by the opposite signs of the δ coefficients in the vertical symmetry planes. In Figure 2.5b we changed the sign of $\delta^{(2)}$ (the other model parameters remained the same), which reduced the differences between the symmetry-plane NMO velocities ($V_{\text{nmo}}^{(1)}$ and $V_{\text{nmo}}^{(2)}$) and between the corresponding η coefficients ($\eta^{(1)}$ and $\eta^{(2)}$). Although the geometrical spreading did become much less dependent on azimuth at near offsets, the azimuthal variation of L^{-1} at moderate and far offsets in Figure 2.5b is still quite pronounced.

2.4 Comparison with dynamic ray tracing

To verify the accuracy of our algorithm [equation (4)] based on the nonhyperbolic moveout equation (2.10), we compared our results with the spreading computed by dynamic ray-tracing code ANRAY (Gajewski and Pšenčík, 1990). The comparison was carried out for a single orthorhombic layer with the parameters of the Schoenberg-Helbig model used previously¹ and a more complicated medium composed of two orthorhombic and two isotropic layers (Table 1). The moveout coefficients were found by fitting equation (2.10) to ray-traced traveltimes using the least-squares method. The group angle for the layered model was estimated from the slope of the traveltime curve and the velocity in the subsurface isotropic layer.

For both models, the geometrical spreading calculated by our method is close to the results of dynamic ray tracing for a wide range of offsets (Figures 6 and 7). Small deviations from the ray-traced values can be explained by the approximate nature of the Tsvankin-Thomsen nonhyperbolic moveout equation and, possibly, by numerical errors in ANRAY. Note that since equation (4) includes second-order traveltime derivatives, the spreading computed by our algorithm is sensitive to relatively small correlated errors in the moveout function.

Still, Figure 7 demonstrates that equation (2.10) adequately describes P-wave moveout not just for a single layer, but also for a stack of azimuthally anisotropic layers with aligned vertical symmetry planes. For layered media, all moveout coefficients become effective values that depend on the interval NMO velocities and η parameters.

2.5 Discussion and conclusions

Although geometrical spreading of reflected waves is determined by the medium properties around the whole raypath, it can be obtained from the reflection traveltime and the group angles at the source and receiver locations. Using ray theory, we showed that for

¹To facilitate the conversion from the relative spreading produced by our algorithm to the absolute spreading computed by ANRAY, we placed a thin (10 m) isotropic layer on top of the 1000 m-thick orthorhombic layer.

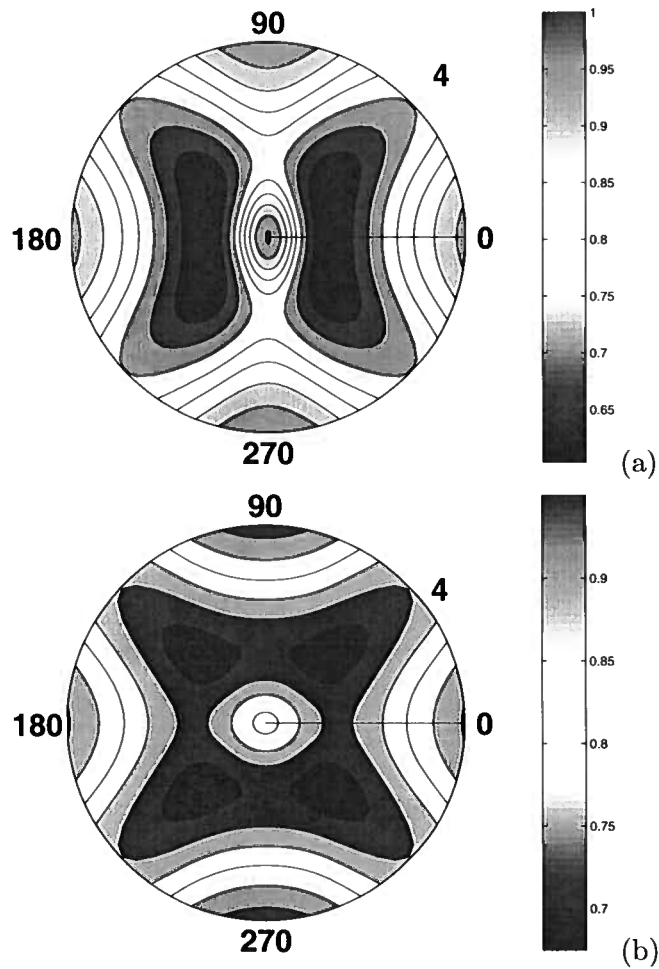


Figure 2.5. Map of the normalized inverse spreading L^{-1} as a function of offset and azimuth. Plot (a) is computed for the model from Figure 2.3; in plot (b), the sign of the parameter $\delta^{(2)}$ was changed from negative to positive (i.e., $\delta^{(2)} = 0.078$). The offset-to-depth ratio varies from zero to four.

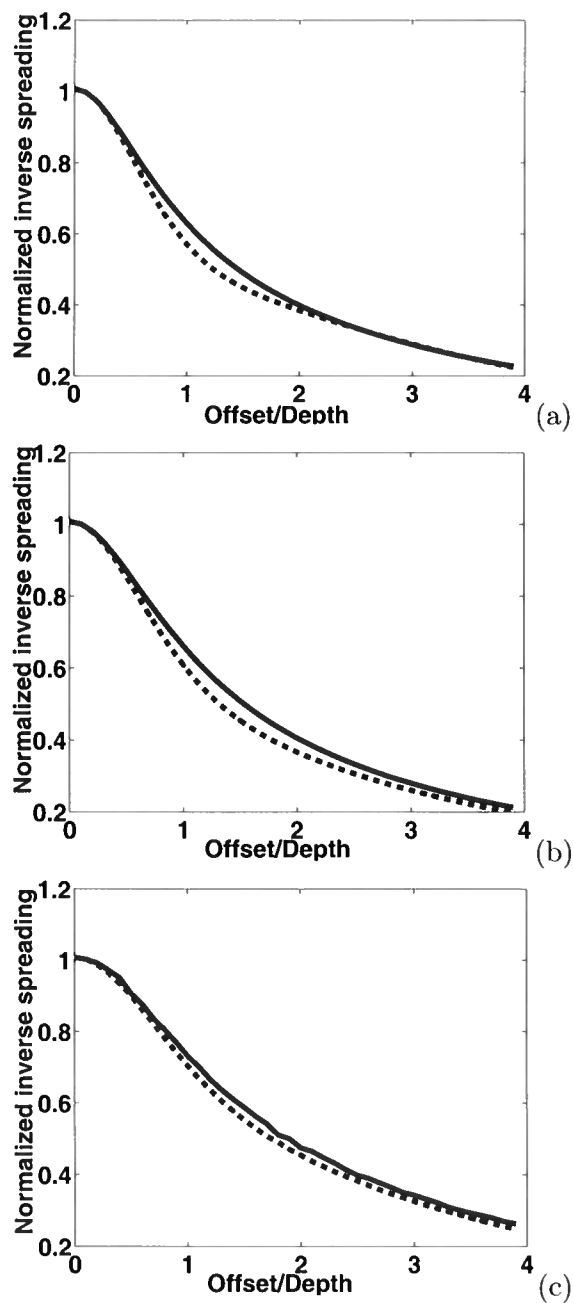


Figure 2.6. Comparison of the inverse relative spreading computed by our method (dashed line) and code ANRAY (solid) for the model from Figure 2.3. The source-receiver line is oriented (a) along the x_1 -axis; (b) at 45° with the x_1 -axis; and (c) along the x_2 -axis.

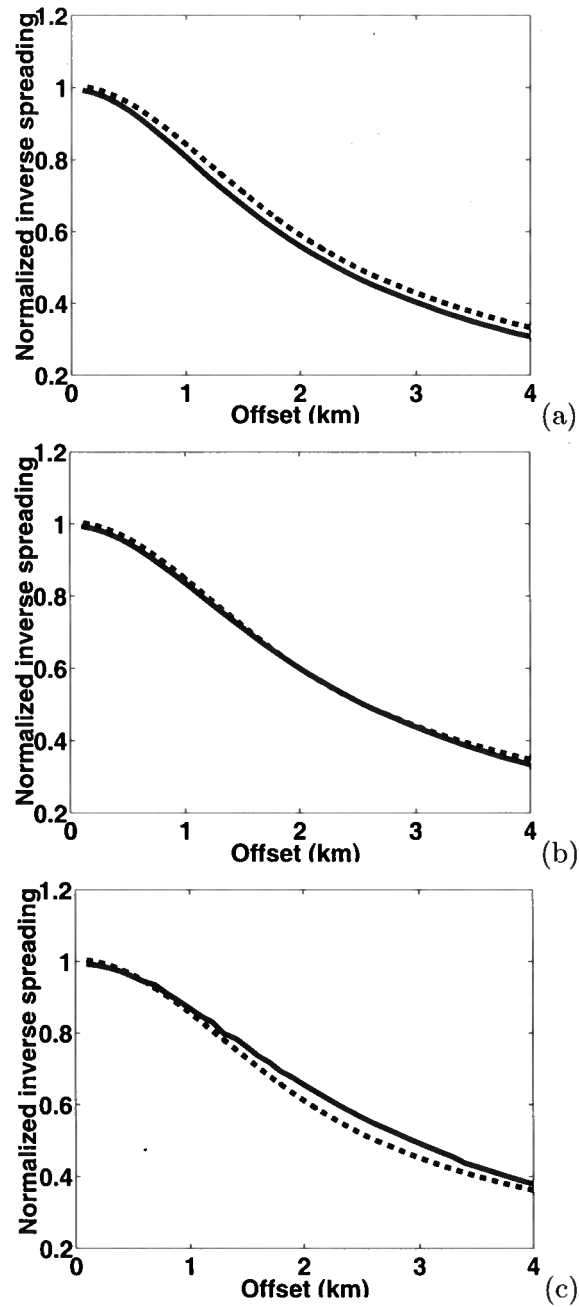


Figure 2.7. Comparison of the inverse relative spreading computed by our method (dashed line) and code ANRAY (solid) for the layered orthorhombic model from Table 1 (we used the reflection from the bottom of the third layer). The source-receiver line is oriented (a) along the x_1 -axis; (b) at 45° with the x_1 -axis; and (c) along the x_2 -axis.

	Layer 1	Layer 2	Layer 3	Layer 4
Symmetry type	ISO	ORTH	ORTH	ISO
V_{P0} (km/s)	1.5	2.437	3.0	3.2
Thickness (km)	0.2	0.9	0.9	0.5
$\epsilon^{(1)}$	0	0.329	0.25	0
$\epsilon^{(2)}$	0	0.258	0.15	0
$\delta^{(1)}$	0	0.083	0.05	0
$\delta^{(2)}$	0	-0.078	-0.1	0
$\delta^{(3)}$	0	-0.106	0.15	0

Table 2.1. Parameters of a four-layer model that includes two orthorhombic layers (layers 2 and 3) with aligned vertical symmetry planes.

pure (non-converted) modes recorded above a horizontally layered medium, the relative geometrical spreading can be expressed as a simple function of the traveltime derivatives with respect to offset and azimuth and the group angles at the surface. Although this equation does not account for lateral heterogeneity, it involves no restrictions on the number of layers above the reflector or the type of symmetry in each layer.

To describe the geometrical spreading of P-waves in orthorhombic media, we combined our general result with the Tsvankin-Thomsen (1994) nonhyperbolic moveout equation for a homogeneous, horizontal orthorhombic layer. P-wave reflection traveltime and, therefore, the geometrical spreading for this model is governed by the NMO velocities $V_{\text{nmo}}^{(1)}$ and $V_{\text{nmo}}^{(2)}$ in the vertical symmetry planes and the anellipticity coefficients $\eta^{(1)}$, $\eta^{(2)}$, and $\eta^{(3)}$. To explain the dependence of the inverse spreading L^{-1} on these parameters, we employed the weak-anisotropy approximation based on linearization in the anisotropic coefficients. The analytic results were verified by numerical tests for an orthorhombic model formed by vertical penny-shaped cracks embedded in a VTI matrix.

Although the geometrical-spreading signature in an orthorhombic layer is repeated in each quadrant, the variation of the factor L^{-1} with offset and azimuth has a rather complicated character. For the model used here, the error of the isotropic equation for the geometrical spreading reaches a maximum of 40% in the intermediate offset range (i.e., for the offset-to-depth ratio between one and two). The azimuthal variation $L^{-1}(\alpha)$ for a fixed offset is close to elliptical at relatively small offset-to-depth ratios of up to one. For larger offsets, $L^{-1}(\alpha)$ deviates from an ellipse and may have intermediate minima or maxima between the symmetry planes.

Both analytic and numerical results show that the spreading factor L^{-1} is substantially influenced by azimuthal velocity variations even in the vertical symmetry planes. At zero offset (vertical incidence), the exact inverse geometrical spreading is given by a simple equation that involves only the NMO velocities in both symmetry planes: $L^{-1} = 1/(T_0 V_{\text{nmo}}^{(1)} V_{\text{nmo}}^{(2)})$. The offset-dependent part of L^{-1} in the symmetry planes can be separated (in the weak-

anisotropy approximation) into the in-plane term, identical to the factor L^{-1} in the corresponding VTI medium, and the out-of-plane term associated with azimuthal anisotropy. In the $[x_1, x_3]$ -plane, the contribution of azimuthal velocity variation is proportional to the combination $(\eta^{(2)} - \eta^{(1)} + \eta^{(3)})$, and in the $[x_2, x_3]$ -plane to $(\eta^{(1)} - \eta^{(2)} + \eta^{(3)})$.

The large magnitude of the anisotropy-induced distortions of the factor L^{-1} means that reliable interpretation of the wide-azimuth AVO response for media with azimuthally anisotropic overburden is impossible without properly correcting for the geometrical spreading. The estimation and removal of geometrical spreading can be accomplished by applying equation (7.2) with the best-fit traveltime function. Analytic representations of reflection moveout can facilitate the spreading correction by providing a smooth accurate approximation for the measured traveltimes.

In practice, however, complications may arise from the high sensitivity of the geometrical spreading to lateral heterogeneity, small errors in the best-fit traveltimes, distortions in the group (ray) angles, etc. For example, it is difficult to estimate the group angles at the source and receiver locations using just the acquisition geometry and traveltime data, unless the subsurface layer is isotropic (Ursin and Hokstad, 2003). Even for the homogeneous orthorhombic model studied above, the group angle $\phi^s = \phi^r$ can be found in a straightforward way only if the layer thickness is known (see Figure 1). Practical issues involved in the geometrical-spreading correction for layered azimuthally anisotropic media will be investigated in more detail in a sequel paper.

2.6 References

- Al-Dajani, A., Tsvankin, I., and Toksöz, M.N., 1998, Nonhyperbolic reflection moveout for azimuthally anisotropic media: 68th Ann. Internat. Mtg., Soc. Expl. Geophys., Expanded Abstracts, 1479–1482.
- Alkhalifah, T., and Tsvankin, I., 1995, Velocity analysis for transversely isotropic media: *Geophysics*, **60**, 1550–1566.
- Bakulin, A., Grechka, V., and Tsvankin, I., 2000, Estimation of fracture parameters from reflection seismic data – Part II: Fractured models with orthorhombic symmetry: *Geophysics*, **65**, 1803–1817.
- Červený V., 2001, *Seismic ray theory*: Cambridge University Press.
- Gajewski, D., and Pšenčík, I., 1990, Vertical seismic profile synthetics by dynamic ray tracing in laterally varying layered anisotropic structure: *Journal of Geophysical Research*, **95**, 11301–11315.
- Goldin, S. 1986, *Seismic traveltime inversion*: Society of Exploration Geophysics.
- Grechka, V., Theophanis, S., and Tsvankin, I., 1999. Joint inversion of P- and PS- waves in orthorhombic media: Theory and a physical modeling study: *Geophysics*, **64**, 146–161.
- Grechka, V., and Tsvankin, I., 1998, Feasibility of nonhyperbolic moveout inversion in transversely isotropic media: *Geophysics*, **63**, 957–969.

- Grechka, V., and Tsvankin, I., 1999, 3-D moveout velocity analysis and parameter estimation for orthorhombic media: *Geophysics*, **64**, 820–837.
- Lynn, H.B., Campagna, D., Simon, K.M., and Beckham, W.E., 1999, Relationship of P-wave seismic attributes, azimuthal anisotropy, and commercial gas pay in 3-D P-wave multi-azimuth data, Rulison Field, Piceance Basin, Colorado: *Geophysics*, **64**, 1312–1328.
- Mallick, S., Craft, K., and Meister, L., 1998, Determination of the principal directions of azimuthal anisotropy from P-wave seismic data: *Geophysics*, **63**, 692–706.
- Martinez, R.D., 1993, Wave propagation effects on amplitude variation with offset measurements: A modeling study: *Geophysics*, **58**, 534–543.
- Maultzsch, S., Horne, S., Archer, S., and Burkhardt, H., 2003, Effects of an anisotropic overburden on azimuthal amplitude analysis in horizontal transverse isotropic media: *Geophysical Prospecting*, **51**, 61–74.
- Newman, P., 1973, Divergence effects in a layered earth: *Geophysics*, **38**, 481–488.
- Pech, A., and Tsvankin, I., 2004, Quartic moveout coefficient for a dipping azimuthally anisotropic layer: *Geophysics*, **69**, 699–707.
- Rüger, A., 2001, Reflection coefficients and azimuthal AVO analysis in anisotropic media: *Society of Exploration Geophysics*.
- Rüger, A., and Tsvankin, I., 1997, Using AVO for fracture detection: Analytic basis and practical solutions: *The Leading Edge*, **16**, 1429–1434.
- Schoenberg, M., and Helbig, K., 1997, Orthorhombic media: Modeling elastic wave behavior in a vertically fractured earth: *Geophysics*, **62**, 1954–1974.
- Thomsen, L., 1986, Weak elastic anisotropy: *Geophysics*, **51**, 1954–1966.
- Tsvankin, I., 1995, Body-wave radiation patterns and AVO in transversely isotropic media: *Geophysics*, **60**, 1409–1425.
- Tsvankin, I., 1997, Anisotropic parameters and P-wave velocity for orthorhombic media: *Geophysics*, **62**, 1292–1309.
- Tsvankin, I., 2001, *Seismic signatures and analysis of reflection data in anisotropic media*: Elsevier Science Publ. Co., Inc.
- Tsvankin, I., and Thomsen, L., 1994, Nonhyperbolic reflection moveout in anisotropic media: *Geophysics*, **59**, 1290–1304.
- Ursin, B., and Hokstad, K., 2003, Geometrical spreading in a layered transversely isotropic medium with vertical symmetry axis: *Geophysics*, **68**, 2082–2091.
- Vanelle, C., and Gajewski, D., 2003, Determination of geometrical spreading from travel-times: *Journal of Applied Geophysics*, **54**, 391–400.

Chapter 3

Anisotropic geometrical-spreading correction for wide-azimuth P-wave reflections

3.1 Summary

Compensation for the geometrical spreading along the raypath is one of the key steps in AVO (amplitude variation with offset) analysis, in particular for wide-azimuth surveys. Here, we propose an efficient methodology to correct long-spread, wide-azimuth reflection data for the geometrical spreading in stratified azimuthally anisotropic media. The P-wave geometrical-spreading factor is expressed through the reflection traveltime described by a nonhyperbolic moveout equation that has the same form as in VTI (transversely isotropic with a vertical symmetry axis) media.

The adapted VTI equation is parameterized by the normal-moveout (NMO) ellipse and the azimuthally varying anellipticity parameter $\eta(\alpha)$. To estimate the moveout parameters, we apply the 3D nonhyperbolic semblance algorithm of Vasconcelos and Tsvankin that operates simultaneously with traces at all offsets and azimuths. The estimated moveout parameters are used as the input in the geometrical-spreading computation. Numerical tests for models composed of orthorhombic layers with strong, depth-varying velocity anisotropy confirm the high accuracy of our traveltime-fitting procedure and, therefore, of the geometrical-spreading correction. Since our algorithm is based entirely on the kinematics of reflection arrivals, it can be readily incorporated into the processing flow of azimuthal AVO analysis.

In combination with the nonhyperbolic moveout inversion, the method was applied to wide-azimuth P-wave data collected at Weyburn field in Canada. The geometrical-spreading factor for the reflection from the top of the fractured reservoir is clearly influenced by the azimuthal anisotropy in the overburden, which should cause distortions in the estimated azimuthal AVO attributes. This case study confirms that the azimuthal variation of the geometrical-spreading factor is often comparable to or exceeds that of the reflection coefficient.

3.2 Introduction

Seismic signatures measured in wide-azimuth reflection surveys may be strongly influenced by azimuthal anisotropy associated with natural fracture systems, nonhydrostatic stresses, or dipping transversely isotropic layers (e.g., shales). The inversion of azimuthally

varying traveltimes and amplitudes of reflected waves gives valuable information for characterization of fractured reservoirs and lithology discrimination (Mallick et al., 1998; Grechka and Tsvankin, 1999a; Lynn et al., 1999; Bakulin et al., 2000; Rüger, 2001; Hall and Kendall, 2003). Although the most direct evidence of the presence of azimuthal anisotropy is provided by shear-wave splitting, estimation of a representative set of anisotropic parameters is impossible without performing azimuthal moveout or amplitude-variation-with-offset (AVO) analysis.

The main advantages of the anisotropic AVO inversion are the possibility of resolving the reflection coefficient at the target horizon and the high sensitivity of body-wave reflectivity to the anisotropic parameters (e.g., Tsvankin, 1995, 2005; Rüger, 2001). However, the transformation of seismic amplitudes measured at the surface into the reflection coefficients involves corrections for the source signature and propagation phenomena along the raypath (e.g., Maultzsch et al., 2003). Major amplitude distortions in anisotropic media, in particular for wide-azimuth data, are caused by the directionally varying geometrical spreading above the reflector. A detailed discussion of geometrical spreading in TI and orthorhombic media can be found in Ursin and Hokstad (2003), Tsvankin (2005, Chapter 2) and Xu et al. (2005; hereafter referred to as Paper I).

If the velocity model of the overburden is known, geometrical spreading can be computed, for example, by performing dynamic ray tracing. A more practical approach that does not depend on knowledge about the velocity model is based on expressing geometrical spreading through reflection traveltimes using ray theory (e.g., see equation 4.10.50 in Červený, 2001). As shown in Paper I, the geometrical-spreading factor L for laterally homogeneous media can be found as the following function of observed traveltime T :

$$L(x, \alpha) = \frac{\sqrt{\cos \phi^s \cos \phi^r}}{V_g} \left[\frac{\partial^2 T}{\partial x^2} \frac{\partial T}{\partial x} \frac{1}{x} + \frac{\partial^2 T}{\partial x^2} \frac{\partial^2 T}{\partial \alpha^2} \frac{1}{x^2} - \left(\frac{\partial T}{\partial \alpha} \right)^2 \frac{1}{x^4} \right]^{-1/2}, \quad (3.1)$$

where x is the source-receiver offset, α is the azimuth of the source-receiver line with respect to the x_1 -axis, V_g is the group velocity at the source location, and ϕ^s and ϕ^r are the angles between the ray and the vertical at the source and receiver, respectively.

In Paper I, equation 3.1 is combined with the Tsvankin-Thomsen (1994) nonhyperbolic moveout equation for the traveltime T to study the P-wave geometrical spreading in a horizontal orthorhombic layer. Analytic results and numerical modeling reveal pronounced distortions of the geometrical spreading caused by both polar and azimuthal anisotropy. Paper I demonstrates that reliable recovery of the reflection coefficient from the azimuthal AVO response often requires an accurate anisotropic geometrical-spreading correction (also, see Mallick et al., 1998).

The goal of this paper is to develop a practical implementation of the geometrical-spreading correction for layered azimuthally anisotropic media. The main emphasis of the paper is on models with orthorhombic symmetry considered typical for naturally fractured reservoirs (e.g., Schoenberg and Helbig, 1997; Bakulin et al., 2000). It is clear from equation 3.1 that the key issue in computing the geometrical-spreading factor from surface data is to find a smooth approximation for reflection traveltime that can be used for a wide range

of offsets and azimuths.

We start by testing the accuracy of a simplified P-wave moveout equation based on the approximate kinematic equivalence between orthorhombic and VTI media. While this equation provides a good fit to the traveltimes for layered models with a uniform (identical) orientation of the vertical symmetry planes in all layers, it requires modification when the symmetry-plane azimuths vary with depth. We use the 3D semblance algorithm of Vasconcelos and Tsvankin (2004) to estimate the best-fit moveout parameters needed to evaluate the traveltime derivatives in equation 3.1. Numerical tests for layered orthorhombic models confirm that azimuthal anisotropy may produce comparable distortions in the geometrical spreading and in the reflection coefficient. Finally, we apply the algorithm to wide-azimuth data collected at Weyburn field in Canada to evaluate the azimuthally varying geometrical-spreading factor for wide-angle reflections from the reservoir.

3.3 Moveout equations for orthorhombic media

Homogeneous layer

The analysis in Paper I confirms the conclusion of Al-Dajani et al. (1998) that P-wave reflection traveltime in a horizontal orthorhombic layer with a horizontal symmetry plane is well-described by the Tsvankin-Thomsen (1994) nonhyperbolic moveout equation. The form of this equation remains the same for different anisotropic symmetries, but in the presence of azimuthal anisotropy the moveout coefficients become azimuthally dependent:

$$T^2(x, \alpha) = T_0^2 + \frac{x^2}{V_{\text{nmo}}^2(\alpha)} + \frac{A_4(\alpha)x^4}{1 + A(\alpha)x^2}. \quad (3.2)$$

Here, V_{nmo} is the normal-moveout (NMO) velocity, A_4 is the quartic moveout coefficient, and A is the coefficient that ensures the convergence of equation 3.2 for large source-receiver offsets.

The azimuthally varying NMO velocity traces out an ellipse with the axes parallel to the vertical symmetry planes of the orthorhombic layer (Grechka and Tsvankin, 1998):

$$V_{\text{nmo}}^{-2}(\alpha) = \frac{\sin^2(\alpha - \phi)}{\left(V_{\text{nmo}}^{(1)}\right)^2} + \frac{\cos^2(\alpha - \phi)}{\left(V_{\text{nmo}}^{(2)}\right)^2}, \quad (3.3)$$

where $V_{\text{nmo}}^{(1)}$ and $V_{\text{nmo}}^{(2)}$ are the semi-minor and semi-major axes of the NMO ellipse, respectively, and ϕ is the azimuth of the semi-major axis.

Explicit expressions for the coefficients $A_4(\alpha)$ and $A(\alpha)$ are given in Al-Dajani et al. (1998) and Paper I. However, the nonhyperbolic (x^4) term in equation 3.2 can be substantially simplified by using an approximate equivalence between the P-wave kinematics in the vertical symmetry planes of orthorhombic and VTI media. The VTI moveout equation of Alkhalifah and Tsvankin (1995) can be adapted for an orthorhombic layer by introducing

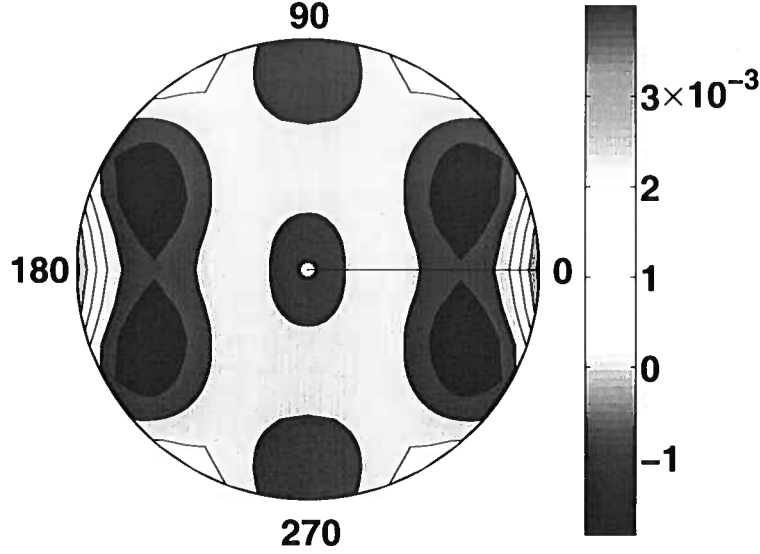


Figure 3.1. Accuracy of equation 3.4 in describing full-azimuth, long-offset P-wave moveout in a homogeneous orthorhombic layer. The moveout parameters are found by fitting equation 3.4 to traveltimes computed by anisotropic ray tracing. The map shows the difference between the best-fit and ray-traced traveltimes normalized by the zero-offset time (0.82 s). The radius corresponds to the source-receiver offset (the maximum offset-to-depth ratio is three), the numbers around the perimeter indicate the azimuth with respect to the $[x_1, x_3]$ symmetry plane. The P-wave velocity parameters of the model are $V_{P0} = 2.437$ km/s, $\epsilon^{(1)} = 0.329$, $\epsilon^{(2)} = 0.258$, $\delta^{(1)} = 0.083$, $\delta^{(2)} = -0.078$, and $\delta^{(3)} = -0.106$. The corresponding moveout parameters are $V_{\text{nmo}}^{(1)} = 2.632$ km/s, $V_{\text{nmo}}^{(2)} = 2.239$ km/s, $\eta^{(1)} = 0.211$, $\eta^{(2)} = 0.398$, and $\eta^{(3)} = 0.194$.

an azimuthally varying anellipticity coefficient $\eta(\alpha)$ (Pech and Tsvankin, 2004; Paper I):

$$T^2(x, \alpha) = T_0^2 + \frac{x^2}{V_{\text{nmo}}^2(\alpha)} - \frac{2\eta(\alpha)x^4}{V_{\text{nmo}}^2(\alpha)[T_0^2 V_{\text{nmo}}^2(\alpha) + (1 + 2\eta(\alpha))x^2]}, \quad (3.4)$$

$$\eta(\alpha) = \eta^{(1)} \sin^2(\alpha - \phi) + \eta^{(2)} \cos^2(\alpha - \phi) - \eta^{(3)} \sin^2(\alpha - \phi) \cos^2(\alpha - \phi). \quad (3.5)$$

The anellipticity parameters $\eta^{(1)}$, $\eta^{(2)}$, and $\eta^{(3)}$ are defined in the symmetry planes by analogy with the Alkhalifah-Tsvankin parameter η for VTI media (Grechka and Tsvankin, 1999b).

Although the analogy between orthorhombic and VTI media is based on the weak-

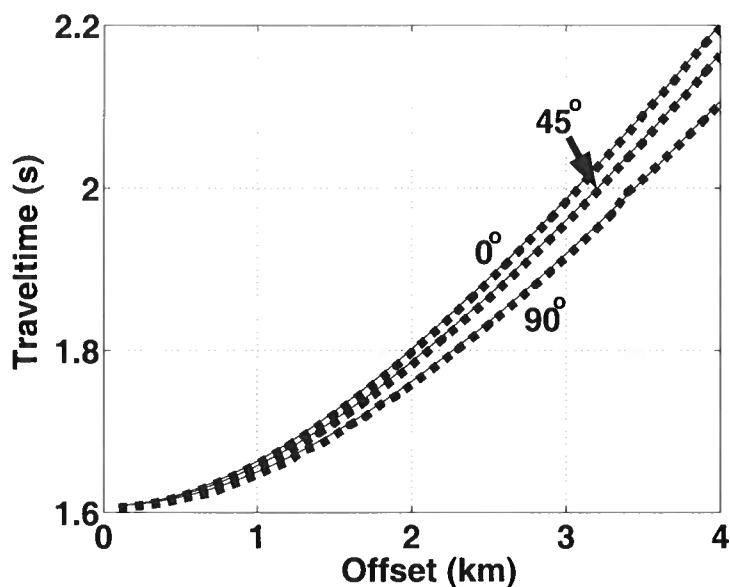


Figure 3.2. Accuracy of equation 3.4 for the layered azimuthally anisotropic model from Table 1 (model 1). The azimuths ($\alpha = 0^\circ$, 45° , and 90°) with respect to the $[x_1, x_3]$ symmetry plane are marked on the plot. The dashed line is the ray-traced traveltime for the reflection from the bottom of layer 3, the solid line is the corresponding traveltime computed from equation 3.4 with the following estimated (best-fit) moveout parameters: $\phi = 90^\circ$, $V_{\text{nmo}}^{(1)} = 2.307$ km/s, $V_{\text{nmo}}^{(2)} = 2.675$ km/s, $\eta^{(1)} = 0.305$, $\eta^{(2)} = 0.222$, and $\eta^{(3)} = -0.006$.

anisotropy approximation, extensive numerical testing shows that equation 3.4 with fitted moveout parameters provides excellent accuracy for a homogeneous orthorhombic layer with a horizontal symmetry plane (see also Vasconcelos and Tsvankin, 2004). In Figure 3.1, the parameters $V_{\text{nmo}}^{(1)}$, $V_{\text{nmo}}^{(2)}$, $\eta^{(1)}$, $\eta^{(2)}$, $\eta^{(3)}$, and ϕ were found by fitting equation 3.4 to ray-traced traveltimes using the least-squares method. Here and in the examples below, the synthetic data are generated using ANRAY – the 3D anisotropic ray-tracing code of Gajewski and Pšenčík (1990). The difference between the ray-traced traveltimes and those computed from equation 3.4 is much less than 1% of the zero-offset two-way traveltime (i.e., less than 4 ms) for a wide range of offsets and azimuths. Note that the model in Figure 3.1 has substantial polar and azimuthal anisotropy, and the maximum offset-to-depth ratio is as large as three. The influence of traveltime errors on the computation of the moveout parameters and geometrical spreading is analyzed in detail below.

3.3.1 Layered models with uniform symmetry-plane orientation

Next, we apply equation 3.4 to more complicated, multilayered azimuthally anisotropic models. Suppose the medium above the reflector includes horizontal layers of orthorhombic or higher symmetries, and the vertical symmetry planes in each layer have the same orientation. Note that in azimuthally isotropic (i.e., VTI or purely isotropic) media any vertical plane is a plane of mirror symmetry. The uniform orientation of the symmetry planes in all layers implies that the model as a whole has two orthogonal vertical symmetry planes.

Because of the kinematic equivalence between the symmetry planes of orthorhombic and VTI media, P-wave nonhyperbolic moveout in the symmetry-plane directions is well-described by equation 3.4 with the effective parameter η computed from the VTI averaging equations (Tsvankin, 1997; 2005, Appendix 4B). Although for off-symmetry azimuthal directions the kinematic analogy with VTI media is valid only for weak anisotropy, the numerical testing in the last section indicates that equation 3.4 parameterized by the best-fit values of V_{nmo} and η may be sufficiently accurate for any given azimuth. It is not clear, however, whether or not the azimuthal variation of the effective parameter $\eta(\alpha)$ can be described by the single-layer equation 7.10.

To estimate the effective moveout parameters in equation 3.4 without traveltimes picking, we employ the 3D nonhyperbolic semblance algorithm of Vasconcelos and Tsvankin (2004). They developed a three-step procedure designed to make the multiparameter semblance search for wide-azimuth surveys more efficient. First, conventional-spread data are used to reconstruct the NMO ellipse and estimate the symmetry-plane azimuth ϕ and the NMO velocities $V_{\text{nmo}}^{(1)}$ and $V_{\text{nmo}}^{(2)}$. Second, the anellipticity parameters $\eta^{(1)}$ and $\eta^{(2)}$, which are defined in the vertical symmetry planes, are found from the VTI nonhyperbolic semblance analysis in narrow sectors centered at the symmetry-plane directions. The third step is a full-azimuth nonhyperbolic semblance search based on equations 7.9–7.10, with the estimated values of the parameters ϕ , $V_{\text{nmo}}^{(1)}$, $V_{\text{nmo}}^{(2)}$, $\eta^{(1)}$, and $\eta^{(2)}$ used to specify the starting model.

Application of this semblance algorithm to ray-traced seismograms computed for the four-layer model with the parameters listed in Table 1 confirms that equation 3.4 accurately describes long-spread moveout for the full range of azimuths (Figure 3.2). The model includes two orthorhombic layers with a substantial magnitude of polar and azimuthal anisotropy sandwiched between two isotropic layers. The error of equation 3.4 does not exceed 0.3% of the zero-offset traveltime for all offsets and azimuths; similar results were obtained for a wide range of plausible orthorhombic models.

The high accuracy of the traveltimes fitting method, however, does not imply that the estimated effective NMO velocity and, especially, the coefficient η are always close to the analytic values because of the tradeoffs between various moveout parameters (Vasconcelos and Tsvankin, 2004). Nevertheless, as long as equation 3.4 accurately matches the exact traveltime, the best-fit moveout parameters provide suitable input for the geometrical-spreading correction.

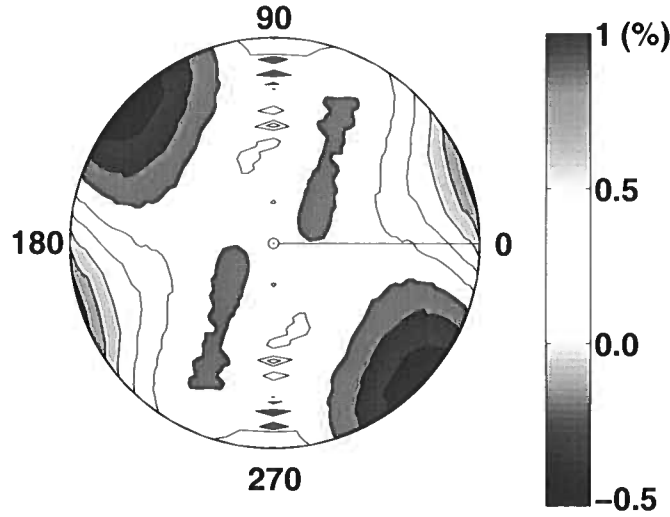


Figure 3.3. Map of the traveltime residuals (normalized by the zero-offset time $T_0 = 1.334$ s) plotted as a function of offset and azimuth for the two-layer model with misaligned symmetry planes from Table 2 (model 2). The residuals are computed for the reflection from the bottom of the model as the differences between the best-fit traveltimes from equation 3.4 and ray tracing. The maximum offset is 4 km; the corresponding offset-to-depth ratio is two. The estimated moveout parameters are $\phi = 78^\circ$, $V_{\text{nmo}}^{(1)} = 2.60$ km/s, $V_{\text{nmo}}^{(2)} = 3.00$ km/s, $\eta^{(1)} = 0.567$, $\eta^{(2)} = 0.330$, and $\eta^{(3)} = 0.104$.

3.3.2 Models with misaligned symmetry planes

For media without throughgoing vertical symmetry planes, the azimuthal variation of the quartic moveout coefficient A_4 becomes more complicated (Al-Dajani et al., 1998), and equation 7.10 for the parameter η may no longer be accurate. However, extensive testing that we performed for a range of orthorhombic models with misaligned symmetry planes shows that traveltime errors seldom exceed 0.5% of the zero-offset time. Apparently, the magnitude of the additional terms in the azimuthal dependence of η is relatively small, and the moveout-inversion algorithm compensates for these missing terms by adjusting the best-fit parameters $\eta^{(1)}$, $\eta^{(2)}$, and $\eta^{(3)}$.

Model 2 used in Figure 3.3 contains two orthorhombic layers with uncommonly large values of the anisotropy parameters and the vertical symmetry planes misaligned by 45° (Table 2). For this extreme example, the normalized errors of equation 3.4 reach 1%. While traveltime errors on the order of 0.5–1% may be acceptable for purposes of conventional moveout inversion, they propagate with amplification into the geometrical-spreading factor (equation 1).

To improve time fitting for multilayered anisotropic media with misaligned symmetry

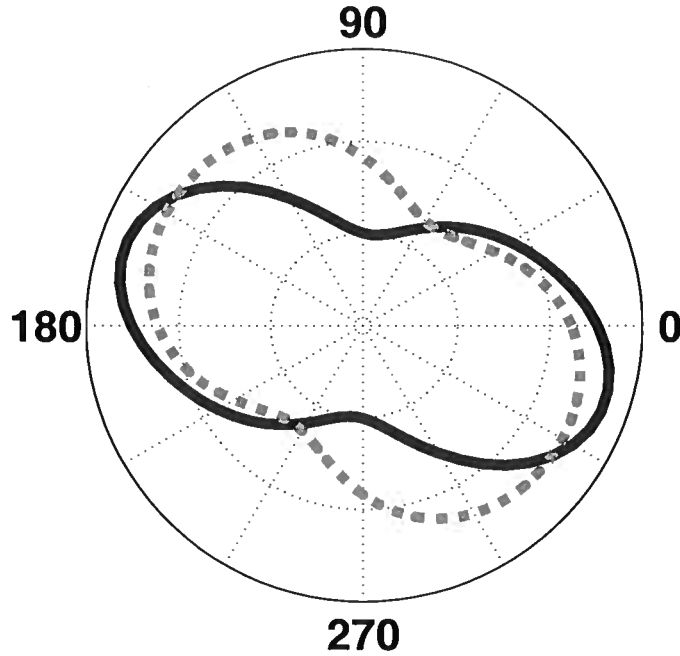


Figure 3.4. Comparison of the effective parameter $\eta(\alpha)$ computed from the VTI averaging equation 3.6 (solid curve) and estimated by the moveout-inversion algorithm (dashed). The model is composed of two orthorhombic layers; for the top layer, $\phi = 15^\circ$, $V_{\text{nmo}}^{(1)} = 2.236$ km/s, $V_{\text{nmo}}^{(2)} = 2.850$ km/s, $\eta^{(1)} = 0.375$, $\eta^{(2)} = 0.000$, and $\eta^{(3)} = -0.086$; for the bottom layer, $\phi = 0^\circ$, $V_{\text{nmo}}^{(1)} = 3.421$ km/s, $V_{\text{nmo}}^{(2)} = 2.683$ km/s, $\eta^{(1)} = 0.000$, $\eta^{(2)} = 0.375$, and $\eta^{(3)} = 0.163$. The maximum offset-to-depth ratio of the data used in the inversion is two.

planes, equation 7.10 can be modified in a relatively straightforward way. To introduce this modification, we analyze the effective parameter $\eta(\alpha)$ for a stack of horizontal orthorhombic layers by applying the VTI averaging equation (Tsvankin, 2005, equation 4.47) for each azimuth α :

$$\eta(\alpha) = \frac{1}{8} \left\{ \frac{1}{V_{\text{nmo}}^4(\alpha) T_0} \left[\sum_{i=1}^N (V_{\text{nmo}}^{(i)}(\alpha))^4 (1 + 8\eta^{(i)}(\alpha)) T_0^{(i)} \right] - 1 \right\}, \quad (3.6)$$

where $V_{\text{nmo}}^{(i)}(\alpha)$ and $\eta^{(i)}(\alpha)$ are the interval parameters in layer i . Although equation 3.6 may become inaccurate for models with strong azimuthal anisotropy, it usually reproduces the shape of the azimuthal variation of the effective η (Al-Dajani et al., 1998).

Figure 3.4 shows a comparison between the parameter η computed from equation 3.6 (solid curve) and estimated by the moveout-inversion algorithm (dashed) for a two-layer

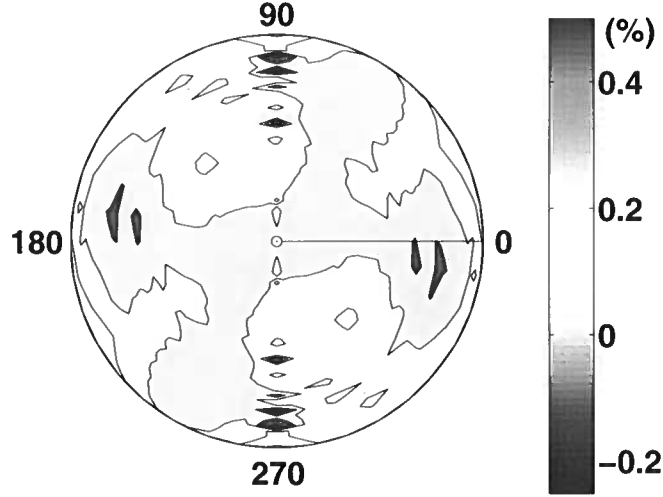


Figure 3.5. Same as Figure 3.3, but the moveout parameters of equation 3.4 were estimated by the modified inversion algorithm that allows for an independent orientation of the $\eta(\alpha)$ -curve [equation 3.7]. The best-fit parameters are $\phi = 81^\circ$, $V_{\text{nmo}}^{(1)} = 2.586$ km/s, $V_{\text{nmo}}^{(2)} = 3.00$ km/s, $\eta^{(1)} = 0.594$, $\eta^{(2)} = 0.339$, $\eta^{(3)} = 0.161$, and $\phi_1 = 89^\circ$.

orthorhombic model with the symmetry planes misaligned by 15° . The shape of the two curves is quite similar, which explains the relatively low magnitude of the time residuals typically produced by equation 3.4. The misalignment of the symmetry planes, however, causes a rotation of the estimated η -curve with respect to the one calculated from equation 3.6.

The moveout-inversion algorithm cannot accommodate this rotation because the “principal axes” of the azimuthal variation of $\eta(\alpha)$ in equation 7.10 are parallel to the axes of the NMO ellipse (equation 7.9). Therefore, the traveltime fitting at far offsets can be improved by decoupling the nonhyperbolic moveout term from the NMO ellipse and introducing an additional angle ϕ_1 responsible for the azimuthal variation of the effective parameter η :

$$\eta(\alpha) = \eta^{(1)} \sin^2(\alpha - \phi_1) + \eta^{(2)} \cos^2(\alpha - \phi_1) - \eta^{(3)} \sin^2(\alpha - \phi_1) \cos^2(\alpha - \phi_1). \quad (3.7)$$

The first two steps of the modified moveout-inversion algorithm remain the same as those described above, but at the last step we fix the orientation of the NMO ellipse (angle ϕ) and search for the angle ϕ_1 and the other moveout parameters using the full range of offsets and azimuths. Application of this algorithm to model 2 (Table 2) results in a substantially improved time fitting (compare Figure 3.5 with Figure 3.3) and a 15% increase in the total semblance value. Hence, equation 3.7 should help make our moveout approximation suitable even for models with uncommonly strong, depth-varying azimuthal anisotropy.

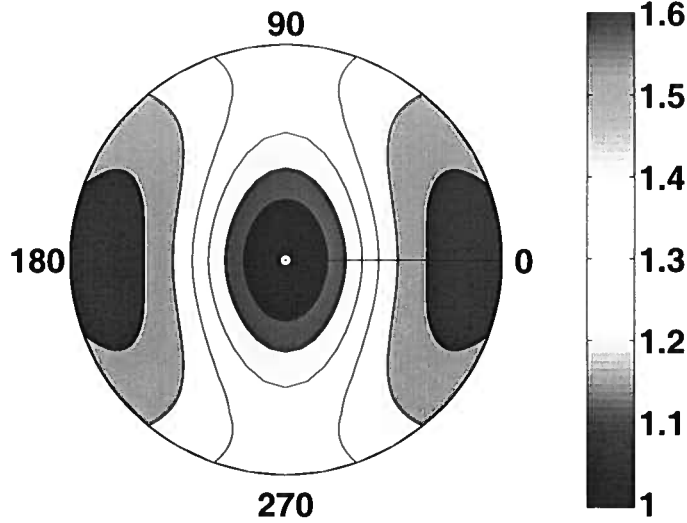


Figure 3.6. Map of the geometrical spreading for the reflection from the bottom of layer 3 in model 1 (Table 1). The factor L is normalized by its value in the reference isotropic homogeneous medium with the velocity equal to $V_{\text{nmo}} = (V_{\text{nmo}}^{(1)} + V_{\text{nmo}}^{(2)})/2$. The maximum offset-to-depth ratio is two.

3.4 Azimuth-dependent geometrical-spreading correction

The traveltime derivatives in the geometrical-spreading equation 3.1 can be computed from the best-fit moveout parameters in equation 3.4. Explicit expressions for these derivatives are given in Appendix A.

Equation 3.1 also contains the group angles at the source (ϕ^s) and receiver (ϕ^r) locations. Since our model is laterally homogeneous, the ray parameter (horizontal slowness) p_{hor} does not change along the raypath and can be computed as

$$p_{\text{hor}} = \sqrt{\left(\frac{\partial T}{\partial x}\right)^2 + \left(\frac{1}{x} \frac{\partial T}{\partial \alpha}\right)^2}. \quad (3.8)$$

In most cases of practical importance, the subsurface layer is isotropic and has a known P-wave velocity V . Then the group angles at the source and receiver can be found directly from p_{hor} :

$$\cos \phi^s = \cos \phi^r = \sqrt{1 - p_{\text{hor}}^2 V^2}. \quad (3.9)$$

If the subsurface layer is anisotropic, estimation of the group angles from the traveltime derivatives involves the relevant anisotropy parameters.

Combining equation 3.1 with the expressions in Appendix A and taking equation 3.9

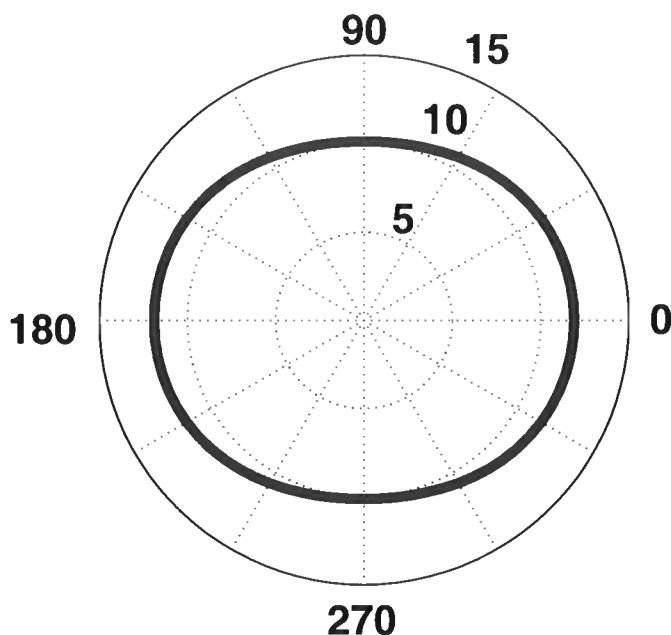


Figure 3.7. Azimuthally varying geometrical spreading for model 1 (Figure 3.6) computed for an offset of 2 km. The corresponding phase incidence angle at the reflector (the bottom of layer 3) is close to 30° ($30^\circ \pm 5^\circ$).

into account, one can compute the geometrical spreading from the best-fit moveout parameters.

3.4.1 Synthetic example

Using the method described above, we calculated the geometrical-spreading factor $L(x, \alpha)$ for the reflection from the bottom of layer 3 in model 1 (Table 1). As was the case for the homogeneous orthorhombic medium discussed in Paper I, the influence of anisotropy leads to pronounced, azimuthally-dependent distortions of the geometrical spreading (Figure 3.6). For an offset-to-depth-ratio of unity, the factor L decreases by 17% between the azimuths $\alpha = 0^\circ$ and 90° (Figure 3.7). Since all layers are horizontal, the dependence of the geometrical spreading on azimuth is caused entirely by the azimuthal anisotropy above the reflector. For comparison, the azimuthal variation of the reflection coefficient for the same event is less than 13% (Figure 3.8). Clearly, if the anisotropic geometrical spreading is unaccounted for, it can compromise the azimuthal AVO signature for this model.

The high accuracy of our algorithm is verified by comparing its output with the results of dynamic ray tracing (Figure 3.9). The geometrical-spreading factors computed by the two methods are almost identical for offset-to-depth ratios less than 1.5, and only slightly

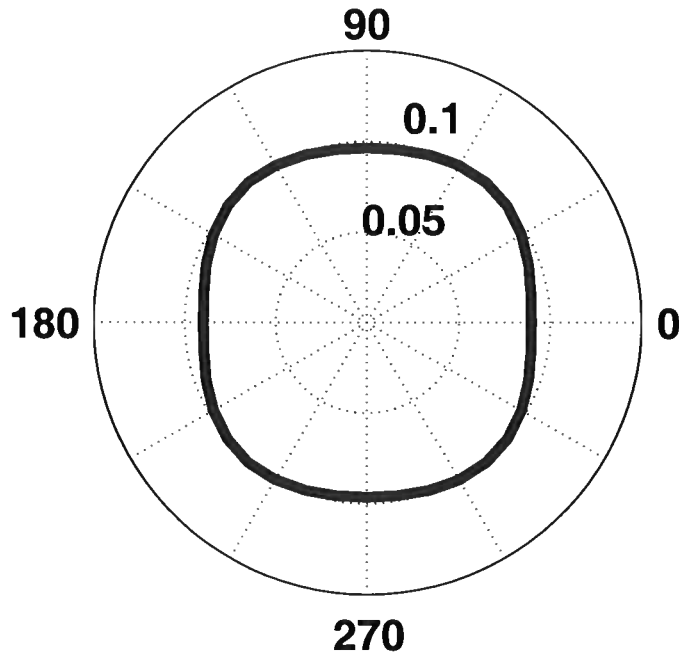


Figure 3.8. Azimuthally varying reflection coefficient from the bottom of layer 3 in model 1 (Table 1) computed for the phase incidence angle at the reflector equal to 30° .

	Symmetry type	V_{P0} (km/s)	Thickness (km)	$V_{nmo}^{(1)}$	$V_{nmo}^{(2)}$	$\eta^{(1)}$	$\eta^{(2)}$	$\eta^{(3)}$
Layer 1	ISO	1.5	0.2	1.5	1.5	0	0	0
Layer 2	ORTH	2.437	0.9	2.632	2.239	0.211	0.398	0.194
Layer 3	ORTH	3.0	0.9	3.146	2.683	0.182	0.313	-0.056
Layer 4	ISO	3.2	0.5	3.2	3.2	0	0	0

Table 3.1. Parameters of a four-layer model (model 1) that includes two orthorhombic layers with aligned vertical symmetry planes $\phi = 0^\circ$ and $\phi = 90^\circ$. The density used in the computation of the reflection coefficient in Figure 3.8 is set to 1.0 g/cm^3 in all layers.

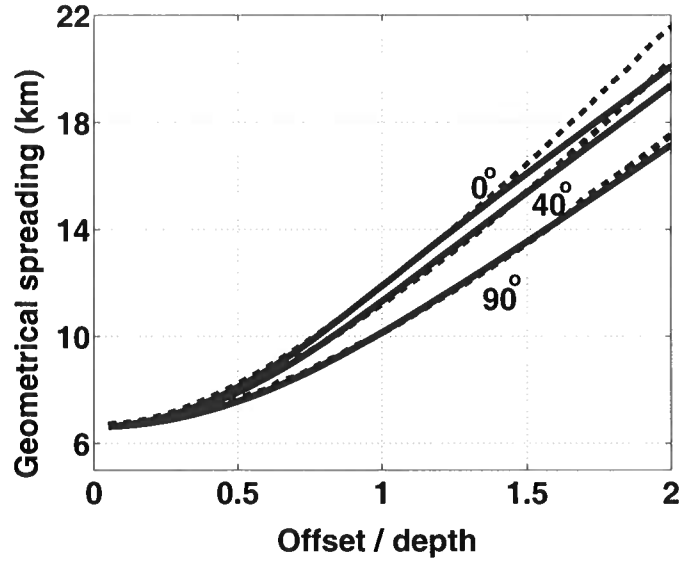


Figure 3.9. Accuracy of our method for the reflection from the bottom of layer 3 in model 1; the azimuths from the $[x_1, x_3]$ symmetry plane are $\alpha = 0^\circ, 40^\circ,$ and 90° . The geometrical-spreading factor L computed by our algorithm (solid lines) is compared with the output of dynamic ray-tracing code ANRAY (dashed).

	Symmetry type	V_{P0} (km/s)	Thickness (km)	$V_{\text{nmo}}^{(1)}$	$V_{\text{nmo}}^{(2)}$	$\eta^{(1)}$	$\eta^{(2)}$	$\eta^{(3)}$
Layer 1	ORTH	3.0	1.0	2.509	2.683	0.857	0.875	-0.192
Layer 2	ORTH	3.0	1.0	3.421	2.509	0.038	1.071	0.030

Table 3.2. Parameters of a model (model 2) that includes two orthorhombic layers with misaligned symmetry planes and uncommonly strong anisotropy. The azimuth of the $[x_1, x_3]$ symmetry plane is $\phi = 45^\circ$ in layer 1 and $\phi = 0^\circ$ in layer 2.

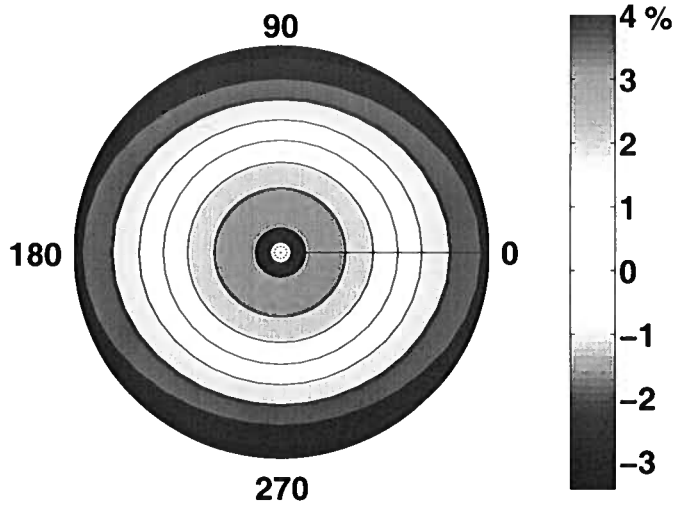


Figure 3.10. Percentage error of the geometrical spreading for model 1 (Figure 3.6) caused by the traveltime error function $4 \sin(3\pi x/x_{\max}) \sin 4\alpha$ (in ms). The maximum offset-to-depth ratio is two.

diverge at longer offsets. The deviation of our result from that of the ray tracing, which reaches a maximum of 6% for $\alpha = 0^\circ$, can be explained by the approximate nature of equation 3.4 and, possibly, by numerical errors in both algorithms. Overall, our method produces a sufficiently accurate geometrical-spreading factor in layered orthorhombic media for a wide range of offsets and azimuths.

3.4.2 Error analysis

To study the influence of realistic traveltime noise on the geometrical spreading computed by our method, we added linear and sinusoidal time errors to the reflection traveltimes for model 1 (Table 1 and Figure 3.2). Linear traveltime noise can approximate long-period static errors, whereas sinusoidal errors can be due to short-period statics.

The linear time error changes from 4 ms at zero offset to -4 ms at the maximum offset (equal to two reflector depths) for each azimuth α . Application of our algorithm to the perturbed traveltimes in the full range of azimuths yields slightly distorted values of the velocities $V_{\text{nm}o}^{(1,2)}$ (the errors are about 1%) and parameters $\eta^{(1,2,3)}$ (the errors are less than 0.03); the maximum error in the geometrical spreading does not exceed 2%. When the magnitude of the linear error function increases from 4 ms to 8 ms, the corresponding geometrical-spreading error reaches only 5%. It is noteworthy that the moveout parameters estimated from wide-azimuth data are less sensitive to linear traveltime errors than those obtained from 2D semblance analysis for VTI media (Tsvankin, 2005). On the whole, our geometrical-spreading computation is sufficiently robust in the presence of moderate linear

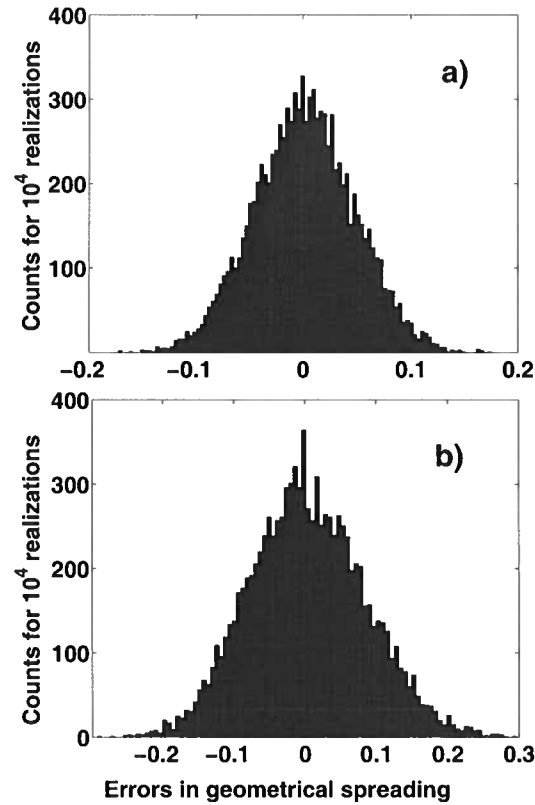


Figure 3.11. Histogram of the error distribution in the geometrical spreading computed in the $[x_1, x_3]$ symmetry plane of model 1 (Figure 3.6). The moveout parameters were contaminated by Gaussian noise with the following standard deviations: 0.5% for T_0 , 3% for $V_{\text{mmo}}^{(1)}$ and $V_{\text{mmo}}^{(2)}$, 30% for $\eta^{(1)}$ and $\eta^{(2)}$, and 50% for $\eta^{(3)}$. The offset-to-depth ratio is equal to one (a) and two (b). The standard deviation of the error in L is 5% in plot (a) and 8% in plot (b).

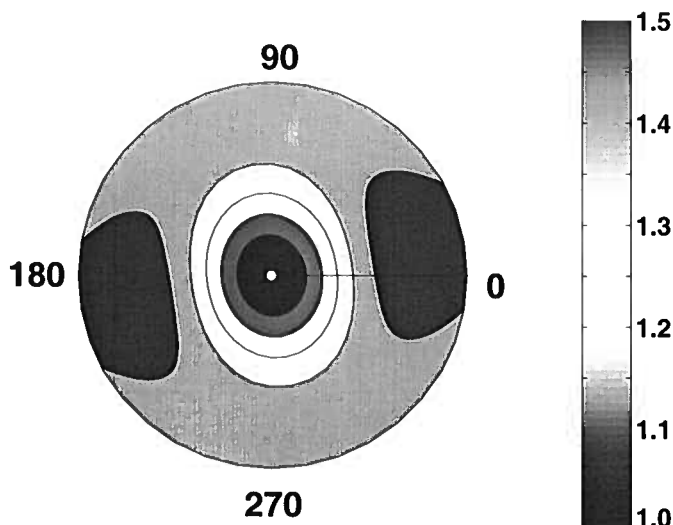


Figure 3.12. Map of the geometrical spreading for the P-wave reflection from the Mississippian formation (the top of the reservoir) at Weyburn field computed for CMP 10829. The factor L is normalized by its value in the reference isotropic homogeneous medium with the velocity equal to $(V_{\text{nmto}}^{(1)} + V_{\text{nmto}}^{(2)})/2$. The moveout parameters are taken from Vasconcelos and Tsvankin (2004): $\phi = 99^\circ$, $V_{\text{nmto}}^{(1)} = 2.371$ km/s, $V_{\text{nmto}}^{(2)} = 2.464$ km/s, $\eta^{(1)} = 0.255$, $\eta^{(2)} = 0.186$, and $\eta^{(3)} = -0.062$. The reflector depth is 1.4 km (the maximum offset-to-depth ratio is 2.5). The North-South direction is at $\phi = 0^\circ$, and the East-West at $\phi = 90^\circ$.

noise.

To test the influence of short-period static errors, the traveltimes for model 1 were contaminated by several sinusoidal functions of the form $A \sin(n\pi x/x_{\text{max}}) \sin m\alpha$. The maximum time error A was fixed at 4 ms; the coefficients n and m control the period of the error function in the radial and azimuthal directions, respectively. When $m = 0$ (i.e., no azimuthal variation in the error) and n is an even number, the spreading remains almost unchanged. Apparently, an equal number of peaks and troughs over the spreadlength compensate for one another, and the noise does not noticeably distort the best-fit moveout parameters and, consequently, the geometrical spreading. However, when n is an odd number (i.e., the number of peaks and troughs differs by one), the sinusoidal error does influence the output of our algorithm. The most significant distortion in geometrical spreading occurs for $n = 3$, when the maximum spreading error reaches 4% (for $m = 0$) over the whole range of offsets and azimuths; the error decreases with n .

Next, we make the traveltime error azimuthally dependent by varying m . Our tests show that the spreading errors are higher when m is an even number because in this case the azimuthal variation of the error function is similar to that of the traveltime $T(x, \alpha)$, which is governed by $\sin^2 \alpha$ and $\cos^2 \alpha$ [see equations 7.9–7.10]. Figure 3.10 displays the

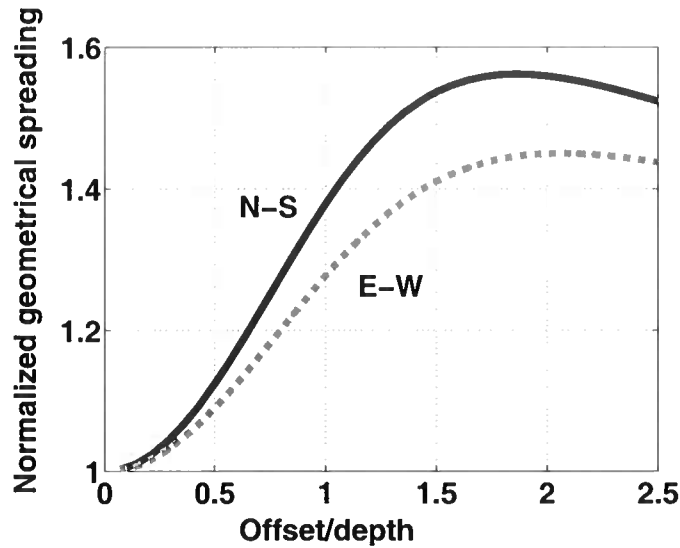


Figure 3.13. Normalized geometrical spreading from Figure 3.12 in the east-west and north-south directions.

distortion in the geometrical spreading caused by the error function $4 \sin(3\pi x/x_{\max}) \sin 4\alpha$ (i.e., $n = 3$ and $m = 4$). The maximum error of just 4% is the same as the one that was obtained for the azimuthally invariant error function with $n = 3$. When the magnitude of the error function increases from 4 ms to 8 ms, the corresponding geometrical-spreading error only doubles for fixed values of m and n .

Since it is difficult to study the influence of all plausible traveltime distortions (obviously, not limited to statics errors) on the geometrical spreading, next we examine the sensitivity of the factor L to errors in the input moveout parameters (see Appendix A). The geometrical-spreading error in a symmetry plane of model 1 caused by Gaussian noise added to the moveout parameters is shown in Figure 3.11. The level of this noise is slightly higher than the largest distortions caused by the traveltime errors studied above.

As the offset-to-depth ratio increases from one to two, the standard deviation of the error in L grows from 5% to 8%. Still, given the relatively high level of errors in the input parameters, the distortion of the spreading factor remains acceptable within the practically important offset range of up to twice the reflector depth. In particular, the geometrical-spreading error is smaller than the percentage error in each moveout parameter when the other parameters are held constant, which indicates that our operator is sufficiently stable. For example, a 5% error in $V_{\text{nm0}}^{(1)}$ yields an error in L of less than 3% if the offset-to-depth ratio does not exceed two.

3.4.3 Field-data application

To demonstrate the influence of azimuthal anisotropy on the geometrical spreading for field data, we applied the algorithm to wide-azimuth reflection events acquired above a fractured reservoir at Weyburn field in Canada by the Reservoir Characterization Project (a research consortium at CSM). Vasconcelos and Tsvankin (2004) carried out nonhyperbolic moveout inversion for P-wave reflections from several interfaces in the overburden and obtained relatively large values of the parameters $\eta^{(1,2,3)}$ reaching 0.25. They also concluded that at least the shallow part of the overburden exhibits non-negligible azimuthal anisotropy.

These results are in good agreement with the analysis of shear-wave splitting by Cardona (2002) and of the azimuthal AVO response by Jenner (2001). In particular, Jenner (2001) found that the P-wave AVO attributes at the reservoir level vary with azimuth. His amplitude processing, however, included only the conventional geometrical-spreading correction for isotropic media.

To evaluate possible anisotropy-induced distortions of the geometrical spreading, we applied our algorithm to the reflection from the top of the reservoir (Figure 3.12). The moveout parameters were obtained by Vasconcelos and Tsvankin (2004) using equations 7.9–7.10. The influence of anisotropy causes a dramatic 50% distortion in the geometrical spreading for offset-to-depth ratios close to two. The magnitude of the azimuthal variation of the factor L at offset-to-depth ratios slightly larger than unity reaches 10% (Figure 3.13). Such a difference between the geometrical spreading in the east-west and north-south directions may cause noticeable distortions in the azimuthal variation of the AVO gradient studied by Jenner (2001).

3.5 Discussion and conclusions

The formalism suggested in Paper I provides an analytic basis for geometrical-spreading correction in layered azimuthally anisotropic media. Since the correction involves only the spatial derivatives of the reflection traveltimes and the group-velocity vector at the source/receiver locations, it does not require knowledge of the velocity field beneath the subsurface layer. The main issue in computing geometrical spreading for purposes of wide-angle azimuthal AVO analysis is to find a sufficiently accurate, smooth approximation for long-offset, multiazimuth reflection moveout in the presence of azimuthal anisotropy.

Numerical testing shows that even for models composed of strongly anisotropic orthorhombic layers, long-spread P-wave reflection traveltimes can be accurately described by a nonhyperbolic moveout equation that has the same form as the widely used Alkhalifah-Tsvankin equation for VTI media. Keeping the same general form of the moveout equation for azimuthally anisotropic and VTI media helps to facilitate the transition between models with different symmetries in both the moveout inversion and geometrical-spreading correction. To accommodate the influence of azimuthal anisotropy, both moveout coefficients - the NMO velocity V_{nmo} and the anellipticity parameter η - have to vary with the azimuth α . While $V_{\text{nmo}}(\alpha)$ traces out an ellipse in media of almost any complexity, the form of the

function $\eta(\alpha)$ depends on the degree of alignment of the symmetry planes in the constituent layers.

If the azimuths of the vertical symmetry planes do not change from layer to layer, the model as a whole has two orthogonal symmetry planes, and the azimuthal dependence of η [equation 7.10] is the same as in a homogeneous orthorhombic medium. For purposes of geometrical-spreading correction, such a model is fully equivalent to a single orthorhombic layer. The moveout equation is then controlled by the azimuth ϕ of one of the symmetry planes, two symmetry-plane NMO velocities $V_{\text{nmo}}^{(1,2)}$, and three anellipticity parameters $\eta^{(1,2,3)}$ that govern $\eta(\alpha)$. For media with depth-varying orientation of the symmetry planes, the accuracy of the moveout equation can be maintained by introducing an additional azimuthal angle ϕ_1 that governs the direction of the “principal axes” of the function $\eta(\alpha)$. The moveout parameters, which serve as the input in the computation of geometrical spreading, are determined using the algorithm of Vasconcelos and Tsvankin based on a 3D nonhyperbolic semblance operator.

Synthetic tests for layered orthorhombic media illustrate the high sensitivity of the spatially varying geometrical spreading to the anisotropic parameters. The magnitude of the anisotropy-induced azimuthal variation of the geometrical spreading may exceed that of the reflection coefficient.¹ Therefore, anisotropic geometrical-spreading correction should be considered an integral part of azimuthal AVO inversion.

The importance of correcting wide-azimuth data for geometrical spreading prior to AVO analysis was highlighted by applying the algorithm to field data acquired at Weyburn field in Canada. The geometrical-spreading factor for the reflection from the top of the fractured reservoir is influenced by the ellipticity of the NMO-velocity function and, especially, by the large values (exceeding 0.2) of the effective parameters $\eta^{(1,2,3)}$. The reliability of the AVO attributes can be improved by taking into account the variation of the geometrical spreading between the symmetry planes (i.e., between the east-west and north-south directions). Note that although information about the effective anisotropy is contained in the input moveout parameters, the difference between the geometrical-spreading factors computed for the top and bottom of a fractured layer can potentially serve as a fracture-detection attribute.

The sensitivity study shows that our geometrical-spreading algorithm is sufficiently robust in the presence of moderate traveltimes errors. Still, the results of traveltimes fitting and, therefore, geometrical-spreading correction may be somewhat distorted by coherent noise associated, for example, with short-period statics. Also, in the presence of significant amplitude variation with offset and azimuth, it is preferable to estimate the moveout parameters using an AVO-sensitive algorithm.

¹Comparisons of this type, however, strongly rely on the model assumptions because the geometrical spreading of reflected waves is independent of the elastic parameters beneath the reflector.

3.6 References

- Al-Dajani, A., I. Tsvankin, and M. N. Toksöz, 1998, Nonhyperbolic reflection moveout for azimuthally anisotropic media: 68th Annual International Meeting, SEG, Expanded Abstracts, 1479–1482.
- Alkhalifah, T., and I. Tsvankin, 1995, Velocity analysis for transversely isotropic media: *Geophysics*, **60**, 1550–1566.
- Bakulin, A., V. Grechka, and I. Tsvankin, 2000, Estimation of fracture parameters from reflection seismic data – Part II: Fractured models with orthorhombic symmetry: *Geophysics*, **65**, 1803–1817.
- Cardona, R., 2002, Fluid substitution theories and multicomponent seismic characterization of fractured reservoirs: PhD thesis, Colorado School of Mines.
- Červený, V., 2001, *Seismic ray theory*: Cambridge University Press.
- Gajewski, D., and I. Pšenčík, 1990, Vertical seismic profile synthetics by dynamic ray tracing in laterally varying layered anisotropic structures: *Journal of Geophysical Research*, **95**, 11301–11315.
- Grechka, V., and I. Tsvankin, 1998, 3-D description of normal moveout in anisotropic inhomogeneous media: *Geophysics*, **63**, 1079–1092.
- Grechka, V., and I. Tsvankin, 1999a, 3-D moveout inversion in azimuthally anisotropic media with lateral velocity variation: Theory and a case study: *Geophysics*, **64**, 1202–1218.
- Grechka, V., and I. Tsvankin, 1999b, 3-D moveout velocity analysis and parameter estimation for orthorhombic media: *Geophysics*, **64**, 820–837.
- Hall, S., and J. M. Kendall, 2003, Fracture characterization at Valhall: Application of P-wave amplitude variation with offset and azimuth (AVOA) analysis to a 3-D ocean-bottom data set: *Geophysics*, **68**, 1150–1160.
- Jenner, E., 2001, Azimuthal anisotropy of 3-D compressional wave seismic data, Weyburn field, Saskatchewan, Canada: PhD thesis, Colorado School of Mines.
- Lynn, H.B., D. Campagna, K. M. Simon, and W. E. Beckham, 1999, Relationship of P-wave seismic attributes, azimuthal anisotropy, and commercial gas pay in 3-D P-wave multiazimuth data, Rulison Field, Piceance Basin, Colorado: *Geophysics*, **64**, 1312–1328.
- Mallick, S., K. Craft, and L. Meister, 1998, Determination of the principal directions of azimuthal anisotropy from P-wave seismic data: *Geophysics*, **63**, 692–706.

- Maultzsch, S., S. Horne, S. Archer, and H. Burkhardt, 2003, Effects of an anisotropic overburden on azimuthal amplitude analysis in horizontal transverse isotropic media: *Geophysical Prospecting*, **51**, 61–74.
- Pech, A., and I. Tsvankin, 2004, Quartic moveout coefficient for a dipping azimuthally anisotropic layer: *Geophysics*, **69**, 699–707.
- Rüger, A., 2001, Reflection coefficients and azimuthal AVO analysis in anisotropic media: SEG.
- Schoenberg M. and K. Helbig, 1997, Orthorhombic media: Modeling elastic wave behavior in a vertically fractured earth: *Geophysics*, **62**, 1954–1974.
- Tsvankin, I., and L. Thomsen, 1994, Nonhyperbolic reflection moveout in anisotropic media: *Geophysics*, **59**, 1290–1304.
- Tsvankin, I., 1995, Body-wave radiation patterns and AVO in transversely isotropic media: *Geophysics*, **60**, 1409–1425.
- Tsvankin, I., 1997, Anisotropic parameters and P-wave velocity for orthorhombic media: *Geophysics*, **62**, 1292–1309.
- Tsvankin, I., 2005, *Seismic signatures and analysis of reflection data in anisotropic media*: Elsevier Science Publ. Co., Inc (second edition).
- Ursin, B., and K. Hokstad, 2003, Geometrical spreading in a layered transversely isotropic medium with vertical symmetry axis: *Geophysics*, **68**, 2082–2091.
- Vasconcelos, I., and I. Tsvankin, 2004, Inversion of P-wave nonhyperbolic moveout in azimuthally anisotropic media: Methodology and field-data application: 74th Annual International Meeting, SEG, Expanded Abstracts, 171–174 (also submitted to *Geophysical Prospecting*).
- Xu, X., I. Tsvankin, and A. Pech, 2005, Geometrical spreading of P-waves in horizontally layered, azimuthally anisotropic media: *Geophysics*, **70**, D43–D53.

Chapter 4

Estimation of reflection coefficients on full-waveform synthetic data

4.1 Introduction

Analysis of prestack amplitude variation with offset and azimuth (often called “azimuthal AVO analysis” or “AVAZ”) is one of the most effective tools for seismic characterization of fractures and in-situ stress field. The main advantage of amplitude methods compared to traveltimes inversion is their high vertical resolution that makes AVO analysis applicable to relatively thin reservoirs. Also, body-wave amplitudes are highly sensitive to seismic anisotropy and, in particular, to azimuthal velocity variations associated with vertical fracture systems and nonhydrostatic stresses.

Similar to traveltimes, reflection amplitudes recorded at the surface represent effective quantities influenced by the medium properties along the whole raypath. The goal of AVO analysis is to resolve the local physical parameters at the reservoir level using the reflection coefficient, which is hidden in the measured amplitude. Therefore, a critical element of AVO processing is separation of the reflection coefficient from the source signature and the propagation factors, most notably from the geometrical spreading in the overburden.

In practice, it is often assumed that as long as the overburden is structurally simple (e.g., layer-cake), it should not produce substantial amplitude distortions. This “common-sense” assumption, however, can be dangerously misleading if some of the overburden formations are anisotropic. Anisotropy above the reflector acts like a lens that focuses and defocuses seismic energy in accordance with angular velocity variations. In his book, Tsvankin (2005) gives striking examples of weakly anisotropic VTI (transversely isotropic with a vertical symmetry axis) models that produce dramatic amplitude variations along the wavefronts of both P- and S-waves. If not corrected for, this strong angle dependence of the anisotropic geometrical-spreading factor can compromise the AVO signature (e.g., the AVO gradient) and lead to erroneous interpretation of lithology and fluid content.

Furthermore, the AVO response for wide-azimuth data can be distorted by the azimuthal variation of geometrical spreading caused by aligned vertical fractures in the overburden (fractures often permeate much of the section above reservoirs). Still, most anisotropic AVO algorithms employ amplitude corrections conventionally used in isotropic processing (e.g., the t - or t^2 -gain factors). Such approximate amplitude treatment generally does not prevent azimuthal AVO analysis from estimating the dominant fracture directions, as attested by successful case studies reported in the literature (e.g., Hall and Kendall, 2003;

Gray and Todorovic-Marinic, 2004). However, to put the method on a firm quantitative footing and make it suitable for estimating the physical properties of fractures, one has to apply a more robust geometrical-spreading correction that honors the azimuthal anisotropy in the overburden.

In principle, the geometrical-spreading factor can be computed using dynamic ray tracing or other forward-modeling techniques. Unfortunately, the anisotropic velocity models are rarely accurate enough to make this approach practical. Therefore, we recently proposed a *moveout-based* anisotropic spreading-correction method, MASC that makes it possible to compute geometrical spreading for wide-angle reflections in horizontally-layered, azimuthally anisotropic media directly from the reflection traveltimes. The spreading correction is preceded by 3D nonhyperbolic moveout analysis using the semblance algorithm of Vasconcelos and Tsvankin (2006). The moveout parameters estimated from wide-azimuth data serve as the input to the geometrical-spreading correction. MASC does not require knowledge of the velocity model (except for the velocities in the layer containing the sources and receivers) and has been shown to be sufficiently robust in the presence of noise.

Here, we process full-waveform 3D synthetic reflection data to answer several important practical questions regarding MASC and anisotropic spreading correction for PP-waves:

1. Can MASC, despite its reliance on ray theory, accurately reconstruct reflection coefficients in the presence of strong azimuthal anisotropy?
2. Can we acceptably replace MASC with simple gain corrections commonly used in practice?
3. Is it possible to ignore the contribution of the transmission loss (which are not included in MASC) along the raypath?

We begin by describing the modeling code and the algorithm used to reconstruct the reflection coefficient from the picked amplitudes of reflected P-waves. Then we compare the performance of MASC and conventional gain corrections for three relatively simple models that include an orthorhombic layer beneath an isotropic overburden. Although most current implementations of azimuthal AVO analysis operate with HTI (TI with a horizontal symmetry axis) media, orthorhombic symmetry is more typical for realistic fractured reservoirs. Recent work of Grechka and Kachanov (2006) shows that orthorhombic models accurately describe even multiple sets of vertical fractures with arbitrary azimuthal orientations.

4.2 Synthetic modeling

The full-waveform modeling algorithm, based on the anisotropic version of the reflectivity method, is designed to simulate exact 3D wavefields for horizontally layered, anisotropic media. The reflectivity code, ANISYNPA, was originally developed by Dennis Corrigan at ARCO and later modified at the Center for Wave Phenomena.

All three models used here include an orthorhombic layer sandwiched between two isotropic media (see Tables 7.1, 7.2, and 6.3). One of the symmetry planes of the orthorhombic medium is horizontal, while the other two coincide with the coordinate planes $[x_1, x_3]$ (azimuth 0°) and $[x_2, x_3]$ (azimuth 90°). If the azimuthal anisotropy is caused by a single system of fractures in a VTI background, one of the vertical symmetry planes is

	Layer 1	Layer 2	Layer 3
Symmetry type	ISO	ORTH	ISO
Thickness (km)	0.5	1.0	∞
Density (g/cm ³)	2.1	2.1	2.12
V_{P0} (km/s)	2.1	2.2	2.3
V_{S0} (km/s)	1.05	1.1	1.15
$\epsilon^{(1)}$	0	0.317	0
$\delta^{(1)}$	0	-0.054	0
$\gamma^{(1)}$	0	0.513	0
$\epsilon^{(2)}$	0	0.121	0
$\delta^{(2)}$	0	0.046	0
$\gamma^{(2)}$	0	0.138	0
$\delta^{(3)}$	0	0.1	0
$\eta^{(1)}$	0	0.42	0
$\eta^{(2)}$	0	0.07	0
$\eta^{(3)}$	0	0.05	0

Table 4.1. Parameters of a three-layer medium used in the numerical tests (model 1). Orthorhombic symmetry can be fully described by the two vertical velocities (V_{P0} for P-waves and V_{S0} for one of the split S-waves) and seven anisotropy parameters ($\epsilon^{(1)}$, $\epsilon^{(2)}$, $\delta^{(1)}$, $\delta^{(2)}$, $\delta^{(3)}$, $\gamma^{(1)}$, and $\gamma^{(2)}$). The anellipticity parameters $\eta^{(1)}$, $\eta^{(2)}$, and $\eta^{(3)}$ control P-wave nonhyperbolic moveout. For a detailed explanation of the notation, see Tsvankin (2005).

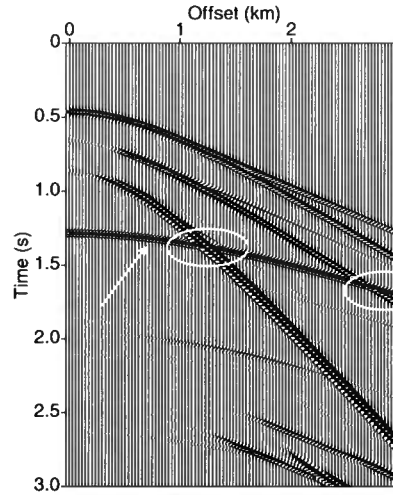


Figure 4.2. Synthetic gather for model 6.3 (Table 3) computed in the symmetry plane $[x_2, x_3]$ (azimuth 90°).

practice, the results of AVO processing often require smoothing because of noisy amplitudes, variations in the source and receiver coupling, etc.

4.3.1 Model 1

Existing laboratory measurements of the anisotropy parameters for orthorhombic media are obtained for synthetic materials (e.g., phenolic). Therefore, the parameters of the orthorhombic layer in model 1 (see Table 7.1) are based on Wang's (2002) results for two transversely isotropic brine-saturated shale samples. The main reason for choosing this model is that the large difference between the SH-wave parameters $\gamma^{(1)}$ and $\gamma^{(2)}$ causes an extremely pronounced azimuthal variation of the P-wave AVO gradient. Note that $\gamma^{(1)} = 0.513$ is much higher than the average value of Thomsen's γ for shales (0.2), so this model likely exaggerates the typical magnitude of the azimuthal AVO response.

The PP-wave reflection coefficient from the bottom of the orthorhombic layer reconstructed by our algorithm (i.e., using the moveout-based geometrical-spreading correction) and by the empirical t^2 -gain is marked by dashed lines in Figures 4.3a,b. (We chose the t^2 -function because it generally gives better results for our models than the linear t -compensation or Newman's correction.) For comparison, Figure 4.3 also displays the exact reflection coefficient (solid lines). To remove the source factor, the estimated reflection coefficient is normalized to match the exact value at normal incidence (zero offset).

The maximum horizontal slowness (0.3 s/km) in Figure 4.3 corresponds to an incidence angle at the source close to 40° (it varies with azimuth) and an offset-to-depth-ratio slightly

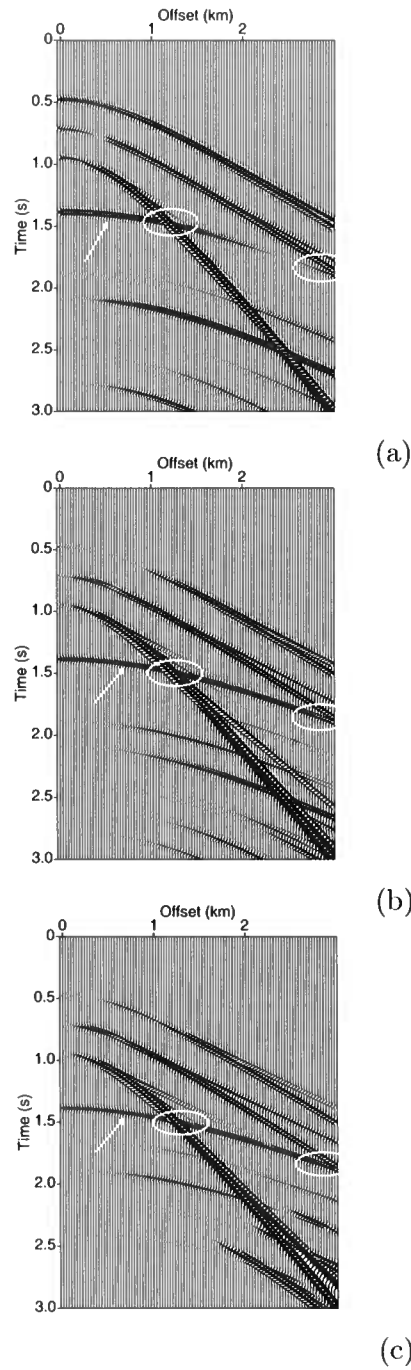


Figure 4.1. Synthetic shot gathers for model 7.1 (Table 1) computed by the reflectivity method in three azimuthal directions: (a) 0° (symmetry plane $[x_1, x_3]$); (b) 45° ; and (c) 90° (symmetry plane $[x_2, x_3]$). The top layer is specified as a halfspace to eliminate the influence of the free surface. The arrows mark the target PP-wave reflected from the bottom of the orthorhombic layer. The ellipses highlight the areas of interference of the target PP event with the PS and SS reflections from the top of the orthorhombic layer.

aligned with the fracture strike. Synthetic seismograms were computed for a wide range of offsets in both vertical symmetry planes, as well as for the 45° -azimuth. The code calculates three displacement components of the wavefield excited by a point force parallel to one of the coordinate axes.

The vertical displacement from a vertical force for model 7.1 is displayed in Figure 4.1. Our goal is to carry out azimuthal AVO analysis for the PP-wave reflected from the bottom of the orthorhombic layer (this event is marked by the arrows) for all three models. To avoid the interference of this PP reflection with ground roll and surface-related multiples, we eliminated the free surface in the computation of the synthetic seismograms. Still, the target PP event interferes with the PS- and SS-wave reflections from the top of the orthorhombic layer, particularly for model 3 (Figure 4.2), which causes distortions of the picked AVO response.

4.3 Estimation of the reflection coefficient from the AVO response

The moveout-based anisotropic geometrical-spreading correction was implemented for layered orthorhombic and HTI media in the Seismic Unix program SUAZAVO. MASC computes the offset- and azimuth-dependent geometrical-spreading factor for a given reflection event using the zero-offset time t_0 and effective moveout parameters $V_{\text{nmo}}^{(1)}$, $V_{\text{nmo}}^{(2)}$, $\eta^{(1)}$, $\eta^{(2)}$, and $\eta^{(3)}$. The symmetry-plane normal-moveout (NMO) velocities $V_{\text{nmo}}^{(1)}$ and $V_{\text{nmo}}^{(2)}$ determine the NMO ellipse on conventional spreads, while $\eta^{(1)}$, $\eta^{(2)}$, and $\eta^{(3)}$ are the anellipticity parameters (they are similar to the parameter η for VTI media) responsible for nonhyperbolic (long-spread) moveout. The moveout parameters are estimated with a global semblance algorithm that maximizes semblance computed for all offsets and azimuths in the gather. It should be emphasized that the geometrical-spreading correction is not influenced by the trade-offs between the NMO velocities and η parameters, as long as the reconstructed moveout function is sufficiently close to the actual traveltimes.

The processing flow starts with picking the raw amplitudes of a certain event on all traces along the traveltimes surface defined by the estimated moveout parameters. Then the picked amplitudes are corrected for the anisotropic geometrical spreading computed for each offset and azimuth. Finally, assuming that the sources and receivers are located in an isotropic layer with a known P-wave velocity, the algorithm removes the source and receiver directivity factors using local time slopes (i.e., horizontal slownesses) calculated from the moveout function.

Since our models are nonattenuative, the corrected amplitude should be determined primarily by the plane-wave reflection coefficient. The only propagation factor not accounted for in this algorithm is the product of the transmission coefficients along the ray-path, which is usually close to a constant (see below). A scalar related to the strength of the source can be removed by simple normalization.

The output amplitudes have to be smoothed to mitigate the distortions caused by the interference of the PP reflection with shear and converted waves (see the ellipses in Figures 4.1 and 4.2). The smoothing was accomplished by least-squares fitting of a fourth-order polynomial in the horizontal slowness to the reconstructed reflection coefficients. In

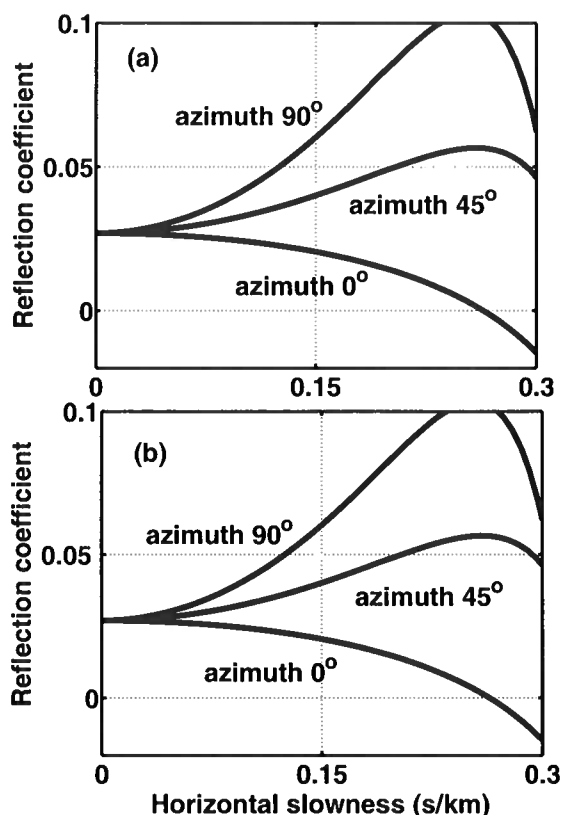


Figure 4.3. Comparison of the reconstructed (dashed lines) and exact (solid lines) reflection coefficients for the PP-wave reflected from the bottom of the orthorhombic layer in model 7.1. The reflection coefficient is estimated using (a) MASC; and (b) the t^2 -gain. The offset-to-depth ratio that corresponds to the maximum horizontal slowness (0.3 s/km) is slightly larger than two.

larger than two. The slownesses up to 0.15 s/km (the corresponding incidence angle is up to 20°) define what we will call the near-offset amplitude response; the reflection coefficient in this slowness range is governed mostly by the AVO gradient.

Clearly, for near offsets the MASC algorithm recovers the reflection coefficient with extremely high accuracy (Figure 4.3a). The small deviation of the estimated reflection coefficient from the exact curve at far offsets for azimuths of 45° and 90° is related to the interference with shear and mode-converted waves (Figures 4.1b and 4.1c). The excellent agreement between the reconstructed and exact reflection coefficients for a wide range of offsets and azimuths is ensured by the application of the moveout-based geometrical-spreading correction. Figure 4.4 confirms that the output of MASC for all three azimuths practically coincides with the geometrical spreading computed by dynamic ray tracing.

The performance of the simple t^2 -gain correction often used in practice varies with azimuth (Figure 4.3b). For an azimuth of 0° the estimated reflection coefficient is close to the exact value for the full offset range. The accuracy of the t^2 -gain, however, is much lower

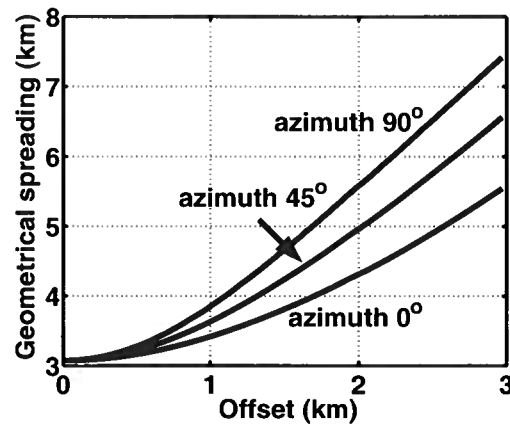


Figure 4.4. Comparison of the geometrical spreading computed by MASC (dashed lines) and dynamic ray tracing (solid) for the PP reflection from the bottom of the orthorhombic layer in model 7.1.

for the other two azimuths, especially at far offsets.

Since the traveltimes depends on both polar and azimuthal velocity variations, the t^2 -function absorbs some of the influence of the anisotropy on the geometrical-spreading factor. For that reason, the t^2 -gain happens to be adequate for the 0° -azimuth, although it does not accurately reproduce the variation of the spreading away from that direction. Still, it is clear from Figure 4.3b that the error of the t^2 -correction does not seriously compromise qualitative analysis of the AVO gradient as a function of azimuth. For model 1, the variation of the AVO gradient between the symmetry planes is so pronounced that the geometrical-spreading factor does not have to be computed with high accuracy. Quantitative inversion of the AVO response on long-spread gathers, however, should be based on the MASC algorithm.

4.3.2 Model 2

The second model is designed in such a way that the geometrical spreading of the target event from the bottom of the orthorhombic layer is the same as that in model 1, but the azimuthal variation of the reflection coefficient is much less pronounced (which is more typical for field data). The ratio of the overall azimuthal variation of the geometrical spreading and that of the reflection coefficient (estimated at a horizontal slowness of 0.15 s/km) for model 7.2 reaches 40%. In the absence of interference with other arrivals at large offsets, the reflection coefficient recovered by MASC is almost identical to the exact value for the whole range of offsets and azimuths (Figure 4.5a).

The impact of the errors produced by the t^2 -gain in this model is amplified by the relatively weak azimuthal dependence of the reflection coefficient (Figure 4.5b). The reflection

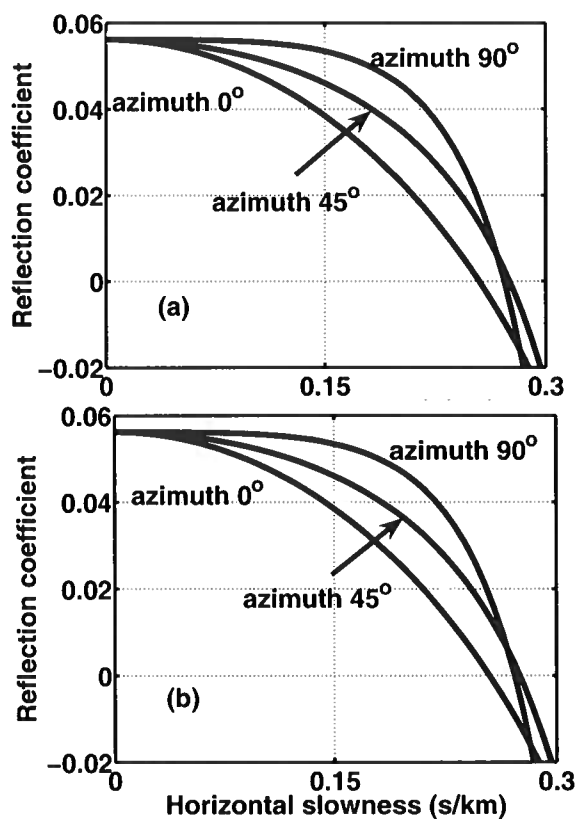


Figure 4.5. Comparison of the reconstructed (dashed lines) and exact (solid) reflection coefficients for model 7.2. The reflection coefficient is estimated using (a) MASC; and (b) the t^2 -gain. The reconstructed reflection coefficients for the 45°- and 90°-azimuths on plot (b) practically coincide with one another; for the 0°-azimuth, the reconstructed coefficient is almost invisible because it is close to the exact value. The offset-to-depth ratio that corresponds to the maximum horizontal slowness (0.3 s/km) is close to two.

	Layer 1	Layer 2	Layer 3
Symmetry type	ISO	ORTH	ISO
Thickness (km)	0.5	1.0	∞
Density (g/cm ³)	2.1	2.1	2.12
V_{P0} (km/s)	2.1	2.2	2.3
V_{S0} (km/s)	1.05	1.1	1.15
$\epsilon^{(1)}$	0	0.317	0
$\delta^{(1)}$	0	-0.054	0
$\gamma^{(1)}$	0	0.138	0
$\epsilon^{(2)}$	0	0.121	0
$\delta^{(2)}$	0	0.046	0
$\gamma^{(2)}$	0	0.03	0
$\delta^{(3)}$	0	0.1	0
$\eta^{(1)}$	0	0.42	0
$\eta^{(2)}$	0	0.07	0
$\eta^{(3)}$	0	0.05	0

Table 4.2. Parameters of model 7.2. We modified model 7.1 to reduce the azimuthal variation of the reflection coefficient while keeping the geometrical-spreading factor unchanged.

coefficients after the t^2 -gain are close for all three azimuths (and practically coincide for 45° and 90°, even at far offsets). Evidently, such small azimuthal differences in amplitude would be undetectable in the presence of realistic noise. Hence, application of the empirical t^2 -correction for this model obliterates the azimuthal AVO signature and makes it useless for fracture-detection purposes.

4.3.3 Model 3

The parameters of the orthorhombic layer in model 6.3 are typical for a set of parallel, vertical, penny-shaped cracks embedded in a VTI background medium (the so-called “standard orthorhombic model” of Schoenberg and Helbig). The reflection coefficient for the PP reflection from the bottom of the orthorhombic layer computed by MASC remains accurate up to a horizontal slowness of about 0.2 s/km (Figure 4.6a). For larger slownesses (i.e., at far offsets) the reconstructed reflection coefficient is severely distorted by the interference of the target event with the PS conversion from the top of the orthorhombic layer (see Figure 4.2). Note that for model 6.3 the slowness 0.15 s/km corresponds to an incidence angle close to 25° (slightly higher than that for model 7.1) and an offset-to-depth ratio of one.

The t^2 -gain correction for this model works better than for model 2 but worse than for model 1 (Figure 4.6b). [The ratio of the overall azimuthal variation of the geometrical

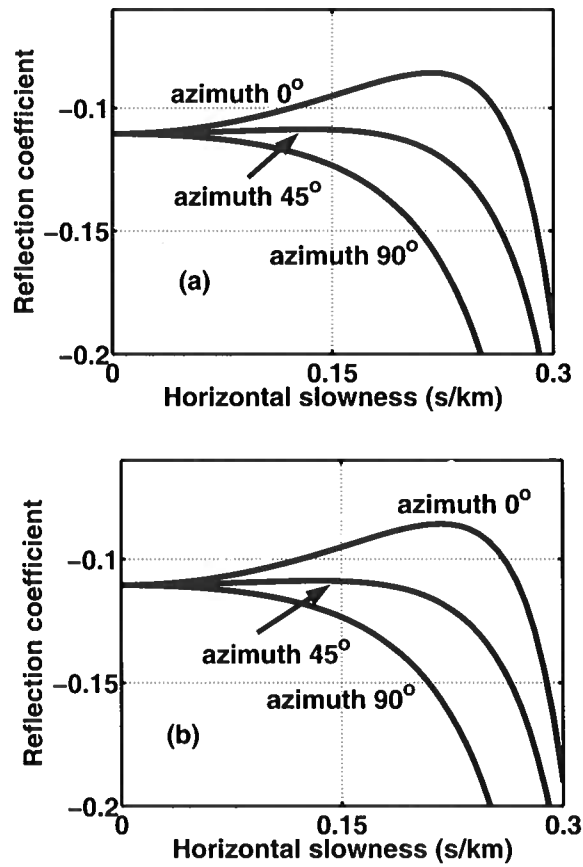


Figure 4.6. Comparison of the reconstructed (dashed lines) and exact (solid) reflection coefficients for model 6.3. The reflection coefficient is estimated using (a) MASC; and (b) the t^2 -gain. The offset-to-depth ratio that corresponds to the maximum horizontal slowness (0.3 s/km) is close to 2.5.

	Layer 1	Layer 2	Layer 3
Symmetry type	ISO	ORTH	ISO
Thickness (km)	0.5	1.0	∞
Density (g/cm ³)	2.44	2.70	2.44
V_{P0} (km/s)	2.16	2.437	2.16
V_{S0} (km/s)	1.150	1.265	1.150
$\epsilon^{(1)}$	0	0.329	0
$\delta^{(1)}$	0	0.083	0
$\gamma^{(1)}$	0	0.046	0
$\epsilon^{(2)}$	0	0.258	0
$\delta^{(2)}$	0	-0.078	0
$\gamma^{(2)}$	0	0.182	0
$\delta^{(3)}$	0	-0.106	0
$\eta^{(1)}$	0	0.211	0
$\eta^{(2)}$	0	0.398	0
$\eta^{(3)}$	0	0.194	0

Table 4.3. Parameters of model 6.3. The orthorhombic layer corresponds to the “standard” orthorhombic model of Schoenberg and Helbig (1997).

spreading and that of the reflection coefficient (estimated at a horizontal slowness of 0.15 s/km) for model 6.3 is 15%]. For all three azimuths, the reflection coefficient after the t^2 -correction is larger than the exact value, and the error becomes noticeable at relatively small offsets. The reconstructed reflection coefficient in the 90°-direction even has the wrong sign of the AVO gradient. However, while the t^2 -gain is clearly inadequate for purposes of quantitative AVO inversion, it correctly reproduces the azimuthal trend of the AVO gradient between the vertical symmetry planes.

4.4 Influence of the transmission loss

The transmission coefficients along the raypath are not part of the geometrical-spreading correction, and are difficult to estimate from surface data. To evaluate the transmission loss for our models, we subtract from unity the product of the transmission coefficients along the raypath of the target PP reflection (Figure 7.7). For all three models, the transmission loss becomes noticeable only at far offsets, but the related azimuthal amplitude variation is substantially smaller than that of the reflection coefficient (e.g., compare Figure 7.7a with the solid curves in Figure 4.3). Therefore, the transmission loss can be considered a secondary factor in azimuthal AVO analysis, which is confirmed by the high accuracy of MASC in our examples.

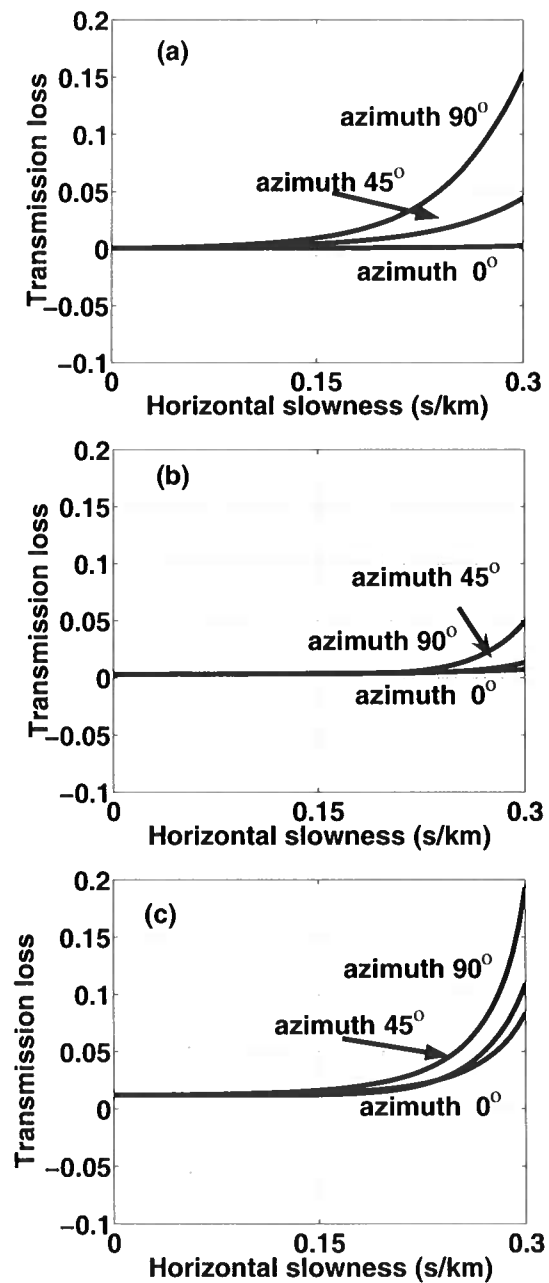


Figure 4.7. Transmission loss for the PP reflection from the bottom of the orthorhombic layer in (a) model 7.1; (b) model 7.2; and (c) model 6.3. The loss is computed by subtracting from unity the product of the plane-wave transmission coefficients along the raypath.

4.5 Discussion

Our modeling results show that application of MASC is essential when the azimuthal variation of the geometrical spreading is not negligible compared to that of the reflection coefficient, a situation that commonly can arise in practice where the overburden is fractured. It is important to keep in mind that geometrical spreading and reflection coefficient are governed by two different sets of medium parameters defined at different scales. When the model is orthorhombic, the azimuthal variation of the P-wave AVO gradient is controlled by the *local* jump in the shear-wave splitting parameter and in the difference between the Thomsen-type δ parameters ($\delta^{(2)} - \delta^{(1)}$) across the target interface. In contrast, geometrical spreading of reflected waves depends on the *effective* (average) parameters of the overburden.

If fracturing is largely limited to the reservoir formation, the azimuthal amplitude variation of the reflection from the top of the reservoir generally follows the reflection coefficient (the case of our model 1). This explains why the results of azimuthal AVO analysis with the conventional (isotropic) spreading correction often are in good agreement with other fracture-characterization methods. However, natural fractures that respond to the local stress field often permeate the whole section and lead to substantial azimuthal anisotropy in the overburden. In such cases, application of MASC is highly beneficial even for purposes of “qualitative” AVO analysis designed to estimate the relative change in the AVO response between the symmetry planes. Also, the azimuthal variation of geometrical spreading is more significant for the reflection from the *bottom* of the reservoir, especially for relatively thick reservoir layers. Note that the moveout and geometrical spreading of reflections from beneath the reservoir contain useful information for reservoir characterization, which is complementary to that provided by the reflection coefficient.

Long-offset reflection data used in our synthetic study help to increase the sensitivity of the azimuthal AVO response to the anisotropy (e.g., fracture) parameters. However, even if amplitude analysis is restricted to the AVO gradient estimated on conventional offsets, the geometrical-spreading correction can benefit from nonhyperbolic moveout inversion for the anellipticity parameters $\eta^{(1,2)}$. Although this result seems counterintuitive, it is explained by the strong dependence of geometrical spreading on the second travelttime derivative with respect to offset.

Conclusions

The transformation of seismic amplitudes measured at the surface into the reflection coefficient at the target horizon is a critically important step in AVO analysis. Here, we tested the moveout-based anisotropic geometrical-spreading correction (MASC) on long-offset, wide-azimuth synthetic data from three models, which included a strongly anisotropic layer of orthorhombic symmetry. The results show that although MASC is based on ray theory, it accurately reconstructs the azimuthally varying reflection coefficient for a wide range of offsets and azimuths. The errors in the estimated reflection coefficient are mostly caused by interference-related amplitude distortions.

In practice, azimuthal AVO analysis often involves an empirical gain correction designed to compensate for the amplitude loss in the overburden. Our tests demonstrate that although the t^2 -gain absorbs some of the influence of anisotropy on geometrical spreading, it produces significant errors in the reflection coefficient, especially for offsets-to-depth ratios greater than unity. Therefore, the empirical correction cannot be used in quantitative inversion of the azimuthally varying AVO response for the anisotropy parameters (e.g., for the fracture compliances).

On the other hand, most existing applications of azimuthal AVO are limited to estimating the principal azimuthal directions of the AVO gradient and its variation between the vertical symmetry planes. This relative azimuthal change in the AVO gradient measured over a fractured reservoir is then used to identify “sweet spots” of high fracture density. For models where the azimuthal variation of the reflection coefficient is much more pronounced than that of geometrical spreading (e.g., our models 1 and 3), the t^2 -gain is sufficient to reproduce the general azimuthal trend of the reflection coefficient.

However, as the ratio of the overall azimuthal variation of the geometrical spreading and that of the reflection coefficient (estimated for an incidence angle of about 20°) increases to 40% in model 2, the empirical correction completely smears the AVO signature. For model 2, the reflection coefficient after the t^2 -gain is so weakly dependent on azimuth that it contains almost no information about the reservoir. On the whole, application of MASC becomes essential even in qualitative AVO analysis when the azimuthal variation of the geometrical spreading reaches about 1/3 of that of the reflection coefficient.

It should be emphasized that the MASC algorithm can be conveniently incorporated into the processing flow prior to velocity model-building at almost no extra cost. Indeed, azimuthal AVO analysis has to be preceded by a moveout correction designed to flatten the event of interest. The estimated effective moveout parameters can then be used as the input to the MASC algorithm, which does not require any other information about the velocity model (with the exception of the layer that contains the sources and receivers).

Chapter 5

Case studies of azimuthal AVO analysis with anisotropic spreading correction

5.1 Introduction

In tight, low-porosity reservoirs, cost-effective production often relies on a good understanding of the subsurface fracture network. A range of direct and indirect methods can be used to delineate fracture characteristics and their spatial variations. Such techniques include image logs, coherence analysis of images, and measurements of seismic anisotropy. While image logs provide direct estimates of fracture counts and orientations on various scales, these measurements are restricted to the vicinity of the well. Fault mapping by coherence analysis might suggest the spatial distribution of cracks, but it encounters challenges when the correlation between the spatial distribution of faults and fractures is not straightforward to establish.

Measurement of anisotropy using the azimuthal variation of normal-moveout (NMO) velocity and amplitude-variation-with-offset (AVO) of P-waves is an inexpensive and reliable tool for characterizing fracture population (Bakulin, et al., 2000; Li, et al. 2003; Neves, et al. 2003; Perez, et al. 1999; Rüger, 2001). The presence of preferentially oriented fractures results in azimuth-dependent NMO velocities and AVO gradients that can be used to infer the fracture orientation and density. After cross-validation with direct measurements, fracture maps obtained from the azimuthal seismic attributes can be employed as inputs into reservoir simulation.

Both the azimuthal AVO (often abbreviated as “AVAZ”) and NMO attributes have their own advantages. Azimuthal AVO analysis, on one hand, provides local information about the cracks at the target horizon; the NMO ellipse, on the other hand, reveals average properties of the fractures in the entire reservoir. When combined together, azimuthal AVO and NMO analyses offer an improved understanding of the subsurface fracture network. From the processing perspective, both techniques have advantages and challenges. While velocity measurements usually are more robust, amplitude is much more sensitive to the presence of anisotropy and, therefore, provides higher vertical resolution and stronger signal. Besides the difficulties caused by the near surface (e.g., statics and coupling), the removal of overburden distortions presents challenges for both techniques. To obtain interval azimuthal NMO velocities, the generalized Dix equation can be used to layer-strip overburden effects (Grechka and Tsvankin, 1998). It is well understood when this operation becomes unstable (Grechka et al., 1999; Neves, 2003; Perez, 1999). It is less known, however, that removal

of amplitude distortions caused by anisotropic overburden, in particular of geometrical spreading, should be an integral part of estimation of azimuthal AVO gradients (Tsvankin, 2005; Rüger and Tsvankin, 1997).

Xu et al. (2005) and Xu and Tsvankin (2006a, 2006b) developed a methodology of moveout-based anisotropic spreading correction (MASC) and showed its importance on synthetic data. Their algorithm uses 3D nonhyperbolic moveout parameters and requires no additional information about the subsurface velocity field. MASC is applied after 3D nonhyperbolic moveout inversion (Vasconcelos and Tsvankin, 2006), and fits in a straightforward way into the processing sequence designed to estimate the azimuthal AVO gradients. Here, we apply MASC to wide-azimuth data acquired at the Rulison field, Colorado to evaluate its effectiveness on results of azimuthal AVO analysis. Among other issues, we investigate the distribution of enhanced fracture zones in the Rulison field.

5.2 Geologic background

The Rulison field is a basin-centered gas accumulation located in the South Piceance Basin, Garfield County, Colorado (Figure 5.1). Gas production is primarily from the Williams Fork formation, which consists of channel sand lenses embedded in fine-grained levee deposition (Figure 5.2). The reservoir is capped by the UMV shale, beneath which water saturates the upper reservoir for a few hundred feet (Cumella and Ostby, 2003). Massive shale formation overlies the unconformity at the top of the Mesaverde group. The bottom of the reservoir is bounded by the Cameo coal, which provides source for the gas accumulated in the reservoir.

The lithology of the reservoir formation is classified as tight sand with matrix permeability on the order of micro-Darcies and porosity of 6–12%. Because of the low porosity and permeability, it is of utmost importance to map the fracture networks for cost-effective development of the field.

5.3 Data acquisition and processing

To improve the understanding of the fracture network and the in-situ stress field, the Reservoir Characterization Project (RCP) acquired a 3D multicomponent seismic survey over a 2.2-by-2.5 km area of the Rulison field. The acquisition geometry was designed to be orthogonal to reach optimal balance between the uniformity of the azimuthal distribution and the economy of the layout (Figure 5.3). Listed in Table 15.3 are the acquisition parameters, which were used to collect dense data with the highest fold of 225 for a small bin size of 55-by-55 ft (Figure 5.4).

Prior to our processing, statics correction was applied to the data by Veritas. As illustrated by the cross-section in the middle of the survey, the data quality is decent for land seismics (Figure 5.5). Also, the subsurface structure is close to layer-cake, which simplifies application of azimuthal moveout and AVO analysis, as well as the anisotropic geometrical-spreading correction (MASC).

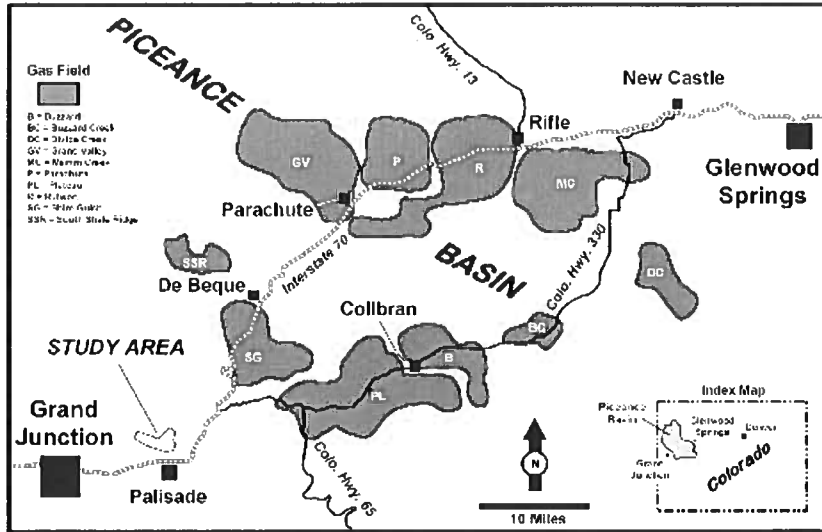


Figure 5.1. Map of the Rulison field (indicated by R), Piceance Basin, Colorado.

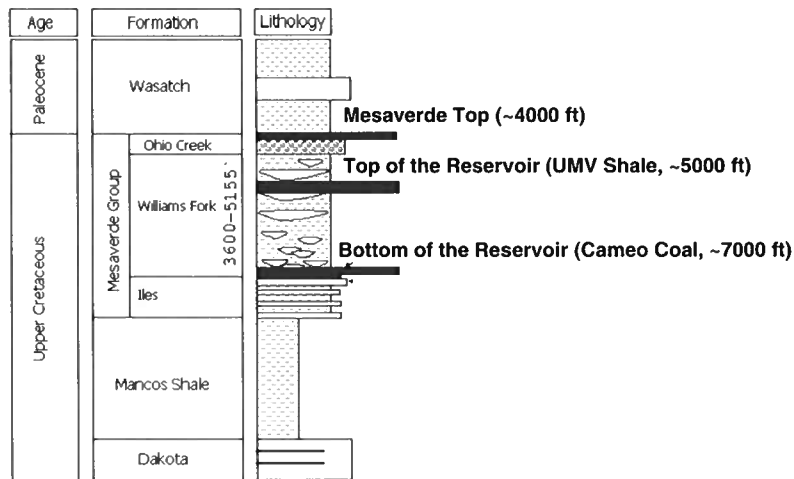


Figure 5.2. Stratigraphic column of the Rulison field. The gas-producing reservoir is bounded by the UMV Shale and the Cameo Coal. The Mesaverde Top is an unconformity that separates the Mesaverde group from the overlying Wasatch formation.

Survey type	3-D, 9-C
Subsurface bin size	55'x55'
Number of receiver locations	1500
Number of source locations	770
Receiver grid	110' inline spacing, 330' between lines
Source grid	110' inline spacing, 660' between lines
Receiver array	1, 3-C VectorSeis System Four
Source array	Mertz 18
P-wave sweep range	6-120 Hz

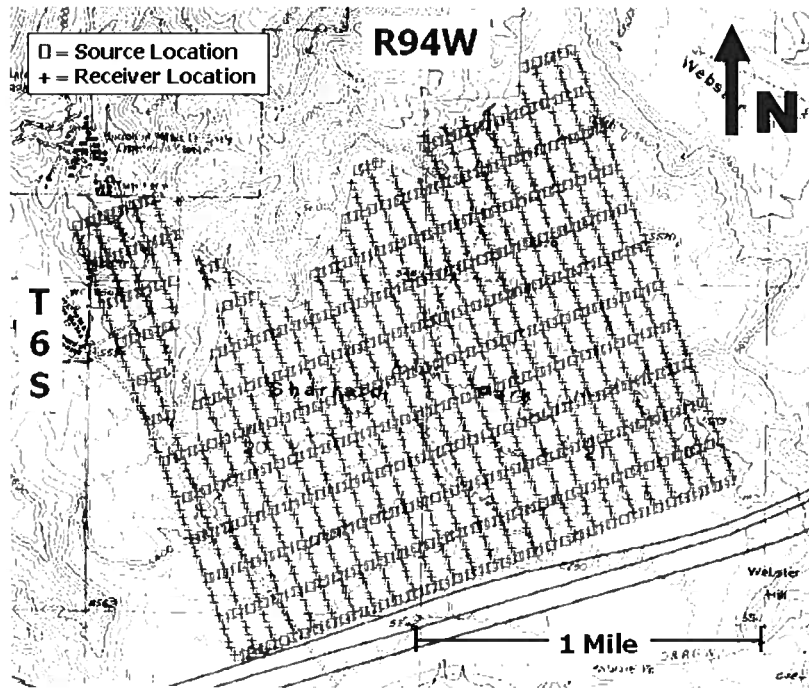


Figure 5.3. Seismic acquisition grid for the RCP nine-component 2003 survey.

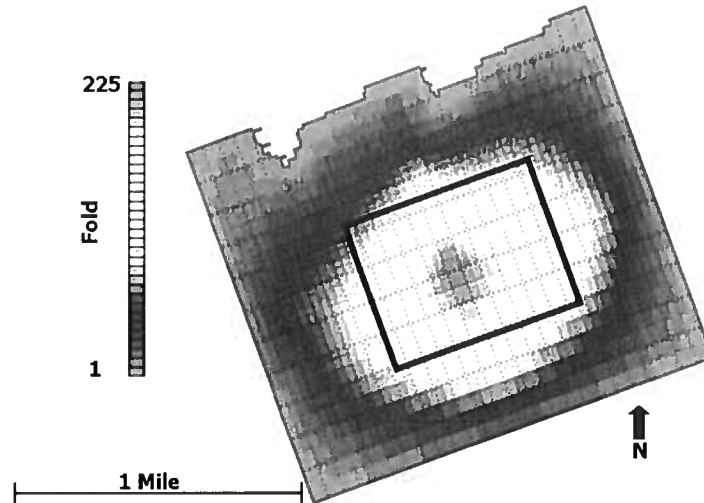


Figure 5.4. P-wave fold for the 55x55 ft binsize. The square in the center encompasses the study area of this paper.

To increase azimuth and offset coverage, we combined CMP gathers into superbins. The choice of superbin size is based on the smallest value that provides adequate coverage in offset and azimuth and sufficiently high semblance values. Relatively small bins suffer from non-uniformity of the distribution of offsets and azimuths; on the other hand, use of large bins increases the influence of lateral heterogeneity. By trying different superbin sizes, we found 5x5 bins to be optimal. Figure 7.5a displays a 5x5 superbin gather at northwest corner of our study area. The ground roll in the gather was suppressed using an azimuth-friendly slope filter suggested by Vasconcelos and Grechka (2006). Figure 7.5b shows the same gather after the application of azimuthally-varying NMO correction (i.e., using the NMO ellipse). The bending at the far offsets for the reflection from the top of the reservoir (UMV Shale) indicates the presence of nonhyperbolic moveout (Figure 7.5b). Since for this gather the offset-to-depth-ratio at the bottom of the reservoir (Cameo Coal) is only slightly larger than unity, the apparent flatness of the event does not necessarily imply the lack of nonhyperbolic moveout.

The azimuthally-varying NMO velocity traces out an ellipse even for anisotropic inhomogeneous media (Grechka and Tsvankin, 1998). Similarly, the azimuthal variation of AVO gradient can often be approximated by an elliptical curve (Rüger, 2001). The orientation and eccentricity of both ellipses reflect the fracture directions and intensities in the subsurface. To extract NMO and AVO ellipses, it is common to divide 3D data into azimuthal

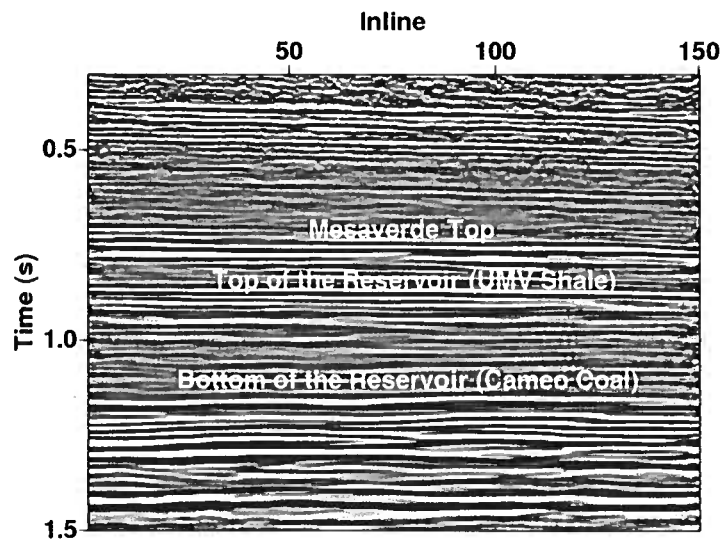
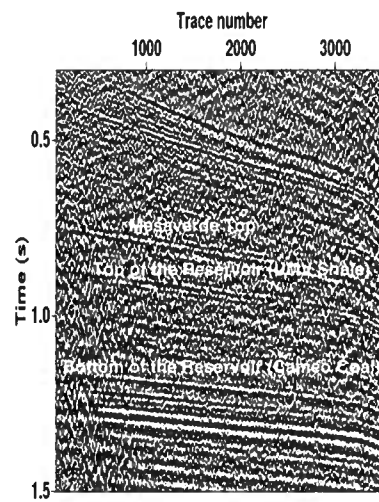
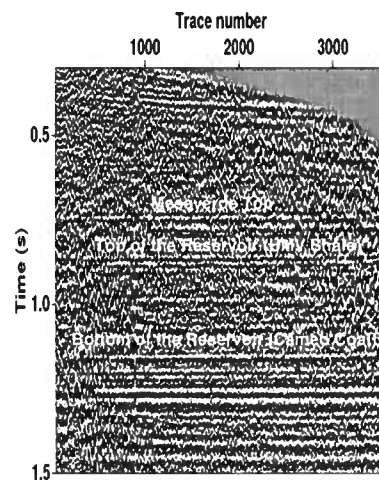


Figure 5.5. Seismic section across the middle of the survey area. The reflectors analyzed in the paper are marked on the plot.



(a)



(b)

Figure 5.6. (a) A 5x5 CMP supergather at the north-west corner of our study area; (b) the same gather after application of azimuthally-varying normal-moveout correction. The maximum offset for the gather is 7700 feet. The maximum offset-to-depth-ratios for the Mesaverde Top, the top of the reservoir (UMV Shale), and the bottom of the reservoir (Cameo Coal) are 1.9, 1.5, and 1.1, respectively.

sectors. For each sector, the NMO velocity and AVO gradient are inverted separately. The obtained NMO velocities and AVO gradients for different sectors are then combined to estimate the best-fit ellipses. While this approach allows application of existing 2D algorithms, it suffers from bias when the sector width is too large and uncertainty when it is too small (Li et al. 2003). Here, we adopted a more accurate algorithm that honors the azimuth of each trace and fits an ellipse to the data globally using all azimuths and offsets within a CMP gather (Grechka and Tsvankin, 1999; Vasconcelos and Tsvankin, 2006).

To estimate the AVO and NMO ellipses from CMP superbins, we implemented the following processing sequence. First, we employed a semblance method to obtain the NMO ellipse from near-offset traces (i.e., offset-to-depth-ratio equals to unity). We then used this ellipse as the first guess to carry out 3D nonhyperbolic moveout analysis on all traces (Vasconcelos and Tsvankin, 2006). Third, we picked the amplitude from the near-offset traces along the travelttime surface defined by the 3D nonhyperbolic moveout parameters. The amplitudes were then corrected for the geometrical spreading using MASC of Xu and Tsvankin (2006a, 2006b). Finally, we inverted the corrected amplitudes for the AVO ellipse. To evaluate the influence of the anisotropic spreading correction on the azimuthal AVO analysis, we also replaced MASC with a conventional gain correction (t^2 throughout this paper) while keeping the other processing steps unchanged.

A square in the center of the RCP survey (Figure 5.4) was chosen for carrying out the azimuthal NMO and AVO analysis. The minimum fold of CMP superbins in this study area is 1500, and the maximum 5000. In 3D azimuthal analysis, uniform azimuthal coverage is important for preventing the inversion from being distorted by the acquisition footprint. Figure 5.7 shows the azimuth and offset coverage for CMP superbins at the four corners of the study area. The coverage increases as the CMP location moves towards the center of the survey. Azimuthal coverage is acceptably uniform for offset to about 5000 feet. The predominant acquisition direction (i.e., from 40° to 120°), includes 20% extra traces. Since the extra traces along the predominant acquisition azimuth accounts for a small portion of the data, azimuthal analysis in this study is likely to be free from the acquisition footprint.

Because of the difficulty in displaying ellipses at every CMP location, we plotted instead the eccentricity and the orientation of the semi-major axis of the ellipses. We next present the results of the azimuthal NMO and AVO analysis for the top of the Mesaverde group, the top of the reservoir (UMV shale), and the bottom of the reservoir (Cameo coal).

5.4 Results of azimuthal seismic analysis

5.4.1 Mesaverde top

Parameters of AVO and NMO ellipses for the Mesaverde Top are displayed in Figure 5.8. A distinctive azimuthal AVO anomaly appears on the east side of the study area (panels a and b). The magnitude of the AVO ellipticity for this anomaly is close to unity indicating that the AVO gradient in one principal direction is twice as large as in the orthogonal direction. In contrast, the magnitude of the NMO ellipticity is close to zero, which suggests that the overburden, on the whole, is azimuthally isotropic. Also, the orientations of the principal axes of the AVO ellipses in the area of the anomaly are around $N45^\circ W$.

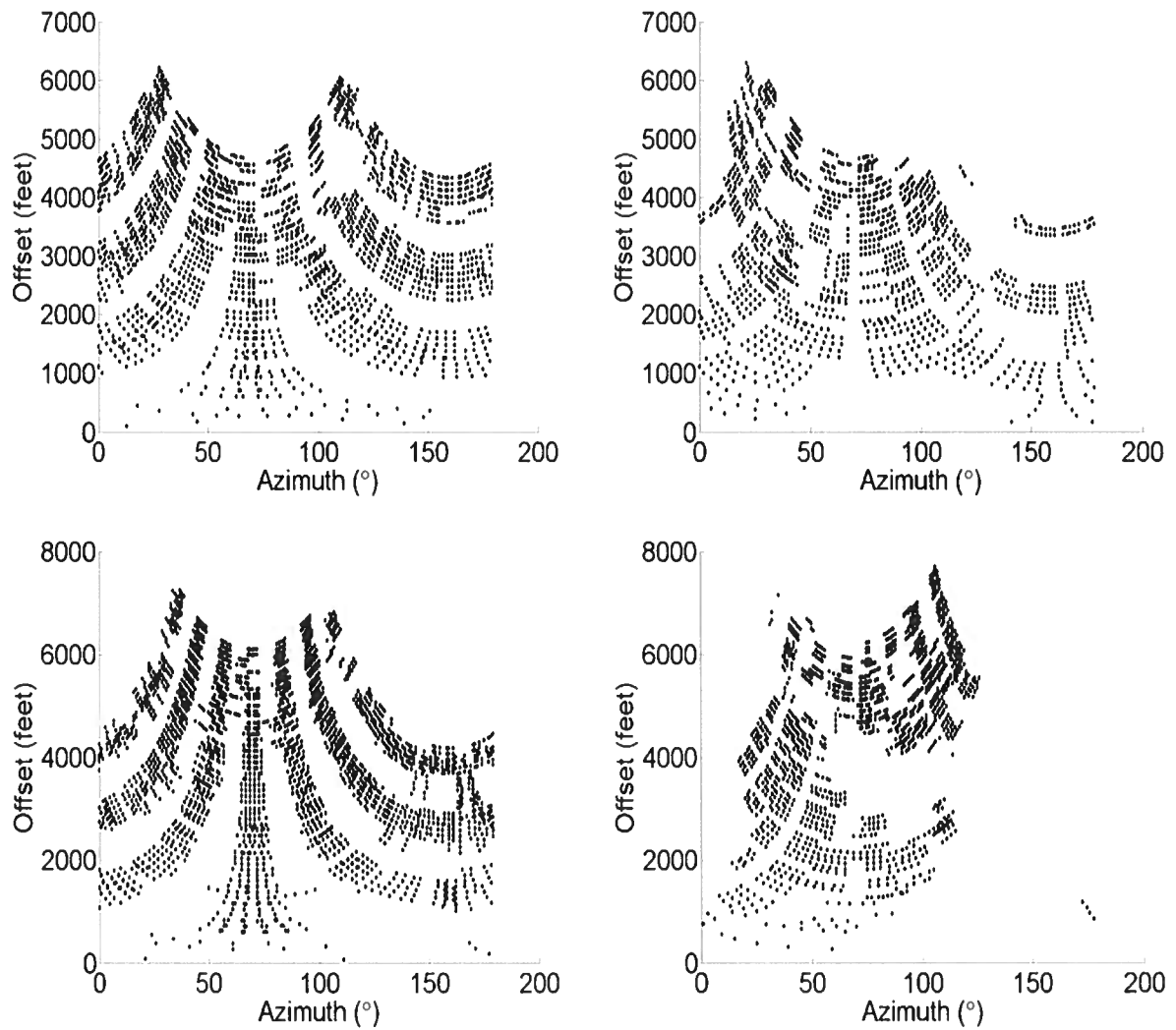


Figure 5.7. Distribution of offsets and azimuths for CMP superbins in the four corners of the study area. Note that full azimuthal coverage is achieved for offsets up to around 5000 feet.

Since the reflectivity responds to the local changes of rock properties, the azimuthal AVO anomaly in Figure 5.8 can be an indication of a fractured zone near the Mesaverde Top. The obtained AVO-gradient map offers useful information for the operating company, which is investigating candidate formations above the Mesaverde Top for storage of production water.

Although the individual anellipticity parameter η is nonnegligible (0.15 on average), its azimuthal variation is weak. Consequently, the azimuthal variation of geometrical spreading is small as well (Figure 5.9). The comparison of the first two columns of Figure 5.8 confirms that the influence of the anisotropic spreading correction on the azimuthal AVO analysis is small.

5.4.2 Top of the reservoir (UMV Shale)

Similar to the Mesaverde Top, the AVO-gradient anomaly at the top of the reservoir is located on the east edge of our study area. The magnitude of the AVO anomaly (Figure 5.10), however, increases by 30%, and compared to that of the Mesaverde Top its location is shifted to north by 200 m. If the UMV shale on top of the reservoir is VTI, the anomaly in Figure 5.10 likely marks a weak spot in the upper reservoir. The influence of the anisotropic spreading correction on the azimuthal AVO response at the top of the reservoir is marginal for the same reason as for the Mesaverde Top (Figure 5.11).

The effective NMO ellipticity for the top of the reservoir (not shown here) is slightly larger than that for the Mesaverde Top. We computed the interval NMO ellipse for the UMV Shale layer using the generalized Dix equation proposed by Grechka et al. (1999). The orientations of the interval NMO ellipses are almost random, which suggests that either the shale formation is close to VTI, or the layer-stripping operation is unstable because of the weak effective NMO ellipticity.

5.4.3 Bottom of the reservoir (Cameo Coal)

Figure 5.12 shows the azimuthal seismic attributes obtained for the bottom of the reservoir. Two significant AVO-gradient anomalies appear in the north-east and south-west quadrant of the study area (panels a and b). The magnitude of both anomalies is close to 1.5, which means that the semi-major axis of the AVO ellipse is 2.5 times that of the semi-minor axis. The principal axes of the AVO ellipse shows a rotation pattern, which seems to support the wrenching fault model for the Rulison Field, (Cumella and Ostby, 2003).

Primarily because of the large thickness of the reservoir, the interval NMO ellipses for the reservoir are somewhat constrained (the last column of Figure 5.12). The only noticeable azimuthal NMO anomaly is located in the north-east corner, near one of the azimuthal AVO anomalies. The magnitude of the NMO anomaly is about 8%, which implies that the difference between the coefficients $\delta^{(1)}$ and $\delta^{(2)}$ in the vertical symmetry planes of the model is close to 0.08.

The influence of MASC on the azimuthal AVO analysis is significant for the anomaly in the south-west quadrant of the study area (compare panels a and b of Figure 5.12).

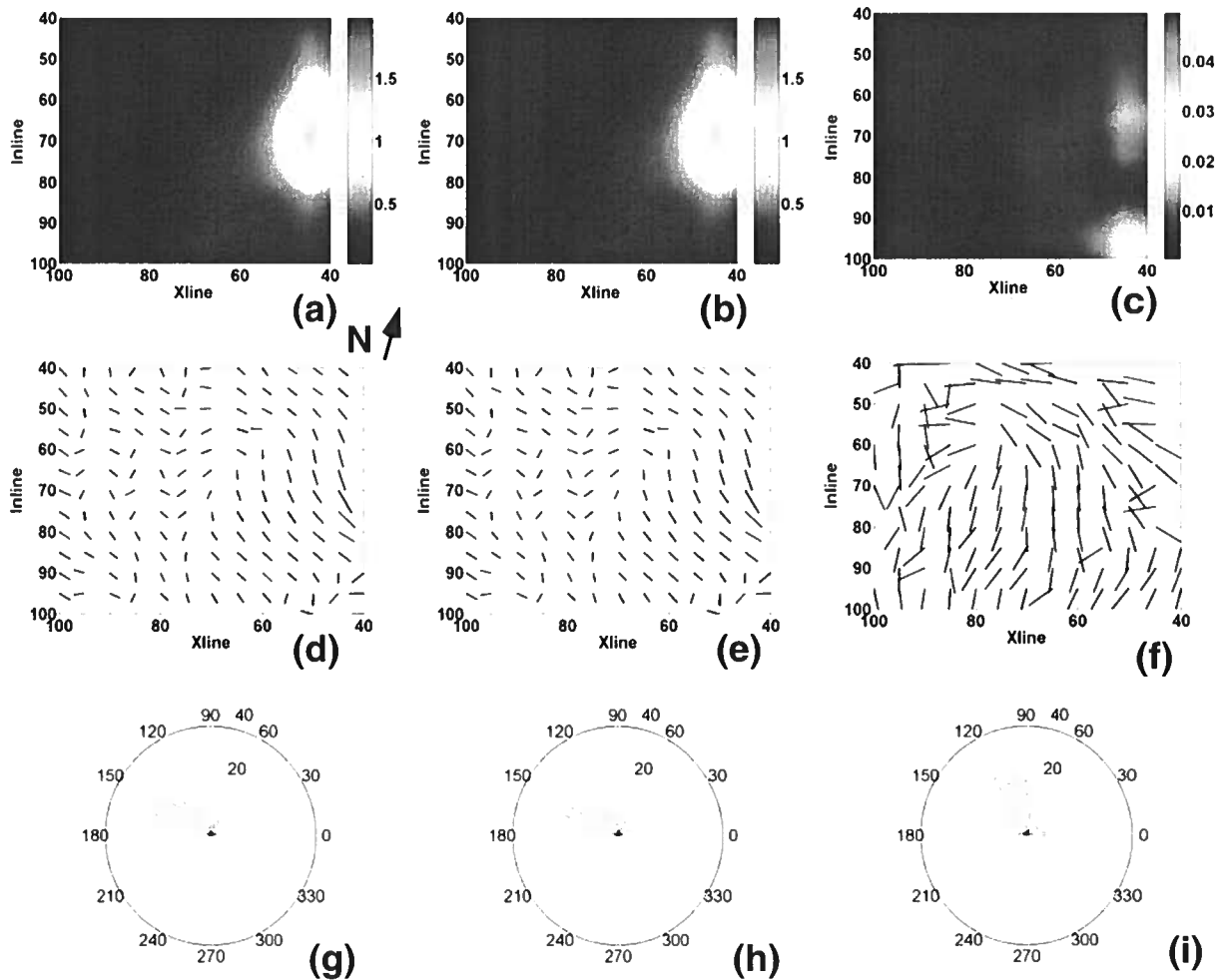


Figure 5.8. AVO and NMO ellipse information extracted for the reflection from the Mesaverde Top. The three columns correspond to the AVO ellipses computed using MASC (left), the AVO ellipses after application of the conventional gain correction t^2 (center), and the effective NMO ellipses (right). The three rows show the eccentricity of the ellipses (top), the azimuths of the major principal axis of the ellipses (middle), and the rose diagram of the orientation of the major principal axis (bottom). The eccentricity is calculated by subtracting unity from the ratio of the semi-major and semi-minor axes. The lengths of the ticks in panels d, e, and f are related to the eccentricities of the ellipses. The arrow marks the north direction, which is consistent throughout figures 5.8 to 5.13.

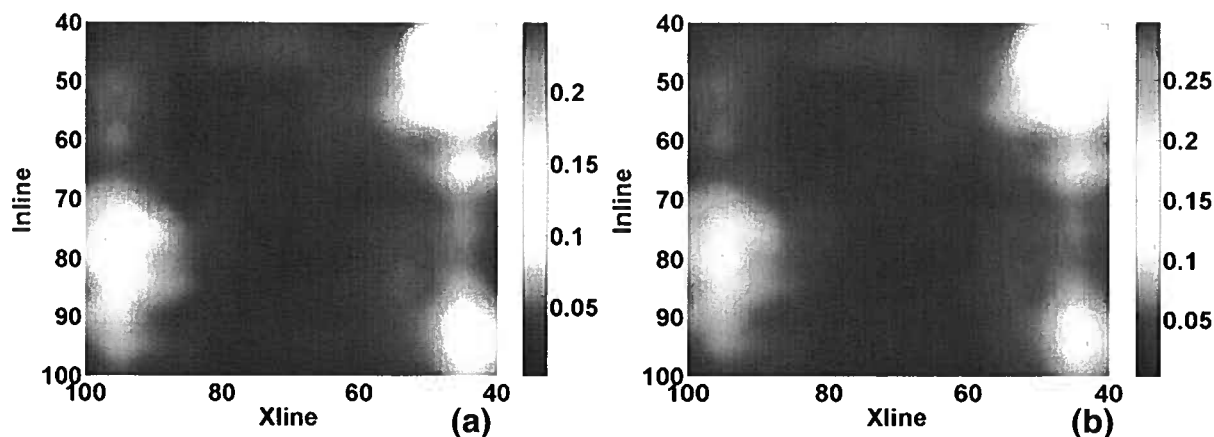


Figure 5.9. Azimuthal variation of the geometrical spreading (a) and of the parameter η (b) for the Mesaverde Top. Plot (a) shows the percentage difference between the spreading values along the semi-major and the semi-minor axes of the NMO ellipse computed for the offset-to-depth-ratio of unity. Plot (b) shows the difference between $\eta^{(1)}$ and $\eta^{(2)}$ (the anellipticity coefficients in the vertical symmetry planes).

The anomaly on MASC-corrected data is more pronounced and spatially coherent than that reconstructed by the conventional method. Because of the contribution of fractures in the thick reservoir formation, the distortion in geometrical spreading is more severe for the bottom of the reservoir (Figure 5.13) than for the top. As a result, the anisotropic spreading correction becomes important for computing an accurate AVO response from the bottom of the reservoir. Most existing azimuthal AVO case studies in the literature have been conducted for the top of the reservoir (Neves et al. 2003). Using synthetic modeling for fractured gas sands, Sayers and Rickett (1997) concluded that the bottom of the reservoir exhibits a stronger azimuthal variation of the AVO response than does the top. After the removal of the directivity factors at the source and receiver, however, the azimuthal AVO signature observed on the surface is the product of the geometrical spreading along the raypath and the reflection coefficient at the target horizon. The azimuthal variation of geometrical spreading could either strengthen or weaken the reflection coefficient. As a result, the azimuthal AVO variation for the bottom of the reservoir could be either stronger or weaker than that for the top. Thus, it is critically important to apply the anisotropic spreading correction, in particular, to the bottom of the reservoir for separation of reflection coefficients from the propagation factor. In addition, analysis of the geometrical spreading could provide supplementary information for fracture characterization. The uncertainty associated with such analysis, however, entails use with caution in practice.

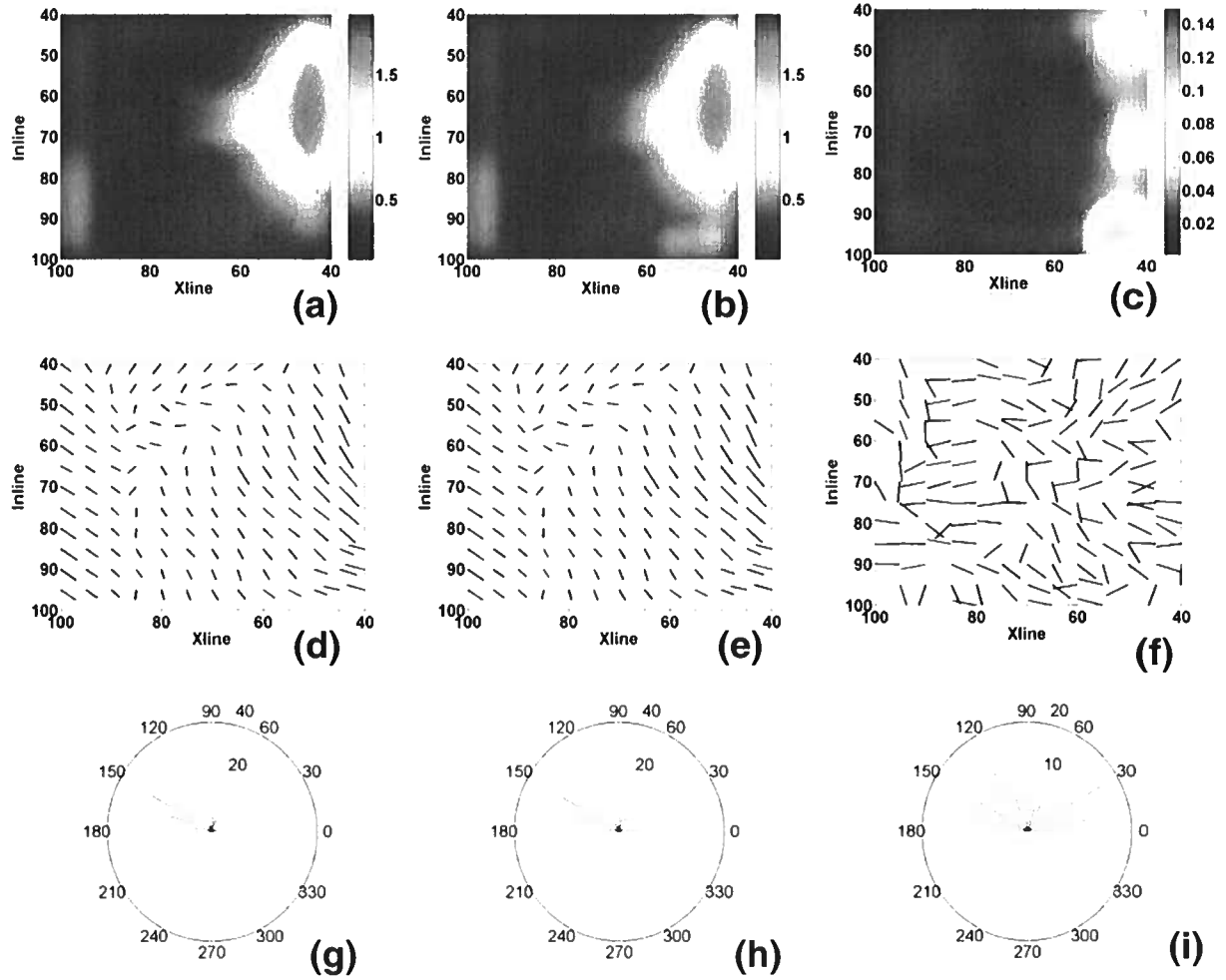


Figure 5.10. AVO and interval NMO ellipse information for the top of the reservoir (See Figure 5.8 for details).

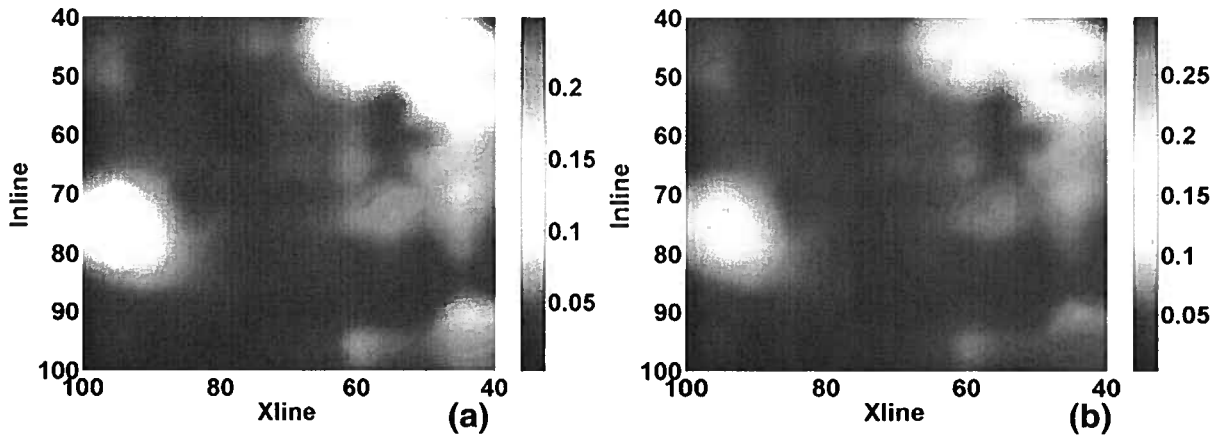


Figure 5.11. Azimuthal variation of the geometrical spreading (a) and of the parameter η (b) for the top of the reservoir (see Figure 5.9 for details).

5.5 Comparison with the fault system and EMI log

5.5.1 Fault system

Enhanced fracture zones are often associated with locations of faulting. It is, therefore, of interest to compare our fracture-characterization results with fault distribution in the Rulison field. Cumella and Ostby (2003) suggest that the fault system at the Rulison field shows a wrenching pattern. Following the wrenching fault model, Jansen (2005) interpreted the fault system using automated curvature measurements. The background image in Figure 5.14 shows his interpreted fault system at the bottom of the reservoir. The primary fault system is aligned along N70W, and a secondary step-over fault trends along N30E. Interestingly, our observed AVO-gradient anomalies (Figure 5.14a and b) are at the intersections of the two wrenching fault systems, where stress concentration is believed to induce particularly intense fracturing. Compared to the AVO anomaly observed by using conventional gain correction (Figure), the anomaly obtained by MASC in the south-west quadrant makes more geologic sense as it is closer to the intersection.

5.5.2 EMI and production logs

An electrical microimager (EMI) log is available in well RWF 542-20 near the center of our study area. Figure 5.15 compares the fracture direction obtained from EMI log and from the azimuthal AVO analysis. The predominant fracture orientation determined by the azimuthal AVO analysis differs from that interpreted by the EMI log by less than 10° . A secondary fracture set (almost perpendicular to the primary) is also observed from the AVO analysis, which does not present in the EMI log. Given that Figure 5.15c displays the results for the entire study area, the agreement between the EMI log and the azimuthal

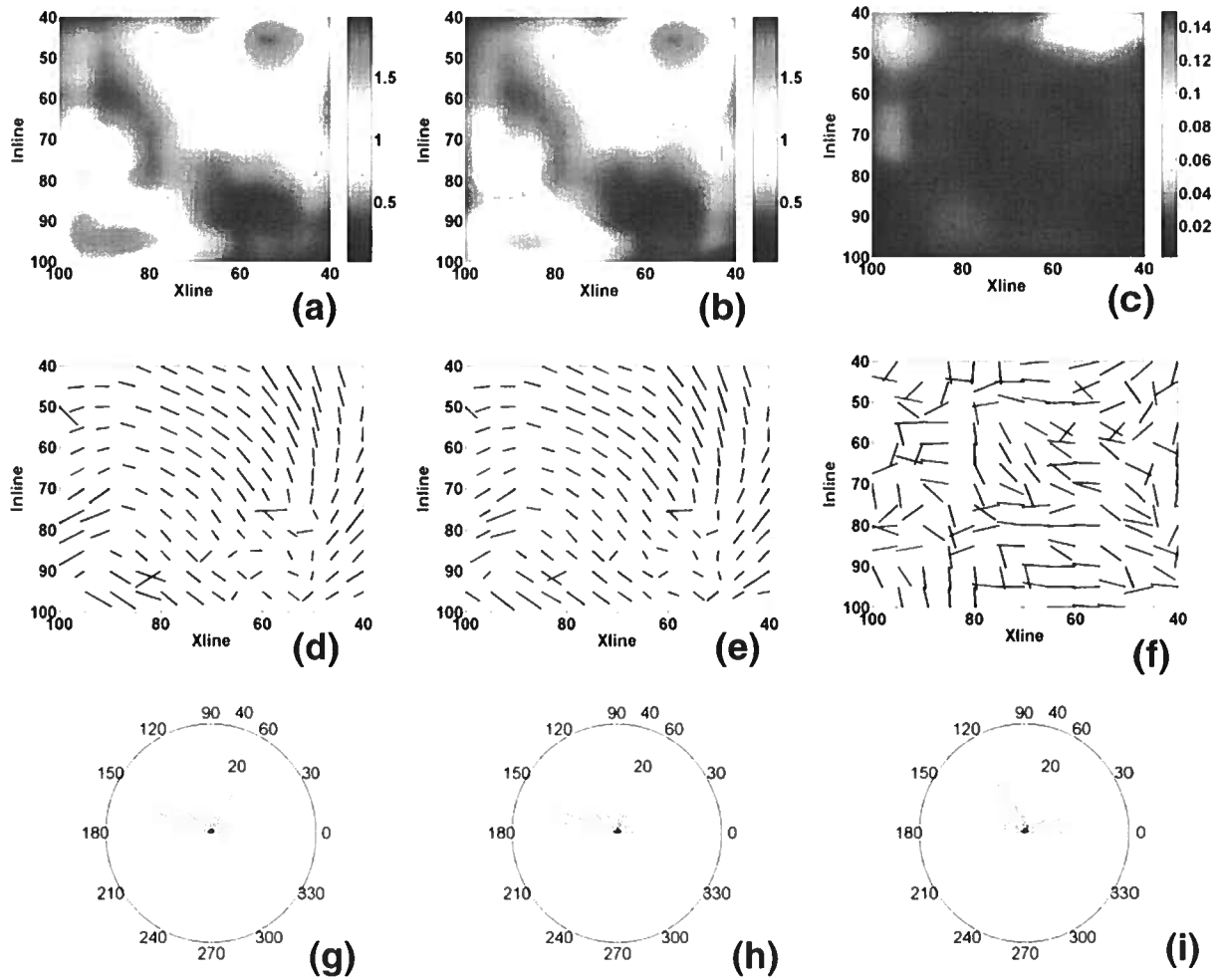


Figure 5.12. AVO ellipse information extracted for the bottom of the reservoir (Cameo Coal) and the interval NMO ellipse information for the reservoir formation (see Figure 5.8 for detailed explanation).

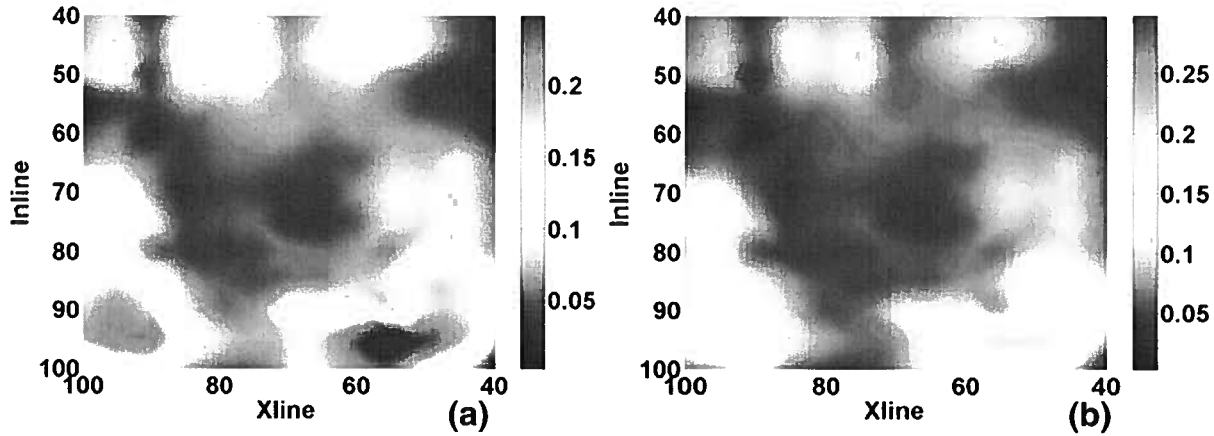


Figure 5.13. Azimuthal variation of the geometrical spreading (a) and of the parameter η (b) for the bottom of the reservoir (see Figure 5.9 for details).

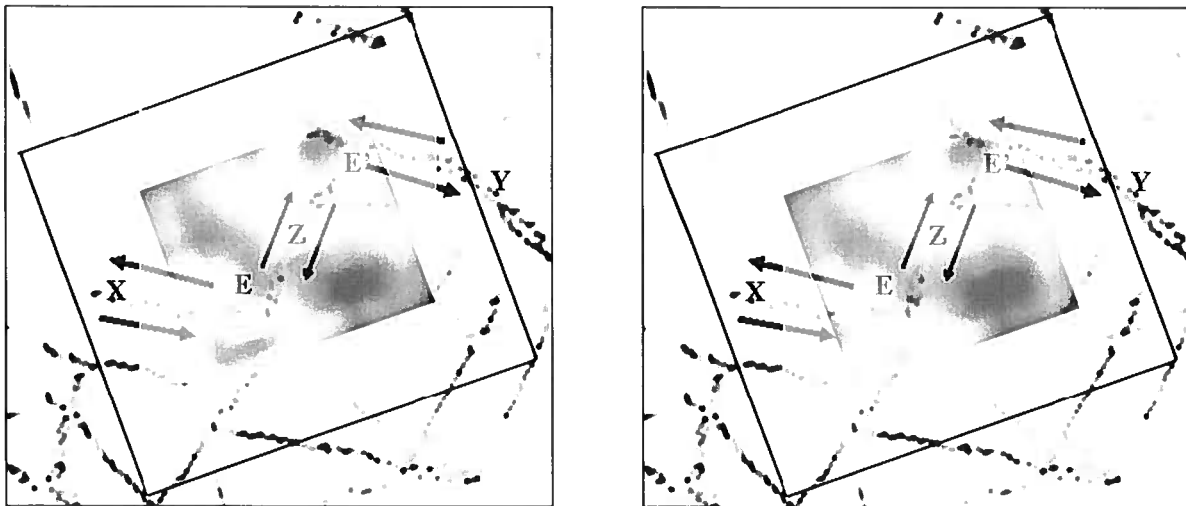


Figure 5.14. Comparison of the fault system and the azimuthal AVO attributes for the bottom of the reservoir. The fault system on both plots was interpreted by Jansen (2005) using poststack P-wave images. The azimuthal AVO attribute in plot (a) is computed using MASC (Figure 5.12a), and in plot (b) using the conventional spreading correction (Figure 5.12b). The black rectangles mark the RCP survey area, the blue lines represent faults, and the arrows indicate the directions of the slip movement. High fracture density is expected at the intersections E and E' of the two wrenching fault systems. The azimuthal AVO anomalies on plot (a) coincide with these intersections.

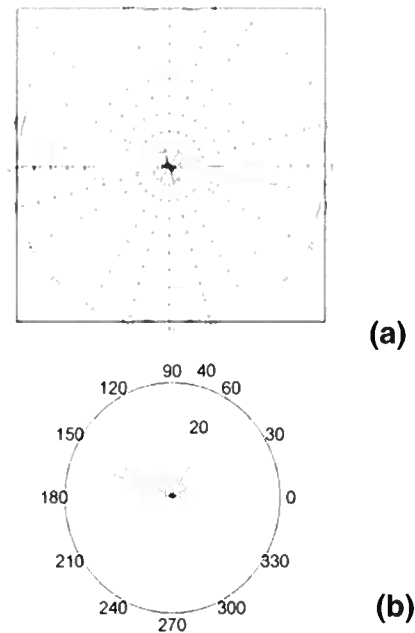


Figure 5.15. Rose diagrams of the fracture orientation. (a) Fracture directions counted in well RWF 542-20 within the reservoir; (b) directions obtained from the azimuthal AVO analysis at the bottom of the reservoir.

AVO analysis is satisfactory.

5.6 Discussion

5.6.1 Acquisition footprint

Since the acquisition design achieved full azimuthal coverage for offsets up to approximately 5000 ft, the NMO and AVO ellipses at the Mesaverde Top and the top of the reservoir (UMV Shale) are not distorted by the acquisition footprint. The azimuth and offset coverage in the four corners of our study area suggests that the orientation of the NMO and AVO ellipses for the bottom of the reservoir might be biased towards the dominant acquisition azimuth from 40° to 100° (Figure 5.7). No evident bias is observed, however, in the azimuths of the AVO and NMO ellipses (Figure 5.12d, e, and f). In particular, the azimuths of the AVO ellipses are random in the lower right corner of the study area where the AVO eccentricities are close to zero (Figure 5.12d and e). The absence of the acquisition footprint can be explained by the orthogonality of the acquisition layout, which ensures that 80% of all traces fall into offsets for which full-azimuth coverage is achieved.

5.6.2 Error analysis

Considering that the uncertainty in traveltime picking does not exceed 8ms, Vasconcelos and Grechka (2006) estimated that the variance in the NMO velocities is close to 7%. The most serious problem in the estimation of the NMO ellipses, however, is the bias observed for different superbin sizes. The NMO ellipticity systematically increases over the area when the superbin size changes from 5x5 to 9x9. The larger bin size can cause distortions that can be attributed to the influence of lateral heterogeneity, which may result in a higher NMO ellipticity and lower semblance values. On average, the effective NMO ellipticity for the top of the reservoir increased by 0.04 and the semblance value decreased from around 0.6 for 5x5 superbin size to 0.45 for 9x9 bin size. The considerable decrease in semblance value by 9x9 bin size suggests the influence of lateral heterogeneity. The 9x9 bin size, therefore, yields less reliable seismic attributes than does the 5x5 bin size.

For all the reflectors, the confidence interval of the AVO eccentricity can be assessed from the azimuths of the AVO ellipses (Figure 5.8d, Figure 5.10d, and Figure 5.12d). When the AVO eccentricities are smaller than 0.3, the azimuths of the AVO ellipses are random (that is particularly obvious in the upper left quarter of Figure 5.10d and lower right quarter of Figure 5.12d). Once the AVO eccentricity becomes larger than about 0.3, the azimuths of the AVO ellipses show regular pattern.

Because of the small offset-to-depth-ratio for the bottom of the reservoir (close to unity at the edges and 1.6 in the center of the study area), the estimated anellipticity parameters $\eta^{(1)}$, $\eta^{(2)}$, and $\eta^{(3)}$ might contain large errors. The performance of MASC, however, is insensitive to trade-offs between the moveout parameters as long as they give an accurate approximation for the traveltime surface (Xu and Tsvankin, 2006a). The quality of the approximation provided by our moveout-inversion algorithm is confirmed by relatively high semblance values (0.7 on average) achieved by the nonhyperbolic-moveout equation.

5.6.3 Correlation between the NMO and AVO ellipses

It has been suggested in the literature to combine the NMO ellipse with the azimuthally-varying AVO gradient to constrain the anisotropy parameters and invert for some physical fracture parameters (Rüger and Tsvankin, 1997; Bakulin et al. 2000a). This approach is feasible when the reservoir is thick enough for reliable estimation of the interval NMO ellipses but does not have pronounced vertical heterogeneity. Because the vertical resolution of AVO analysis is much higher than that of NMO velocity and the large thickness of the reservoir in Rulison field, no strong correlation exists between the azimuthal NMO and AVO attributes. Still, when combined together they complement each other for better understanding of the fracture system.

5.6.4 Group angle versus phase angle

The AVO gradient is extracted here using the source-receiver offset rather than the incidental phase angle. This crude treatment can result in nonnegligible errors in quantitative AVO inversion. Unfortunately, the phase angle cannot be accurately calculated

without knowledge of the anisotropy parameters in the overburden. It would be worthwhile to carry out a modeling study to investigate errors in azimuthal AVO attributes caused by inaccuracy in the phase angle.

5.7 Conclusions

The influence of the anisotropic spreading correction on the azimuthal AVO response should be taken into account for the bottom of the reservoir where the azimuthal distortion of the geometrical spreading is significant. The azimuthal AVO anomaly computed after application of MASC in the south-west quadrant of the study area is more pronounced and spatially coherent than is that obtained by the conventional t^2 correction. Therefore, it is essential to apply MASC to ensure reliable recovery of the azimuthal AVO attributes. Note that the implementation of MASC following the azimuthal moveout analysis involves no extra cost.

The AVO-gradient anomalies at the bottom of the reservoir coincide with the intersections of the two wrenching fault systems, which suggests that the anomalies indeed indicate weak spots of high fracture density. While the fracture orientation varies in space, the dominant fracture azimuth is N70W (Figure 5.15), which is in good agreement with the EMI logs. The weak NMO ellipticity for the interval between the Mesaverde Top and the top of the reservoir (dominated by shale) suggests that this interval is azimuthally isotropic. Thus, the AVO anomalies at the top of the reservoir and at the Mesaverde Top are likely caused by enhanced fractured zones in the upper reservoir and in the formation immediately above the Mesaverde Top, respectively.

The magnitude of the azimuthal AVO ellipticity is significantly higher than that of the NMO ellipticity in the Rulison field. Also, no strong correlation is observed between the azimuthal AVO and NMO attributes, which may be explained by the inherent difference between these two measurements. AVO response depends on the local changes in rock properties; NMO velocities, on the other hand, reflect the average rock properties over coarse intervals. Since the reservoir interval in the Rulison field is 2000ft thick, the map of the azimuthal NMO ellipse suggests the distribution of relative fracture density averaged over this large reservoir column. The azimuthal AVO maps, however, show the fracture distribution near the Mesaverde Top and the top and the bottom of the reservoir.

5.8 References

- Bakulin, A., V. Grechka, and I. Tsvankin, 2000, Estimation of fracture parameters from reflection seismic data – Part I: HTI model due to a single fracture set: *Geophysics*, **65**, 1788–1802.
- Bakulin, A., V. Grechka, and I. Tsvankin, 2000, Estimation of fracture parameters from reflection seismic data – Part II: Fractured models with orthorhombic symmetry: *Geophysics*, **65**, 1803–1817.

- Cumella, S. P., and D. B. Ostby, 2003, Geology of the basin-centered gas accumulation, Piceance Basin, Colorado. Piceance Basin 2003 Guidebook: Rocky Mountain Association of Geologists, 171–193.
- Grechka, V., and I. Tsvankin, 1998, 3-D description of normal moveout in anisotropic inhomogeneous media: *Geophysics*, **63**, 1079–1092.
- Grechka, V., and I. Tsvankin, 1999, 3-D moveout inversion in azimuthally anisotropic media with lateral velocity variation: Theory and a case study: *Geophysics*, **64**, 1202–1218.
- Grechka, V., I. Tsvankin, and J. D. Cohen, 1999, Generalized Dix equation and analytic treatment of normal-moveout velocity for anisotropic media: *Geophysical Prospecting*, **47**, 117–148.
- Jansen, K., 2005, Seismic investigation of wrench faulting and fracturing at Rulison field, Colorado: M.S. thesis, Colorado School of Mines.
- Li, X., Y. Liu, E. Liu, F. Shen, L. Qi, and S. Qu, 2003, Fracture detection using land 3D seismic data from the Yellow River delta, China: *The Leading Edge*, 680–683.
- Neves, F. A., A. Al-Marzoug, J. J. Kim, and E. L. Nebrija, 2003, Fracture characterization of deep tight sands using azimuthal velocity and AVO seismic data in Saudi Arabia: *The Leading Edge*, 469–475.
- Perez, M. A., V. Grechka, and Michelena, R. J., 1999, Fracture detection in a carbonate reservoir using a variety of seismic methods: *Geophysics*, **64**, 1266–1276.
- Rüger, A., 2001, Reflection coefficients and azimuthal AVO analysis in anisotropic media: *Society of Exploration Geophysics*.
- Rüger, A., and Tsvankin, I., 1997, Using AVO for fracture detection: Analytic basis and practical solutions: *The Leading Edge*, **16**, 1429–1434.
- Sayers, C. M., and J. E. Rickett, 1997, Azimuthal variation in AVO response for fractured gas sands: *Geophysical Prospecting*, **45**, 165–182.
- Tsvankin, I., 2005, *Seismic signatures and analysis of reflection data in anisotropic media*: Elsevier Science Publ. Co., Inc. (second edition).
- Vasconcelos, I., and I. Tsvankin, 2006, Non-hyperbolic moveout inversion of wide-azimuth P-wave data for orthorhombic media: *Geophysical Prospecting*, **54**, 535–552.
- Vasconcelos, I., and V. Grechka, 2006, Seismic characterization of multiple fracture sets from multicomponent, multiazimuth, 3D data: Rulison Field, CO: CWP Project Review.
- Xu, X., I. Tsvankin, and A. Pech, 2005, Geometrical spreading of P-waves in horizontally layered, azimuthally anisotropic media: *Geophysics*, **70**, D43–D53.

Xu, X., and I. Tsvankin, 2006a, Anisotropic geometrical-spreading correction for wide-azimuth P-wave reflections: *Geophysics*, **71**, D161–D170.

Xu, X., and I. Tsvankin, 2006b, Azimuthal AVO analysis with anisotropic spreading correction: A synthetic study: *The Leading Edge*, (to appear in November issue).

Chapter 6

Anisotropic geometrical-spreading correction in the presence of lateral heterogeneity

6.1 Introduction

Compensation for geometrical spreading is an essential step in AVO (amplitude-variation-with-offset) analysis of reflection data, in particular when the overburden is anisotropic. Xu et al (2005) and Xu and Tsvankin (2006) presented an efficient method (MASC, or moveout-based anisotropic spreading correction) to correct long-offset, wide-azimuth data for geometrical spreading in laterally homogeneous (e.g., horizontally layered), azimuthally anisotropic media. The geometrical-spreading factor is expressed in terms of reflection traveltime described by a nonhyperbolic moveout equation that has the same form as that in VTI (transversely isotropic with a vertical symmetry axis) media.

The underlying assumption of MASC is that the medium is laterally homogeneous, although it can be arbitrarily anisotropic. In practice, however, the subsurface structure is often more complicated. In that case, compensation for geometrical spreading is not straightforward. Tygel et al. (1992) proposed a method to correct geometric spreading in laterally heterogeneous media. Their approach, however, involves complicated manipulations with various recording geometries and suffers from instability.

Here, we use numerical modeling to study the applicability of the MASC method to models with mild reflector dip and moderate lateral velocity gradient. A series of numerical tests is performed for reflections from a dipping interface overlaid by a stack of horizontal layers. Here, we show the results for three models: a layered isotropic medium above a dipping interface, a dipping orthorhombic model, and an isotropic layer with moderate quadratic lateral velocity variation.

6.2 Numerical tests

6.2.1 Layered isotropic model

Table 1 lists the parameters of a layered isotropic medium. The dip of the reflecting interface is 20° , while the layers in the overburden are horizontal. Although MASC makes the assumption that the subsurface is horizontal, we apply it to compute the geometrical spreading for this model (Figure 1). For a wide range of offsets and azimuths, the errors of MASC are less than 6%.

	V_{P0} (km/s)	Thickness (km)	Dip
Layer 1	1.50	0.3	0°
Layer 2	1.74	0.2	0°
Layer 3	1.94	0.2	0°
Layer 4	2.15	0.3	20°

Table 6.1. Parameters of the four-layer isotropic medium used in the numerical test. The target event is the reflection from the dipping interface.

	Symmetry type	V_{P0} (km/s)	Thickness (km)	$V_{nmo}^{(1)}$ (km/s)	$V_{nmo}^{(2)}$ (km/s)	$\eta^{(1)}$	$\eta^{(2)}$	$\eta^{(3)}$	Dip
L 1	ISO	1.5	0.2	1.5	1.5	0	0	0	0°
L 2	ORTH	2.44	0.9	2.63	2.24	0.21	0.40	0.19	0°
L 3	ORTH	3.0	0.9	3.15	2.68	0.18	0.31	-0.06	20°

Table 6.2. Parameters of a three-layer model that includes two orthorhombic layers with aligned vertical symmetry planes $\phi = 0^\circ$ and $\phi = 90^\circ$. The geometrical spreading is computed for the reflection from the dipping interface.

Reflection traveltimes in the dip direction in CMP geometry from a dipping interface in an isotropic homogeneous medium are equal to those from a horizontal interface with velocity and depth divided by a cosine of the dip angle (Levin, 1971). Since a plane interface does not change the curvature of reflection wavefront, geometrical spreading in isotropic homogeneous media with plane interfaces equals to the distance from a source to a receiver regardless of the dip of the reflector. The MASC method does not recognize the dip of the reflector and treats the reflection traveltimes as if they are from an equivalent horizontal interface. The geometrical spreading (i.e., the distance from the source to the receiver) obtained by MASC, therefore, is large by a factor of cosine of the dip angle. This exact relationship is confirmed by ray tracing. Thus, the error in geometrical spreading computed by MASC for a 20° dipping layer is close to 6% in along the dip direction, and decreases towards the strike azimuth. Numerical test in layered isotropic models shows similar errors (Figure 1), albeit not in an exact sense. Apparently, the error of MASC increases with the dip of a dipping reflector.

6.2.2 Dipping orthorhombic layer

I performed a similar comparison for a layered orthorhombic medium with strong azimuthal anisotropy (Table 2). The errors of MASC for this model are comparable to those for the isotropic model.

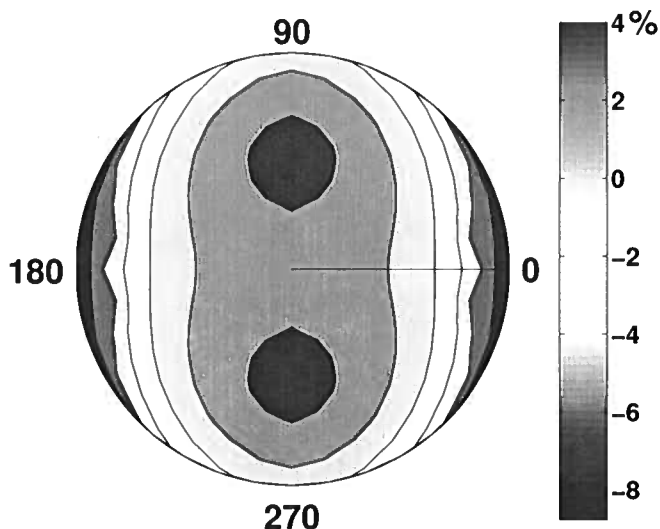


Figure 6.1. Accuracy of MASC in computing full-azimuth, long-offset P-wave geometrical spreading in a layered isotropic medium. The error is normalized by the geometrical spreading obtained by dynamic ray tracing. The maximum offset-to-depth-ratio is two.

6.2.3 Isotropic layer with quadratic lateral velocity variation

Introduction of a constant lateral velocity gradient into a homogeneous isotropic layer does not influence the reflection traveltimes in CMP geometry. Likewise, the geometrical spreading remains unchanged for every source-receiver pair in a CMP gather. We, therefore, test a model with a moderate quadratic velocity gradient (Figure 3). The geometrical spreading computed from MASC is displayed in Figure 4. Even though the accuracy of MASC decreases with offset, the error is less than 10% if the offset-to-depth-ratio is limited by two.

6.3 Conclusions

We performed numerical tests for reflections from a dipping interface overlaid by a stack of horizontal layers with azimuthal anisotropy. If the dip is smaller than 20° , the error of the MASC method does not exceed 10% for the full range of source-receiver azimuths and offsets up to twice reflector depth. Also, the method remains accurate for layer-cake models with constant lateral velocity gradient, and is weakly sensitive to moderate nonlinear lateral velocity variation.

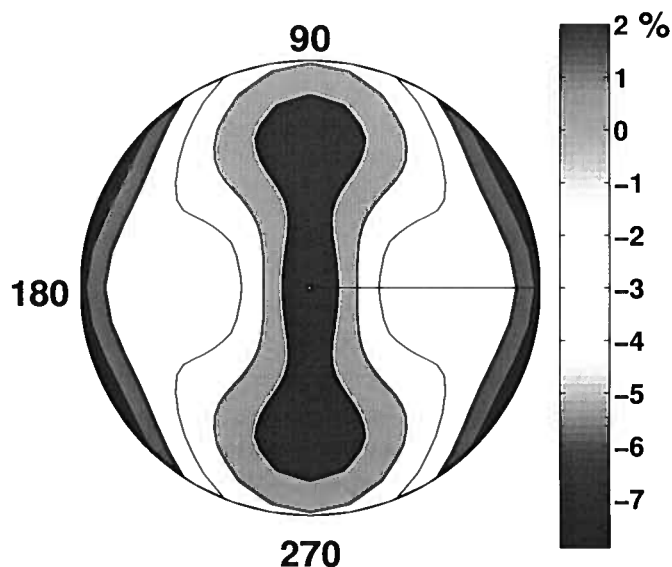


Figure 6.2. Accuracy of MASC in computing full-azimuth, long-offset P-wave geometrical spreading in a layered orthorhombic medium. The error is normalized by the geometrical spreading obtained by anisotropic dynamic ray tracing. The maximum offset-to-depth-ratio is two.

CMP		
↓		
—————		
1.6	2.0	3.2
km s⁻¹	km s⁻¹	km s⁻¹
0.0 s⁻¹	0.4 s⁻¹	1.6 s⁻¹
—————		

Figure 6.3. Parameters of a horizontal isotropic layer with quadratic lateral velocity variation. The arrow marks the common-midpoint (CMP). The velocity and the lateral velocity gradient are marked at three lateral positions (one km to the left of the CMP, at the CMP, one km to the right of the CMP). The thickness of the layer is 1 km.

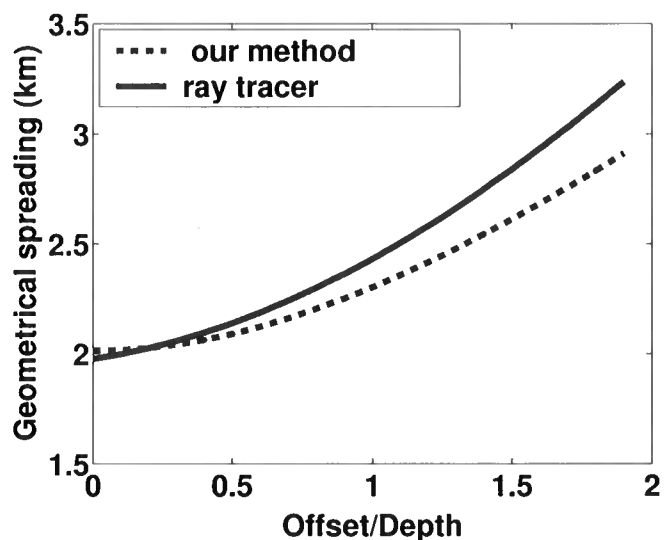


Figure 6.4. Accuracy of MASC in computing P-wave geometrical spreading for the isotropic laterally heterogeneous layer from Figure 3.

6.4 References

- Levin, F.K., 1971, Apparent velocity from dipping interface reflections: *Geophysics*, **36**, 510–516.
- Tygel, M., J. Schleicher, and P. Hubral, 1992, Geometrical spreading corrections of offset reflections in a laterally inhomogeneous earth: *Geophysics*, **57**, 1054–1063.
- Xu, X., I. Tsvankin, and A. Pech, 2005, Geometrical spreading of P-waves in horizontally layered, azimuthally anisotropic media: *Geophysics*, **70**, D43–D53.
- Xu, X., and I. Tsvankin, 2006, Anisotropic geometrical-spreading correction for wide-azimuth P-wave reflections: *Geophysics*, **71**, D161–D170.

Chapter 7

MASC for Converted PS-Waves

7.1 Introduction

Amplitude-variation-with-offset (AVO) analysis of mode-converted PS-waves can be used in combination with P-wave AVO to constrain anisotropy parameters and properties of fracture networks. For example, it is shown in Bakulin et al. (2000) that the azimuthally-varying AVO gradients of PP- and PS-waves uniquely define the normal and tangential compliances of a single set of penny-shaped cracks in an isotropic background. These compliances can be directly related to the fracture density and fluid infill. A more general methodology for joint inversion of PP and PS AVO gradients in azimuthally anisotropic media was developed by Jilek (2002). The advantage of combining PS and PP AVO is that they are determined by rock properties on the same scale.

The high sensitivity of shear-wave amplitudes to the presence of anisotropy makes it imperative to correct PS-wave amplitudes for geometrical spreading prior to AVO inversion. As shown by Tsvankin (1995, 2005) and Xu et al. (2005), the anisotropy parameters η and σ are primarily responsible for distortions of geometrical spreading of P- and SV-waves, respectively. Since σ is often much larger than η because of the contribution of the squared vertical-velocity ratio, the geometrical spreading of SV-waves is more distorted by the presence of anisotropy than is that of P-waves.

To correct AVO signatures for the influence of anisotropic overburden, it is convenient to represent geometrical spreading through reflection traveltimes measured on the earth's surface. Following paraxial ray theory (Červený, 2001), Xu et al. (2005) obtained a concise equation for geometrical spreading of pure wave modes in laterally homogeneous, arbitrarily anisotropic media. By employing a 3D extension of the Alkhalifah-Tsvankin (1995) equation, Xu and Tsvankin (2006a) developed a practical and robust algorithm ("MASC") to correct for geometrical spreading in azimuthally anisotropic media. The accuracy of MASC was confirmed by ray tracing and full-wavefield synthetic studies. Also, Xu and Tsvankin (2006b) showed that MASC cannot always be replaced by conventional gain corrections even for purposes of qualitative AVO analysis.

Here, we extend the methodology of MASC to converted PS-waves in anisotropic media. We first show that despite the asymmetry of the raypath for PS-waves, the geometrical-spreading equation remains the same as that for pure waves. By using both the Tsvankin-Thomsen (1994) and the Alkhalifah-Tsvankin (1995) equations, we extend the MASC algorithm to PSV data acquired in vertical symmetry planes of horizontally layered anisotropic media. Finally, in a full-wavefield synthetic study, we evaluated the accuracy of MASC

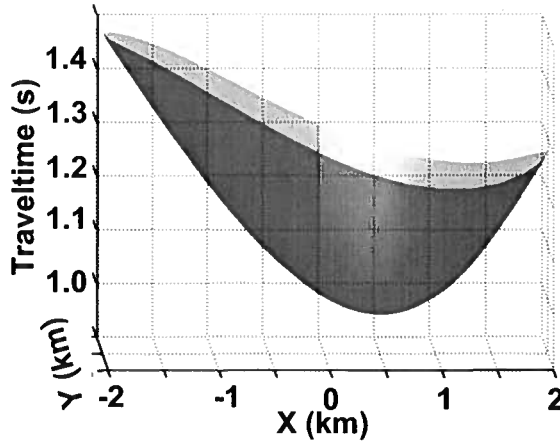


Figure 7.1. Traveltime surface of the fast PS-wave computed for a TTI layer in CMP geometry. Note that the global minimum is not located at zero offset because of the absence of a horizontal symmetry plane. Moreover, the surface is asymmetric with respect to the global minimum. The model parameters are $V_{P0} = 2.6$ km/s, $V_{S0} = 1.38$ km/s, $\epsilon = 0.46$, $\delta = 0.11$, $\gamma = 0.0$, $\nu = 70^\circ$. The thickness of the TTI layer is one kilometer.

for PS-waves and to compare its performance with that of conventional gain corrections routinely used in practice.

7.2 Moveout-based expression for geometrical spreading of PS-waves

The most prominent feature of PS-converted waves as opposed to PP-waves is the asymmetry of the raypath and, consequently, of traveltime and amplitude on common-midpoint (CMP) gathers (Thomsen, 1999). This asymmetry leads to a change in traveltime when the source and receiver are interchanged in a medium with either lateral heterogeneity or anisotropy without a horizontal symmetry plane (Dewangan, 2004). Thus, the key geometrical-spreading equation (reproduced below in equation 7.2) of Xu and Tsvankin (2005) for pure wave modes has to be revisited for converted PS-waves.

While a slight modification of the derivation is needed, equation 7.2 remains valid for converted PS-waves. Appendix A of Xu et al. (2005) contains a derivation of equation 7.2 using an important result of paraxial ray theory. The central step of the derivation was to reduce the number of independent variables of the traveltime function from four to two (i.e., offsets and azimuths) in laterally homogeneous, arbitrarily anisotropic media. For pure waves, the independent variable azimuth ranges only from 0° to 180° because a traveltime remains the same when the source and the receiver are interchanged. For converted waves, however, it is necessary for the azimuth to cover the entire 360° range to account for possible asymmetry of traveltimes when exchanging source and receiver locations. Therefore, A-3

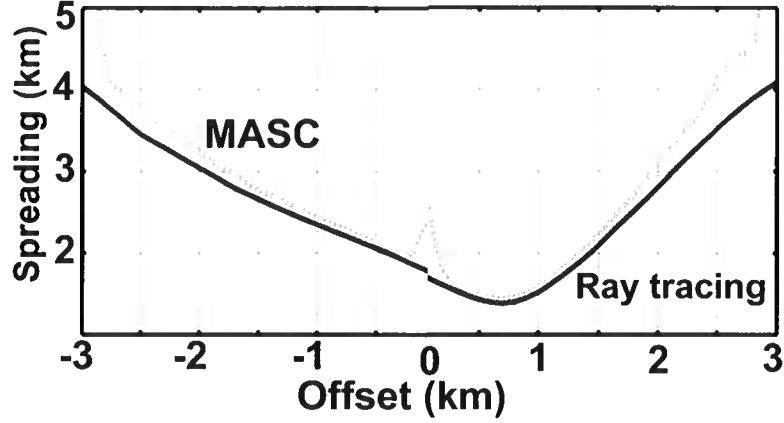


Figure 7.2. Comparison of geometrical spreading computed from equation 2 (dashed line) and by ray tracing (solid) in the symmetry-axis plane of the model in Figure 1. The “jitters” are caused by errors in approximating the traveltime surface shown in Figure 7.1. The arbitrary choice of the second-order derivatives at offsets of ± 3 km and zero-offset results in discrepancies between our method and ray tracing at these locations. On the whole, however, the spreading computed by our method agrees well that obtained by ray tracing.

of Xu et al. (2005) for converted waves changes to

$$\alpha = \begin{cases} \tan^{-1} \left[\frac{x_2^r - x_2^s}{x_1^r - x_1^s} \right] & x_1^r - x_1^s > 0 \\ \tan^{-1} \left[\frac{x_2^r - x_2^s}{x_1^r - x_1^s} \right] + \pi & x_1^r - x_1^s < 0 \end{cases} . \quad (7.1)$$

Here $x_{1,2}^s$ are the coordinates of the source location, and $x_{1,2}^r$ the coordinates of the receiver location (again, we assume a horizontal observation surface). Since a constant, π , does not change the derivatives, the final equation of geometrical spreading as a function of traveltime remains unchanged for converted-PS waves:

$$L(x, \alpha) = (\cos \phi^s \cos \phi^r)^{1/2} \left[\frac{\partial^2 T}{\partial x^2} \frac{\partial T}{\partial x} \frac{1}{x} + \frac{\partial^2 T}{\partial x^2} \frac{\partial^2 T}{\partial \alpha^2} \frac{1}{x^2} - \left(\frac{\partial T}{\partial \alpha} \right)^2 \frac{1}{x^4} \right]^{-1/2}, \quad (7.2)$$

where x is the source-receiver offset, and α is the azimuth of the source-receiver line. Equation 7.2, therefore, is valid for any wave mode in laterally homogeneous, arbitrarily anisotropic media.

Next, we test the validity of equation 7.2 in a transversely isotropic layer with a tilted symmetry axis (TTI, the physical model of Dewangan et al, 2006). The traveltime

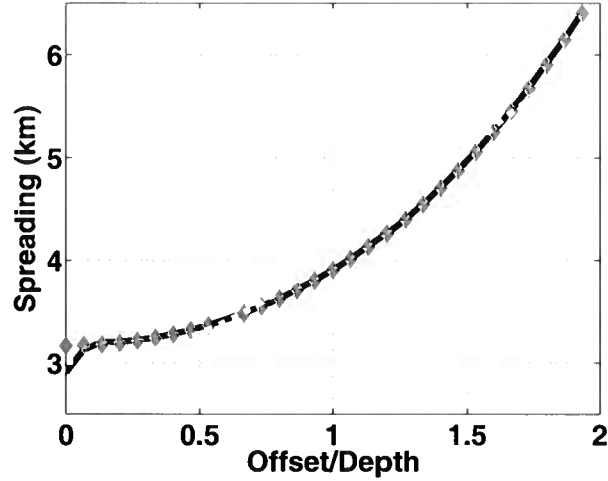


Figure 7.3. Geometrical spreading computed by our method and by ray tracing for model 1. The diamonds correspond to the output of our method with Tsvankin-Thomsen equation; the dashed curve is computed by our method using Alkhalifah-Tsvankin equation; the solid line marks the result of ray tracing.

surface of the fast PS-wave is computed by anisotropic ray tracing for a CMP gather. In the symmetry-axis plane, the fast S-wave has in-plane polarization (i.e., it is an SV wave) since the anisotropy parameter σ is positive and γ is set to zero. As illustrated in Figure 7.1, the traveltimes surface is asymmetric with respect to the location of the global traveltimes minimum, which also deviates from the common midpoint. Since it is difficult to fit the asymmetric traveltimes surface using a Taylor series, we employed a cubic-spline function instead. Combining equation 7.2 and the spline function, we computed the geometrical spreading for the converted PSV-wave in the vertical symmetry-axis plane. The geometrical spreading computed from equation 7.2 is close to that obtained by ray tracing (Figure 7.2), which confirms the validity of that equation for converted PS-waves in media without a horizontal symmetry plane. While equation 7.2 is valid for laterally homogeneous, arbitrarily anisotropic media, in the rest of this paper, we focus on media with a horizontal symmetry plane (i.e. the moveout of PS-waves is symmetric).

7.3 Algorithm for moveout-based anisotropic spreading correction

Because of the difficulty in exciting shear waves on land and the absence of shear-wave source in marine settings, PS-waves are often used to infer shear-wave information about the subsurface. Outside symmetry planes of anisotropic media, an incident P-wave excites two split shear waves which have to be separated using rotation analysis. In contrast, a P-wave generates only SV-waves in vertical symmetry planes, which facilitates AVO analysis for PSV-waves in these planes. The focus of this section, therefore, is on extending the

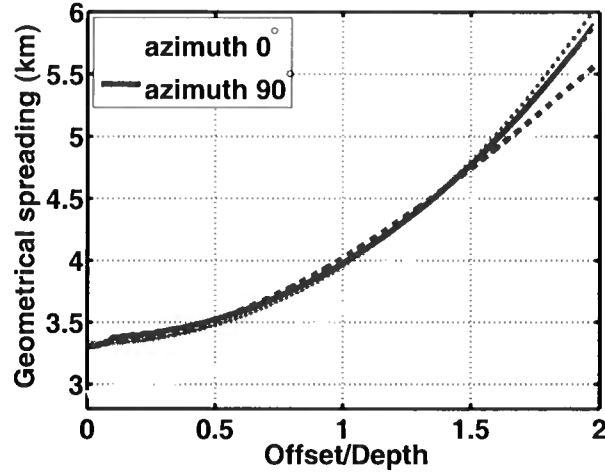


Figure 7.4. Geometrical spreading computed by our method and by ray tracing for two vertical symmetry planes of the orthorhombic model (model 2 from Table 2). The asterisks correspond to spreading computed by our method using the 3D version of the Tsvankin-Thomsen equation; the dash curves are results from our method with application of the 3D version of the Alkhalifah-Tsvankin equation; the solid lines mark the results of ray tracing.

algorithm of MASC (Xu and Tsvankin, 2006a) to PSV modes in vertical symmetry planes of horizontally layered anisotropic media.

As for P-waves, the key issue in implementing equation 7.2 for converted waves is to find a smooth approximation for traveltimes that can be used for a wide range of offsets and azimuths. To describe long-spread reflections for P-waves, Tsvankin and Thomsen (1994) developed the following nonhyperbolic moveout equation:

$$T^2(x) = T_0 + A_2 x^2 + \frac{A_4 x^4}{1 + A x^2}, \quad (7.3)$$

where T_0 is the zero-offset traveltime, A_2 is related to the normal-moveout velocity as $A_2 = V_{\text{nmo}}^{-2}$, and A_4 is the quartic coefficient responsible for nonhyperbolic moveout. The parameter A in the denominator depends on the horizontal group velocity V_{hor} and is designed to make $T(x)$ convergent at large offsets $x \rightarrow \infty$.

The generic Tsvankin-Thomsen equation 7.3 also proves to be accurate for PS traveltimes in horizontally-layered VTI media (Tsvankin, 2005). By accounting for the azimuthal variation in the moveout coefficients, Al-Dajani et al. (1998) extended the general Tsvankin-Thomsen equation to P-waves in azimuthally anisotropic media:

$$T^2(x, \alpha) = A_0 + A_2(\alpha) x^2 + \frac{A_4(\alpha) x^4}{1 + A(\alpha) x^2}, \quad (7.4)$$

$$A_2(\alpha) = A_2^{(1)} \sin^2 \alpha + A_2^{(2)} \cos^2 \alpha, \quad (7.5)$$

$$A_4(\alpha) = A_4^{(1)} \sin^4 \alpha + A_4^{(2)} \cos^4 \alpha + A_4^{(x)} \sin^2 \alpha \cos^2 \alpha. \quad (7.6)$$

Here, $A_2^{(1,2)}$ and $A_4^{(1,2)}$ are symmetry-plane moveout coefficients. $A_4^{(x)}$ is a cross-term that contributes in off-symmetry directions. Analogous to the VTI case, we expect equation 7.4 to be accurate for fitting PS traveltimes in horizontally-layered azimuthally anisotropic media.

Alkhalifah and Tsvankin (1995) proposed a simpler nonhyperbolic moveout equation for P-waves in VTI media that depends on only two parameters, the normal-moveout velocity V_{nmo} and anellipticity coefficient η :

$$T^2(x) = T_0^2 + \frac{x^2}{V_{\text{nmo}}^2} - \frac{2\eta x^4}{V_{\text{nmo}}^2 [T_0^2 V_{\text{nmo}}^2 + (1 + 2\eta) x^2]}. \quad (7.7)$$

Xu and Tsvankin (2006a) proved the 3D version of equation 7.7 to be accurate for computing geometrical spreading in orthorhombic or HTI media with a horizontal symmetry plane:

$$T^2(x, \alpha) = T_0^2 + \frac{x^2}{V_{\text{nmo}}^2(\alpha)} - \frac{2\eta(\alpha) x^4}{V_{\text{nmo}}^2(\alpha) [T_0^2 V_{\text{nmo}}^2(\alpha) + (1 + 2\eta(\alpha)) x^2]}, \quad (7.8)$$

$$V_{\text{nmo}}^{-2}(\alpha) = \frac{\sin^2 \alpha}{\left(V_{\text{nmo}}^{(1)}\right)^2} + \frac{\cos^2 \alpha}{\left(V_{\text{nmo}}^{(2)}\right)^2}, \quad (7.9)$$

and

$$\eta(\alpha) = \eta^{(1)} \sin^2 \alpha + \eta^{(2)} \cos^2 \alpha - \eta^{(3)} \sin^2 \alpha \cos^2 \alpha. \quad (7.10)$$

In equation 7.9, $V_{\text{nmo}}^{(1)}$ and $V_{\text{nmo}}^{(2)}$ are the semi-minor and semi-major axis of the NMO ellipse, respectively; $\eta^{(1,2,3)}$ are the anellipticity parameters in the three symmetry planes of orthorhombic media.

Although equations 7.7 and 7.8 was originally designed for P-waves, it is worthwhile to test them for PS-waves. If these equations yield satisfactory accuracy, the same formalism can be used to fit both P and PS traveltimes. Next, we apply equations 7.3 and 7.7 to PS-waves in a VTI model (model 1; parameters are listed in Table 1) to compute geometrical spreading using equation 7.2. Then, we test equations 7.4 and 7.8 for PS-waves in orthorhombic media (model 2; Table 2).

Figures 7.3 and 7.4 show the comparison of geometrical spreading computed by our moveout equations and by ray tracing. The Tsvankin-Thomsen equation yields results that are almost identical to those obtained by ray tracing. The Alkhalifah-Tsvankin equation, on the other hand, has the advantage of being consistent with that for P-waves while still providing adequate accuracy. It is worth mentioning that the best-fit parameter η for PS-waves differs from the anellipticity parameter for P-waves.

	Layer 1	Layer 2	Layer 3
Symmetry type	ISO	VTI	ISO
Thickness (km)	0.5	1.0	∞
Density (g/cm ³)	2.0	2.1	2.2
V_{P0} (km/s)	1.7	2.2	2.2
V_{S0} (km/s)	0.8	1.1	1.0
ϵ	0	0.23	0
δ	0	0.10	0
γ	0	0.10	0
η	0	0.10	0
σ	0	0.64	0

Table 7.1. Parameters of a three-layer VTI medium used in the numerical test (model 1). The parameters of the VTI layer are based on measurements of Dog Creek Shale (Thomsen, 1986). The event of interest is the PS conversion from the bottom of the VTI layer.

7.4 Application to AVO analysis of synthetic data

Because of the high sensitivity of S-waves to the presence of anisotropy, cusps, singularities, and areas of rapid amplitude changes are common for shear waves (Tsvankin, 2005). For that reason, MASC is likely to suffer from reduced accuracy for mode conversions. Moreover, the asymmetry of the raypath and wave modes can result in a significant angular variation of transmission loss. It is, therefore, necessary to test the performance of MASC on 3D full-wavefield synthetics for PS-waves even more so than for P-waves. As in Xu and Tsvankin (2006b), the questions addressed here are as follows:

1. Can MASC accurately reconstruct conversion coefficients in vertical symmetry planes of anisotropic media?
2. Are errors caused by empirical gain corrections acceptable for purposes of qualitative AVO analysis?
3. Can the influence of transmission loss be ignored as in P-wave AVO analysis?

To answer these questions, we carried out synthetic modeling and amplitude processing PSV waves in a VTI medium (model 1). The employed modeling tool is the reflectivity code (ANISYNPA) that generates an exact 3D wavefield for horizontally layered anisotropic media. Figure 7.5 displays a shot gather for vertical displacement generated by a vertical point source force in model 1. The processing sequence is similar to that for P-waves, and starts with moveout inversion. We then picked raw amplitudes along the travelttime curve defined by the moveout parameters. At the third step, MASC is applied to correct the picked amplitudes for anisotropic geometrical spreading. Finally, we removed the source and receiver directivity factors using the local horizontal slowness. To calibrate P-wave AVO, we matched the corrected amplitude with the exact reflection coefficient at normal incidence

	Layer 1	Layer 2	Layer 3
Symmetry type	VTI	ORTH	ISO
Thickness (km)	0.5	1.0	∞
Density (g/cm ³)	2.1	2.1	2.2
V_{P0} (km/s)	2.2	2.2	2.2
V_{S0} (km/s)	1.1	1.1	1.0
$\epsilon^{(1)}$	0.23	0.317	0
$\delta^{(1)}$	0.10	-0.054	0
$\gamma^{(1)}$	0.10	0.513	0
$\epsilon^{(2)}$	0.23	0.121	0
$\delta^{(2)}$	0.10	0.046	0
$\gamma^{(2)}$	0.10	0.138	0
$\delta^{(3)}$	0	0.1	0
$\eta^{(1)}$	0.1	0.42	0
$\eta^{(2)}$	0.1	0.07	0
$\sigma^{(1)}$	0.64	1.48	0
$\sigma^{(2)}$	0.64	0.31	0

Table 7.2. Parameters of a three-layer orthorhombic medium used in the numerical tests (model 2). Orthorhombic symmetry can be fully described by the two vertical velocities (V_{P0} for P-waves and V_{S0} for one of the split S-waves) and seven anisotropy parameters ($\epsilon^{(1)}$, $\epsilon^{(2)}$, $\delta^{(1)}$, $\delta^{(2)}$, $\delta^{(3)}$, $\gamma^{(1)}$, and $\gamma^{(2)}$). The anellipticity parameters $\eta^{(1)}$ and $\eta^{(2)}$ control P-wave nonhyperbolic moveout. The parameters $\sigma^{(1)}$ and $\sigma^{(2)}$ govern the moveout of SV-waves in the vertical symmetry planes. For a detailed explanation of the notation, see Tsvankin (2005). The parameters of the orthorhombic layer are based on the measurements of Wang (2002). The event of interest is the PS-wave converted at the bottom of the orthorhombic layer.

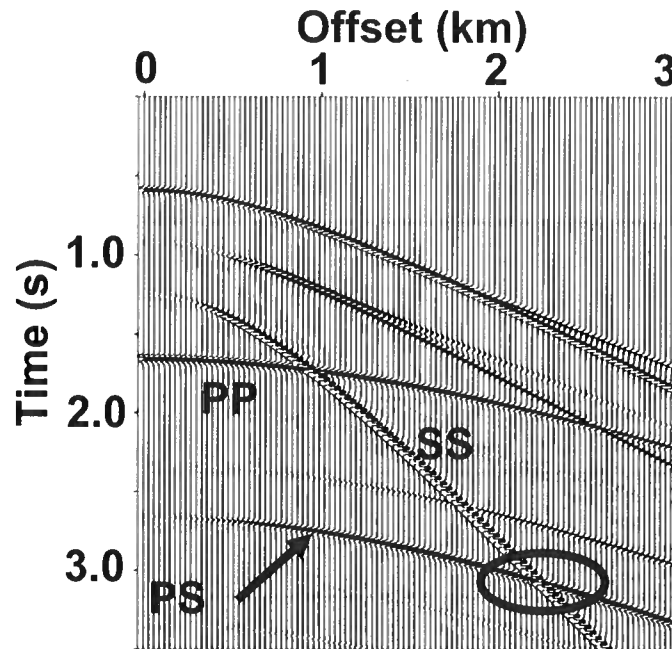


Figure 7.5. Synthetic shot gather for model 1 computed by the reflectivity method. The top layer is specified as a halfspace to eliminate the influence of the free surface. The arrow indicates the target PS-wave converted at the bottom of the VTI layer. The ellipse highlights the area of interference between the target PS event and the SS reflection from the top of the VTI layer.

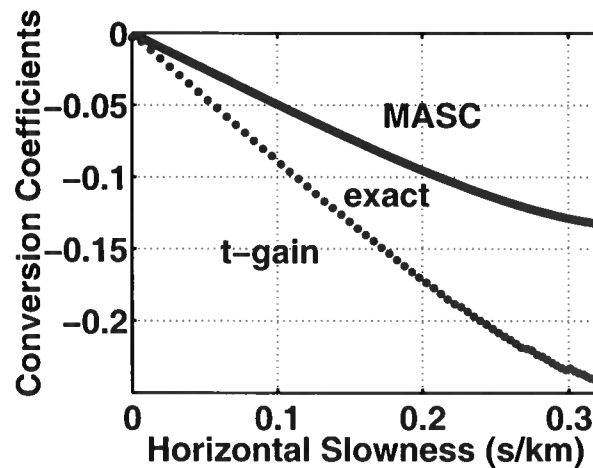


Figure 7.6. Comparison of the reconstructed conversion coefficients. The dashed line corresponds to the output of MASC; the dots mark the coefficient recovered by the t -gain correction; the solid line indicates the exact conversion coefficient. The take-off angle of the downgoing P-wave corresponding to the maximum horizontal slowness (0.3 s/km) is 30° ; for the upgoing S-wave, the angle is 15° .

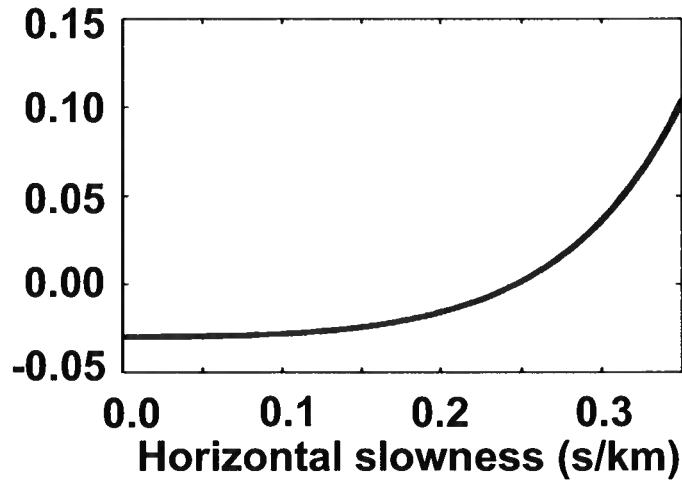


Figure 7.7. Transmission loss for the target PS-wave from Figure 5. The loss is computed by subtracting from unity the product of the plane-wave transmission coefficients along the raypath.

(Xu and Tsvankin, 2006b). For PSV-waves, however, this approach is not applicable since the conversion coefficient at normal incidence vanishes. We, therefore, apply the scaling factor estimated for P-waves to normalize the PSV conversion coefficients.

The VTI parameters of model 1 are based on the measurements of Dog Creek Shale (Thomsen, 1986). For this moderately anisotropic model, application of MASC (with the Tsvankin-Thomsen equation) yields conversion coefficients close to the exact values (Figure 7.6). The conventional gain correction t , on the other hand, results in considerable errors. The results of t^2 -gain correction, not shown here, are even less accurate. Clearly, the presence of anisotropy significantly distorts the geometrical spreading of PSV-waves in typical TI models. Application of MASC is essential for AVO analysis of converted PSV-waves.

Note that at far offsets the reconstructed conversion coefficient deviates substantially from the exact values. The deviation is partly caused by transmission loss and partly by the interference with the SS reflection from the top of the VTI layer (highlighted by the ellipse in Figure 7.5). For PP reflections, the two-way transmission coefficient is such that the resulting transmission loss is almost invariant with offset. Because of the asymmetry of the raypath and wave modes, however, the transmission loss for PSV-waves changes significantly with offset (Figure 7.7), which leads to non-negligible errors in the recovered conversion coefficients.

7.5 Conclusions

Despite the asymmetry of the raypath, the geometrical-spreading equation for PS-waves remains the same as that for pure P-waves (equation 7.2). Moreover, the MASC algorithm for P-waves can be adapted to converted waves in a straightforward manner. While the Tsvankin-Thomsen equation yields high accuracy in traveltimes fitting and, consequently, geometrical spreading, the simpler Alkhalifah-Tsvankin equation originally designed for P-waves also produces adequate accuracy for converted waves. Thus, we can apply the same formalism to both P and converted PS-waves to approximate traveltimes and compute geometrical spreading.

Since shear-wave amplitudes are more distorted by the presence of anisotropy, the errors caused by conventional gain corrections for PS-waves are more significant than those for PP reflections. Application of MASC, therefore, is beneficial for qualitative AVO analysis of PS-waves even in moderately anisotropic media. Compared to PP-waves, the error stemming from transmission loss is more significant for converted waves because of the asymmetry of the raypath and the conversion from P to S.

7.6 References

- Al-Dajani, A., Tsvankin, I., and Toksöz, M.N., 1998, Nonhyperbolic reflection moveout for azimuthally anisotropic media: 68th Ann. Internat. Mtg., Soc. Expl. Geophys., Expanded Abstracts, 1479–1482.
- Alkhalifah, T., and Tsvankin, I., 1995, Velocity analysis for transversely isotropic media: *Geophysics*, **60**, 1550–1566.
- Bakulin, A., V. Grechka, and I. Tsvankin, 2000, Estimation of fracture parameters from reflection seismic data – Part I: HTI model due to a single fracture set: *Geophysics*, **65**, 1788–1802.
- Červený, V., 2001, *Seismic ray theory*: Cambridge University Press.
- Dewangan, P., 2004, Processing and inversion of mode-converted waves using the PP+PS=SS method: Ph.D. thesis, Colorado School of Mines.
- Dewangan, P., I. Tsvankin, M. Batzle, K. van Wijk, and M. Haney, 2006, PS-wave moveout inversion for tilted TI media: A physical-modeling study: *Geophysics*, **71**, D135–D143.
- Jilek, P., 2002, Modeling and inversion of converted-wave reflection coefficients in anisotropic media: A tool for quantitative AVO analysis: Ph.D. thesis, Colorado School of Mines.
- Thomsen, L., 1986, Weak elastic anisotropy: *Geophysics*, **51**, 1954–1966.
- Thomsen, L., 1999, Converted-wave reflection seismology over inhomogeneous, anisotropic media: *Geophysics*, **64**, 678–690.

- Wang, Z., 2002, Seismic anisotropy in sedimentary rocks, part 2: Laboratory data: *Geophysics*, **67**, 1423–1440.
- Tsvankin, I., 1995, Body-wave radiation patterns and AVO in transversely isotropic media: *Geophysics*, **60**, 1409–1425.
- Tsvankin, I., 2005, *Seismic signatures and analysis of reflection data in anisotropic media*: Elsevier Science Publ. Co., Inc (second edition).
- Tsvankin, I., and Thomsen, L., 1994, Nonhyperbolic reflection moveout in anisotropic media: *Geophysics*, **59**, 1290–1304.
- Xu, X., I. Tsvankin, and A. Pech, 2005, Geometrical spreading of P-waves in horizontally layered, azimuthally anisotropic media: *Geophysics*, **70**, D43–D53.
- Xu, X., and I. Tsvankin, 2006a, Anisotropic geometrical-spreading correction for wide-azimuth P-wave reflections: *Geophysics*, **71**, D161–D170.
- Xu, X., and I. Tsvankin, 2006b, Azimuthal AVO analysis with anisotropic spreading correction: A synthetic study: *The Leading Edge*, (to appear in November issue).

Chapter 8

Conclusions

In this thesis I developed a practical methodology (MASC) for correcting wide-azimuth, long-offset multicomponent reflection amplitudes for azimuthally-varying geometrical spreading. The method operates with reflection traveltimes recorded on the earth's surface without using information about the subsurface velocity field. The algorithm conveniently fits into the processing sequence for estimating azimuthal moveout and AVO attributes. Also, little extra computational cost is necessary to carry out the proposed correction.

The methodology is based on the idea of expressing geometrical spreading through reflection traveltimes. By employing 3D nonhyperbolic moveout equations, I represented the geometrical spreading as a function of the moveout parameters. Using the weak-anisotropy approximation, I identified the key parameters responsible for the azimuthal variation of geometrical spreading, which is strongly dependent on the difference between the anellipticity parameters $\eta^{(1)}$ and $\eta^{(2)}$ in the two vertical symmetry planes of the model. Since long-spread traveltimes help to constrain the η parameters, it is beneficial to include long-spread data for computing geometrical spreading. The input to the spreading-correction algorithm includes the 3D nonhyperbolic moveout parameters, which can be obtained from moveout inversion of wide-azimuth, long-offset data. Since these parameters are needed for tracking reflection events for purposes of AVO analysis, the spreading correction does not incur extra cost except for implementing the equations in the Appendix C. The algorithm is insensitive to the trade-offs between various moveout parameters as long as the equation approximates the traveltime surface with good accuracy. In addition, sensitivity analysis shows that while the robustness of the MASC algorithm is lower than that of NMO-velocity inversion, it is higher than that of η estimation in the two vertical symmetry planes.

Application of MASC to full-wavefield synthetic data corroborates its accuracy in the presence of strong azimuthal anisotropy. The synthetic study demonstrated that the transmission loss is a secondary factor in reconstructing azimuthally-varying reflection coefficients for P-waves. Comparison of MASC with conventional gain correction shows that application of MASC can be critically important for quantitative AVO inversion. For qualitative AVO analysis, MASC becomes important when the relative strength of the azimuthal variation of the geometrical spreading is about one-third of that of the reflection coefficient.

To investigate the significance of anisotropic spreading correction for field data, I applied MASC to the azimuthal AVO analysis of a wide-azimuth dataset acquired at the Rulison field, Colorado. The results of AVO analysis for the bottom of the reservoir confirmed that application of MASC is essential for reliable estimation of azimuthal AVO attributes when the azimuthal variation of geometrical spreading is nonnegligible. Also illustrated by

the field study is the robustness of measurements of the azimuthal AVO gradient. Although amplitude signatures are often noisy, the high sensitivity of amplitude to the presence of anisotropy makes the azimuthal AVO gradient a relatively stable attribute. I observed good agreement between the azimuthal AVO attributes and both fault patterns and EMI logs in the field. Perhaps because of the influence of heterogeneity in the reservoir, I observed no clear correlation between the azimuthal AVO and NMO attributes.

Because of the high sensitivity of shear waves to the presence of anisotropy, it is imperative to correct for geometrical spreading in AVO analysis for PS-waves. Therefore, I extended the MASC algorithm to converted PS-waves. I showed that both Tsvankin-Thomsen- and Alkhalifah-Tsvankin-style equations can be used to approximate PS traveltimes. If the Alkhalifah-Tsvankin-style equation is chosen, the same formalism can be applied to correct geometrical spreading for both PP-waves and PS-waves. In contrast to the results for PP-waves, the influence of the transmission coefficient is nonnegligible for AVO analysis of converted waves.

An important assumption of this thesis is lateral homogeneity. Since geological and geophysical settings often violate this assumption to a certain degree, I performed numerical tests to study the applicability of MASC to models with mild dip and moderate lateral velocity variation. Preliminary numerical tests for media with strong azimuthal anisotropy suggest that errors of geometrical spreading computed by MASC are smaller than 10% when reflector dip does not exceed 20° . MASC remains accurate when the lateral velocity variation is linear and is not overly sensitive to moderate quadratic velocity variations.

Although the application of MASC here is focused on azimuthal AVO analysis for horizontally layered media, it can also be incorporated into Kirchhoff prestack time migration that accounts for azimuthal anisotropy. The 3D version of the Alkhalifah-Tsvankin equation can be used to compute traveltimes and slowness without ray tracing, and the MASC algorithm can be employed to compute the amplitude weighting factor. Future research is needed to further explore the applicability of MASC as an amplitude preserving tool for prestack time migration. For more complicated models with strong lateral velocity variation, correction for geometrical spreading has to be implemented in the context of true-amplitude prestack depth migration. For example, Vanelle (2002) employed the general geometrical-spreading equation (equation 4.10.50 of Červený, 2001) in prestack Kirchhoff depth migration. Brandsberg-Dahl et al. (2001) proposed to use the generalized Radon transform to extract reflection coefficients directly as functions of incidence angle and azimuth in angle gathers. In contrast to MASC, these techniques rely on accurate estimation of the velocity field.

Besides pronounced lateral heterogeneity, attenuation anisotropy is another subject not addressed in this work. Zhu (2006) has demonstrated that angular variation of attenuation, along with velocity anisotropy, has serious implications for AVO analysis. Investigation of the influence of attenuation anisotropy on reflection/transmission coefficients and other wave propagation phenomena is an ongoing research area. Among other difficulties that are not addressed here are anisotropic tuning phenomena and tilt of the symmetry planes (note that the equations of geometrical spreading in Appendices A and C handle tilt of symmetry planes; but the MASC algorithm does not).

Clearly, much research is required to account in a robust way for propagation factors and extract reflection coefficients in arbitrarily heterogeneous, anisotropic, attenuative media. Nevertheless, the development of MASC allows reliable qualitative azimuthal AVO analysis and enables quantitative azimuthal AVO inversion in areas of relatively simple subsurface structure. With the reasonable assumption that the layer containing sources and receivers is isotropic and has a known velocity, one can remove the source-receiver directivity factor from the recorded AVO signatures using local horizontal slownesses. Then, the MASC algorithm can correct for azimuthally-varying geometrical spreading without using velocity information. Since the influence of transmission loss on pure-mode amplitudes is negligible, the corrected amplitudes represent the variation of reflection coefficients with offset and azimuth. Well information can be used for calibrating the corrected amplitudes to the true reflection coefficients. Another obstacle in quantitative AVO inversion often mentioned in the literature is the transformation from offset to phase angle. For laterally homogeneous media, this problem can be avoided by expressing the reflection coefficients as a function of horizontal slowness. Once the issues discussed above are resolved, one can attempt quantitative azimuthal AVO inversion on field data. Using effective medium theory, the inverted parameters can be used to infer important rock properties. Particularly, with the advent of wide-azimuth acquisition offshore, I believe that the future for wide-azimuth AVO analysis is promising.

8.0 References

- Brandsberg-Dahl, S., 2001, Imaging-inversion and migration velocity analysis in the scattering-angle/azimuth domain: PhD thesis, Colorado School of Mines.
- Červený V., 2001, Seismic ray theory: Cambridge University Press.
- Vanelle, C., 2002, Traveltime-based true-amplitude migration: PhD thesis, University of Hamburg.
- Zhu, Y., 2006, Seismic wave propagation in attenuative anisotropic media: PhD thesis, Colorado School of Mines.

Appendix A

Relative geometrical spreading as a function of reflection traveltime

As discussed in the main text, the relative geometrical spreading $L(R, S)$ can be obtained in terms of the mixed second-order traveltime derivatives with respect to the source and receiver coordinates using equations (2.2) and (2.3). Here, we express $L(R, S)$ through the multiazimuth reflection traveltimes of a pure (non-converted) mode recorded over a laterally homogeneous medium.

The spreading factor $L(R, S)$ can be found from the traveltime-derivative matrix M^{mix} given in equation (2.3):

$$M^{\text{mix}} = \begin{bmatrix} \frac{\partial^2 T(x^r, x^s)}{\partial x_1^s \partial x_1^r} & \frac{\partial^2 T(x^r, x^s)}{\partial x_1^s \partial x_2^r} \\ \frac{\partial^2 T(x^r, x^s)}{\partial x_2^s \partial x_1^r} & \frac{\partial^2 T(x^r, x^s)}{\partial x_2^s \partial x_2^r} \end{bmatrix}, \quad (\text{A.1})$$

where x_1^s and x_2^s are the horizontal Cartesian coordinates of the source, and x_1^r and x_2^r are the coordinates of the receiver. In general, M^{mix} is a function of four independent variables, $x_1^{s,r}$ and $x_2^{s,r}$. For laterally homogeneous medium considered in this paper, however, the number of independent variables of M^{mix} reduces from four to two. Indeed, in the absence of lateral heterogeneity the traveltime T of a pure mode on a horizontal surface depends only on the distance x between the source and the receiver and the azimuth α of the source-receiver line with respect to the x_1 -axis:

$$x = \sqrt{(x_1^r - x_1^s)^2 + (x_2^r - x_2^s)^2}, \quad (\text{A.2})$$

$$\alpha = \tan^{-1} \left[\frac{x_2^r - x_2^s}{x_1^r - x_1^s} \right]. \quad (\text{A.3})$$

If the traveltime T is expressed as a function of x and α , the elements of the matrix M^{mix} become

$$\frac{\partial^2 T}{\partial x_1^s \partial x_1^r} = \frac{\partial^2 T}{\partial x^2} \frac{\partial x}{\partial x_1^s} \frac{\partial x}{\partial x_1^r} + \frac{\partial T}{\partial x} \frac{\partial^2 x}{\partial x_1^s \partial x_1^r} + \frac{\partial^2 T}{\partial \alpha^2} \frac{\partial \alpha}{\partial x_1^s} \frac{\partial \alpha}{\partial x_1^r} + \frac{\partial T}{\partial \alpha} \frac{\partial^2 \alpha}{\partial x_1^s \partial x_1^r}, \quad (\text{A.4})$$

$$\frac{\partial^2 T}{\partial x_1^s \partial x_2^r} = \frac{\partial^2 T}{\partial x^2} \frac{\partial x}{\partial x_1^s} \frac{\partial x}{\partial x_2^r} + \frac{\partial T}{\partial x} \frac{\partial^2 x}{\partial x_1^s \partial x_2^r} + \frac{\partial^2 T}{\partial \alpha^2} \frac{\partial \alpha}{\partial x_1^s} \frac{\partial \alpha}{\partial x_2^r} + \frac{\partial T}{\partial \alpha} \frac{\partial^2 \alpha}{\partial x_1^s \partial x_2^r}, \quad (\text{A.5})$$

$$\frac{\partial^2 T}{\partial x_2^s \partial x_1^r} = \frac{\partial^2 T}{\partial x_1^s \partial x_2^r}, \quad (\text{A.6})$$

$$\frac{\partial^2 T}{\partial x_2^s \partial x_2^r} = \frac{\partial^2 T}{\partial x^2} \frac{\partial x}{\partial x_2^s} \frac{\partial x}{\partial x_2^r} + \frac{\partial T}{\partial x} \frac{\partial^2 x}{\partial x_2^s \partial x_2^r} + \frac{\partial^2 T}{\partial \alpha^2} \frac{\partial \alpha}{\partial x_2^s} \frac{\partial \alpha}{\partial x_2^r} + \frac{\partial T}{\partial \alpha} \frac{\partial^2 \alpha}{\partial x_2^s \partial x_2^r}. \quad (\text{A.7})$$

The derivatives of x and α with respect to the source and receiver coordinates can be obtained from equations (A.2) and (A.3):

$$\frac{\partial x}{\partial x_i^s} = \frac{x_i^s - x_i^r}{x}, \quad \frac{\partial x}{\partial x_i^r} = \frac{x_i^r - x_i^s}{x} \quad (i = 1, 2), \quad (\text{A.8})$$

$$\frac{\partial \alpha}{\partial x_1^s} = \frac{x_2^r - x_2^s}{x^2}, \quad \frac{\partial \alpha}{\partial x_2^s} = \frac{x_1^s - x_1^r}{x^2}, \quad (\text{A.9})$$

$$\frac{\partial \alpha}{\partial x_1^r} = \frac{x_2^s - x_2^r}{x^2}, \quad \frac{\partial \alpha}{\partial x_2^r} = \frac{x_1^r - x_1^s}{x^2}, \quad (\text{A.10})$$

$$\frac{\partial^2 x}{\partial x_1^s \partial x_1^r} = \frac{-(x_2^r - x_2^s)^2}{x^3}, \quad (\text{A.11})$$

$$\frac{\partial^2 x}{\partial x_1^s \partial x_2^r} = \frac{(x_1^r - x_1^s)(x_2^r - x_2^s)}{x^3}, \quad (\text{A.12})$$

$$\frac{\partial^2 x}{\partial x_2^s \partial x_2^r} = \frac{-(x_1^r - x_1^s)^2}{x^3}, \quad (\text{A.13})$$

$$\frac{\partial^2 \alpha}{\partial x_1^s \partial x_1^r} = \frac{-2(x_1^r - x_1^s)(x_2^r - x_2^s)}{x^4}, \quad (\text{A.14})$$

$$\frac{\partial^2 \alpha}{\partial x_1^s \partial x_2^r} = \frac{(x_1^r - x_1^s)^2 - (x_2^r - x_2^s)^2}{x^4}, \quad (\text{A.15})$$

$$\frac{\partial^2 \alpha}{\partial x_2^s \partial x_2^r} = \frac{2(x_1^r - x_1^s)(x_2^r - x_2^s)}{x^4}. \quad (\text{A.16})$$

Substituting equations (A.8)–(A.16) into equations (A.4)–(A.7) yields

$$\frac{\partial^2 T}{\partial x_1^s \partial x_1^r} = -\frac{\partial^2 T}{\partial x^2} \frac{(x_1^r - x_1^s)^2}{x^2} - \frac{\partial T}{\partial x} \frac{(x_2^r - x_2^s)^2}{x^3} - \frac{\partial^2 T}{\partial \alpha^2} \frac{(x_2^r - x_2^s)^2}{x^4} - \frac{\partial T}{\partial \alpha} \frac{2(x_1^r - x_1^s)(x_2^r - x_2^s)}{x^4}, \quad (\text{A.17})$$

$$\frac{\partial^2 T}{\partial x_1^s \partial x_2^r} = \frac{\partial^2 T}{\partial x^2} \frac{-(x_1^r - x_1^s)(x_2^r - x_2^s)}{x^2} + \frac{\partial T}{\partial x} \frac{(x_1^r - x_1^s)(x_2^r - x_2^s)}{x^3} \quad (\text{A.18})$$

$$+ \frac{\partial^2 T}{\partial \alpha^2} \frac{(x_1^r - x_1^s)(x_2^r - x_2^s)^2}{x^4} + \frac{\partial T}{\partial \alpha} \frac{(x_1^r - x_1^s)^2 - (x_2^r - x_2^s)^2}{x^4}, \quad (\text{A.19})$$

$$\frac{\partial^2 T}{\partial x_2^s \partial x_2^r} = -\frac{\partial^2 T}{\partial x^2} \frac{(x_2^r - x_2^s)^2}{x^2} - \frac{\partial T}{\partial x} \frac{(x_1^r - x_1^s)^2}{x^3} - \frac{\partial^2 T}{\partial \alpha^2} \frac{(x_1^r - x_1^s)^2}{x^4} + \frac{\partial T}{\partial \alpha} \frac{2(x_1^r - x_1^s)(x_2^r - x_2^s)}{x^4}. \quad (\text{A.20})$$

The determinant of the matrix M^{mix} is then found as

$$\det M^{\text{mix}} = \frac{\partial^2 T}{\partial x^2} \frac{\partial T}{\partial x} \frac{1}{x} + \frac{\partial^2 T}{\partial x^2} \frac{\partial^2 T}{\partial \alpha^2} \frac{1}{x^2} - \left(\frac{\partial T}{\partial \alpha} \right)^2 \frac{1}{x^4}. \quad (\text{A.21})$$

Finally, using equation (A.21), the relative geometrical spreading (2.2) can be expressed through the traveltime derivatives with respect to the offset x and azimuth α :

$$L(R, S) = L(x, \alpha) = (\cos \phi^s \cos \phi^r)^{1/2} \left[\frac{\partial^2 T}{\partial x^2} \frac{\partial T}{\partial x} \frac{1}{x} + \frac{\partial^2 T}{\partial x^2} \frac{\partial^2 T}{\partial \alpha^2} \frac{1}{x^2} - \left(\frac{\partial T}{\partial \alpha} \right)^2 \frac{1}{x^4} \right]^{-1/2}. \quad (\text{A.22})$$

Appendix B

Traveltime derivatives from the nonhyperbolic moveout equation

P-wave nonhyperbolic (long-spread) reflection traveltime can be described by the Tsvankin-Thomsen (1994) moveout equation:

$$T^2(x, \alpha) = T_0^2 + A_2(\alpha) x^2 + \frac{A_4(\alpha) x^4}{1 + A(\alpha) x^2}, \quad (\text{B.1})$$

where the moveout coefficients A_2 , A_4 , and A generally vary with the azimuth α .

The derivatives of the traveltime with respect to the offset x are given by

$$\frac{\partial T}{\partial x} = \frac{1}{T} \left[A_2 x + \frac{2A_4 x^3}{1 + A x^2} - \frac{A A_4 x^5}{(1 + A x^2)^2} \right] \quad (\text{B.2})$$

and

$$\frac{\partial^2 T}{\partial x^2} = \frac{1}{T} \left[f(x) - \left(\frac{\partial T}{\partial x} \right)^2 \right]; \quad (\text{B.3})$$

$$f(x) \equiv A_2 + \frac{6A_4 x^2}{1 + A x^2} - \frac{9A A_4 x^4}{(1 + A x^2)^2} + \frac{4A_4 A^2 x^6}{(1 + A x^2)^3}. \quad (\text{B.4})$$

Differentiating equation (B1) with respect to azimuth yields

$$\frac{\partial T}{\partial \alpha} = \frac{1}{2T} \left[A_2' x^2 + \frac{A_4' x^4}{1 + A x^2} - \frac{A_4 A' x^6}{(1 + A x^2)^2} \right] \quad (\text{B.5})$$

and

$$\begin{aligned} \frac{\partial^2 T}{\partial \alpha^2} = & \frac{\partial T}{\partial \alpha} \frac{1}{2T^2} \left[A_2' x^2 + \frac{A_4' x^4}{1 + A x^2} - \frac{A_4 A' x^6}{(1 + A x^2)^2} \right] + \frac{1}{2T} \\ & \left[A_2'' x^2 + \frac{A_4'' x^4}{1 + A x^2} - \frac{A_4 A'' x^6}{(1 + A x^2)^2} - \frac{2A' A_4' x^6}{(1 + A x^2)^2} + \frac{2A_4 (A')^2 x^8}{(1 + A x^2)^3} \right] \end{aligned} \quad (\text{B.6})$$

Here, A_2' , A_4' , A' , A_2'' , A_4'' and A'' are the first and second derivatives of the moveout coefficients with respect to α . For the model of a single orthorhombic layer, these derivatives can be found from the explicit expressions for A_2 , A_4 , and A given in the main text.

Appendix C

Traveltime derivatives for the geometrical-spreading correction

In Appendix B the traveltime derivatives needed in the geometrical-spreading equation 3.1 are expressed through the parameters A_2 , A_4 , and A of the Tsvankin-Thomsen (1994) moveout equation. Here, we showed that an accurate description of traveltimes in layered orthorhombic media can be achieved by using a simpler moveout approximation (equation 3.4) based on the analogy with vertical transverse isotropy. Equation 3.4 can be considered as a special case of the Tsvankin-Thomsen moveout equation with the parameters given by

$$A_2(\alpha) = \frac{\sin^2(\alpha - \phi)}{\left(V_{\text{nmo}}^{(1)}\right)^2} + \frac{\cos^2(\alpha - \phi)}{\left(V_{\text{nmo}}^{(2)}\right)^2}, \quad (\text{C.1})$$

$$A_4(\alpha) = -\frac{2\eta(\alpha)}{T_0^2 V_{\text{nmo}}^4(\alpha)}, \quad (\text{C.2})$$

$$A(\alpha) = \frac{1 + 2\eta(\alpha)}{T_0^2 V_{\text{nmo}}^2(\alpha)}, \quad (\text{C.3})$$

where

$$\eta(\alpha) = \eta^{(1)} \sin^2(\alpha - \phi_1) + \eta^{(2)} \cos^2(\alpha - \phi_1) - \eta^{(3)} \sin^2(\alpha - \phi_1) \cos^2(\alpha - \phi_1). \quad (\text{C.4})$$

As discussed in the main text, the azimuth ϕ_1 is equal to ϕ with uniform symmetry-plane orientation.

Substituting equations (C-1)–(C-3) into equations (B-2)–(B-4), we obtain the derivatives $\partial T/\partial x$ and $\partial^2 T/\partial x^2$ in terms of the parameters T_0 , ϕ , ϕ_1 , $V_{\text{nmo}}^{(1)}$, $V_{\text{nmo}}^{(2)}$, $\eta^{(1)}$, $\eta^{(2)}$, and $\eta^{(3)}$. The geometrical spreading also depends on the first two traveltime derivatives with respect to the azimuth α , which are expressed in equations (B-5) and (B-6) through the corresponding derivatives of A_2 , A_4 , and A . Using equations (C-1)–(C-3) to differentiate A_2 , A_4 , and A with respect to α , we find (prime and double-prime denote the first- and second-order derivatives, respectively)

$$A'_2 = \left[\frac{1}{\left(V_{\text{nmo}}^{(1)}\right)^2} - \frac{1}{\left(V_{\text{nmo}}^{(2)}\right)^2} \right] \sin 2(\alpha - \phi), \quad (\text{C.5})$$

$$A''_2 = 2 \left[\frac{1}{\left(V_{\text{nmo}}^{(1)}\right)^2} - \frac{1}{\left(V_{\text{nmo}}^{(2)}\right)^2} \right] \cos 2(\alpha - \phi), \quad (\text{C.6})$$

$$A'_4 = \frac{1}{T_0^2 \left(V_{\text{nmo}}^{(1)}\right)^4 \left(V_{\text{nmo}}^{(2)}\right)^4} \left\{ 2 \left[\left(V_{\text{nmo}}^{(1)}\right)^2 \cos^2(\alpha - \phi) + \left(V_{\text{nmo}}^{(2)}\right)^2 \sin^2(\alpha - \phi) \right] \right. \\ \times \left\{ -\frac{1}{2} \left[\left(V_{\text{nmo}}^{(1)}\right)^2 + \left(V_{\text{nmo}}^{(2)}\right)^2 + \left(\left(V_{\text{nmo}}^{(1)}\right)^2 - \left(V_{\text{nmo}}^{(2)}\right)^2 \right) \cos 2(\alpha - \phi) \right] \right. \\ \times \left[-\eta^{(1)} + \eta^{(2)} + \eta^{(3)} \cos 2(\alpha - \phi_1) \right] \sin 2(\alpha - \phi_1) \\ + \left(\left(V_{\text{nmo}}^{(1)}\right)^2 - \left(V_{\text{nmo}}^{(2)}\right)^2 \right) \cos(\alpha - \phi) \sin(\alpha - \phi) \\ \times \left[-4\eta^{(2)} \cos^2(\alpha - \phi_1) - 4\eta^{(1)} \sin^2(\alpha - \phi_1) \right. \\ \left. \left. + \eta^{(3)} \sin^2 2(\alpha - \phi_1) \right] \right\} \left. \right\}, \quad (\text{C.7})$$

$$+ \eta^{(3)} \sin^2 2(\alpha - \phi_1) \left. \right\}, \quad (\text{C.8})$$

$$A''_4 = \frac{1}{2T_0^2 \left(V_{\text{nmo}}^{(1)}\right)^4 \left(V_{\text{nmo}}^{(2)}\right)^4} \left\{ \left(\left(V_{\text{nmo}}^{(1)}\right)^2 - \left(V_{\text{nmo}}^{(2)}\right)^2 \right) \right. \\ \times \left[\left(\left(V_{\text{nmo}}^{(1)}\right)^2 + \left(V_{\text{nmo}}^{(2)}\right)^2 \right) \cos 2(\alpha - \phi) + \left(\left(V_{\text{nmo}}^{(1)}\right)^2 - \left(V_{\text{nmo}}^{(2)}\right)^2 \right) \cos 4(\alpha - \phi) \right] \\ \times \left[-4(\eta^{(1)} + \eta^{(2)}) + \eta^{(3)} + 4(\eta^{(1)} - \eta^{(2)}) \cos 2(\alpha - \phi_1) - \eta^{(3)} \cos 4(\alpha - \phi_1) \right] \\ - 2 \left[\left(V_{\text{nmo}}^{(1)}\right)^2 + \left(V_{\text{nmo}}^{(2)}\right)^2 + \left(\left(V_{\text{nmo}}^{(1)}\right)^2 - \left(V_{\text{nmo}}^{(2)}\right)^2 \right) \cos 2(\alpha - \phi) \right]^2 \\ \times \left[(\eta^{(2)} - \eta^{(1)}) \cos 2(\alpha - \phi_1) + \eta^{(3)} \cos 4(\alpha - \phi_1) \right] \\ + 8 \left(\left(V_{\text{nmo}}^{(1)}\right)^2 - \left(V_{\text{nmo}}^{(2)}\right)^2 \right) \left[\left(V_{\text{nmo}}^{(1)}\right)^2 + \left(V_{\text{nmo}}^{(2)}\right)^2 + \left(\left(V_{\text{nmo}}^{(1)}\right)^2 - \left(V_{\text{nmo}}^{(2)}\right)^2 \right) \cos 2(\alpha - \phi) \right] \\ \times \left[-\eta^{(1)} + \eta^{(2)} + \eta^{(3)} \cos 2(\alpha - \phi_1) \right] \sin 2(\alpha - \phi) \sin 2(\alpha - \phi_1) \left. \right\}, \quad (\text{C.9})$$

$$\begin{aligned}
 A' = & -\frac{1}{T_0^2 \left(V_{\text{nm}o}^{(1)}\right)^2 \left(V_{\text{nm}o}^{(2)}\right)^2} \left\{ \left[\left(V_{\text{nm}o}^{(1)}\right)^2 + \left(V_{\text{nm}o}^{(2)}\right)^2 + \left(\left(V_{\text{nm}o}^{(1)}\right)^2 - \left(V_{\text{nm}o}^{(2)}\right)^2 \right) \cos 2(\alpha - \phi) \right] \right. \\
 & \times \left[-\eta^{(1)} + \eta^{(2)} + \eta^{(3)} \cos 2(\alpha - \phi_1) \right] \sin 2(\alpha - \phi_1) \\
 & + \left(\left(V_{\text{nm}o}^{(1)}\right)^2 - \left(V_{\text{nm}o}^{(2)}\right)^2 \right) \cos(\alpha - \phi) \sin(\alpha - \phi) \\
 & \left. \times \left[2 + 4\eta^{(2)} \cos^2(\alpha - \phi_1) + 4\eta^{(1)} \sin^2(\alpha - \phi_1) - \eta^{(3)} \sin^2 2(\alpha - \phi_1) \right] \right\}, \quad (\text{C.10})
 \end{aligned}$$

$$\begin{aligned}
 A'' = & \frac{1}{T_0^2 \left(V_{\text{nm}o}^{(1)}\right)^2 \left(V_{\text{nm}o}^{(2)}\right)^2} \left\{ \frac{1}{2} \left(\left(V_{\text{nm}o}^{(1)}\right)^2 - \left(V_{\text{nm}o}^{(2)}\right)^2 \right) \cos 2(\alpha - \phi) \right. \\
 & \times \left[-4(1 + \eta^{(1)} + \eta^{(2)}) + \eta^{(3)} + 8(\eta^{(1)} - \eta^{(2)}) \cos 2(\alpha - \phi_1) - 5\eta^{(3)} \cos 4(\alpha - \phi_1) \right] \\
 & + 2 \left(\left(V_{\text{nm}o}^{(1)}\right)^2 + \left(V_{\text{nm}o}^{(2)}\right)^2 \right) \left[(\eta^{(1)} - \eta^{(2)}) \cos 2(\alpha - \phi_1) - \eta^{(3)} \cos 4(\alpha - \phi_1) \right] \\
 & + 4 \left(\left(V_{\text{nm}o}^{(1)}\right)^2 - \left(V_{\text{nm}o}^{(2)}\right)^2 \right) \left[-\eta^{(1)} + \eta^{(2)} + \eta^{(3)} \cos 2(\alpha - \phi_1) \right] \\
 & \left. \sin 2\alpha \sin 2(\alpha - \phi_1) \right\}. \quad (\text{C.11})
 \end{aligned}$$

Substitution of equations (C-5)–(C-10) into equations (B-5) and (B-6) yields the derivatives $\partial T/\partial\alpha$ and $\partial^2 T/\partial\alpha^2$ as explicit functions of the moveout parameters.

